University of Naples

"Federico II"

School of Polytechnic and Basic sciences
Department of Chemical Sciences

Doctoral Thesis

Cycle XXIX

Raman-assisted Crystallography applied to protein metalation

Candidate
Marco Caterino

Tutors
Prof. A. Vergara
Prof. A. Merlino

Supervisor
Prof. F. Ruffo

Index

1

Introduction

1.1 Introducing metals

Beyond myths and beliefs, metals have drawn noticeable attention throughout centuries because of (mostly supposed rather than actually proven) medicinal virtues. Copper, arsenic, mercury and the entire precious metals series have been deployed either for rational and for the most odd and awkward purposes, from water sanitisation, wound healing, not missing boosting fertility, dental care and almost every bizarre remedy one could possibly figure out. Yet, there has been an ounce of truth likewise each worthy tale.

The exploiting modern medicine progressively led to prove many metal-based drugs to be highly effective against sundry disorders, diseases and syndromes. Since then, a sweeping set of metal complexes has been synthesized for pharmacological purposes in many fields. Anticancer is intelligibly the foremost nowadays, but endeavours have been spent also for sampling metallo-drugs as anti-inflammatory, antibacterial, anti-rheumatic, and antimalarial and more.[1-4]

The distinctive electronic configuration is the very reason making transition metals such a unique item in the anti-cancer weaponry as it confers distinctive characteristics and offers great versatility, in terms of the ability to tune the properties of a given molecule. It translates in the chance to fine develop key pharmacological aspects such as selective drug activation and delivery.

1.2 Platinum

Metal-based drugs have come to the scene as effective anti-cancer drugs in the between of late 50s and late 60s thanks to Francis Dwyer, who first learned about the ruthenium polypyridyl anticancer qualities,[5-7] and Barnet Rosenberg, who kick started the vigorous research towards anti-cancer active platinum-based compounds back in 1969, after his findings on the very first Pt-based anti-tumour medicine: the *cisplatin*, cis-di-ammino-di-chlorido-platinum(II).[8] Cisplatin has eventually become the very first FDA-approved metal-based anticancer drug back in 1979, yet used to the treatment of testicular, ovarian, bladder, lung, and head-neck cancers.[9,10]

The cisplatin effectiveness, tough not yet wholly understood, ascribes to its ability to bind nuclear DNA.[11] Anyhow, its cellular uptake is known to depend on the interaction with the CTR1 copper-transport protein.[12-14] Remarkably, it is nowadays clear DNA is not the exclusive target for most metallo-drugs: rather than simple sparring partners, proteins play as starring characters for the pharmacological mechanics as they likely act as carriers for drug delivery, release, activation modulators and, ultimately, drug targets.[11,15-18]

Major drawbacks for cisplatin had emerged suddenly as it prompts severe side effects mainly because the drug blindly strikes both sick and healthy cells. Furthermore, many tumours exhibit either acute or acquired resistance towards this medicine as well as barely 1% of administered drug actually reaches its DNA target.[11,15,19] This had shoved towards developing new Pt compounds but only a few (*carboplatin* and *oxaliplatin* are the most representative - Figure 1) have actually proven effective and eventually been approved.[20,21] Square-planar coordination geometry of Pt(II) is thought to be the

utmost limiting factor for Pt effectiveness.[22] A brief gallery of representative platinum anticancer agents is reported in Figure 1. The success and limitations of Pt drugs have been driving forces towards probing new and diverse metals in cancer treatment. Ruthenium, palladium and gold-based compounds came next and the medicinal inorganic chemistry research branch has been progressively thriving since then, as the anti-tumour qualities of many other metals have been studied, including, iridium, osmium, cobalt, vanadium, copper and others.[1,3,11,23-25]

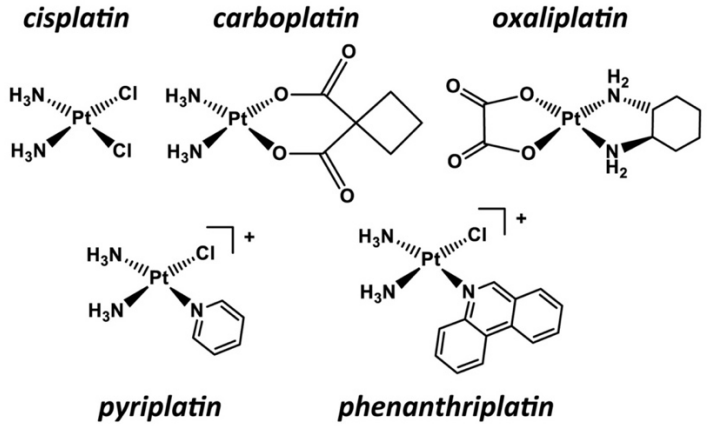

Figure 1 – Chemical structures for the most representative Pt-based anticancer active drugs.

1.3 Palladium and Gold

Beyond platinum and among other metals tested in anticancer treatment, palladium and (even more) gold should deserve a much deeper discussion than this text is meant for.

A palladium complex has been the first Pt alternative undergoing clinical trials against different solid tumours. Pd exhibits coordination and geometry likewise Pt but with a higher tendency to hydrolysis. Its complexes have been recorded cytotoxic towards a variety of cancers though no actual breakthroughs have been clinched in the search of cisplatin successor. For a more comprehensive insight please refer to.[15,26-28]

The first and longstanding application of gold in modern medicine, the rheumatoid arthritis treatment, dates back to the 1930s and stayed as almost the sole gold medicinal usage until late XX century. Au(I) thiolates are the class forefathers whereas *auranofin* is probably the most famous modern successor, on duty since 1985.[29] Notwithstanding Au(I) complexes do have striking cytotoxicity against haemolymphatic cancers *in-vitro*, most of them arose severe cardiac threats and hence rejected for clinical trials.[15]

Au(III) compounds are drawing lively research energies as they have been proved to be a good source of potential alternatives to cisplatin, mostly because resembling the Pt(II) d^8 electronic configuration. In spite of structural similarities, Au(III)-based drugs act somehow differently from cisplatin, additionally showing a larger variety of DNA- or protein-binding chances, but inconsistent results achieved from different complexes contribute to puzzle the big picture of Au(III)-complexes action mechanisms.[15] Au(III) complexes also share a variety of cons with cisplatin when it comes to high toxicity, induced drug resistance, deficiency in cancer-cell specificity and limited bioavailability.

Anyhow a number of gold complexes, notably those based on thiocarbamates, have demonstrated to be worthy candidates for taking over from cisplatin as effective and non-toxic anticancer agents. Readers should refer to following references for further details.[3,11,15,25,30,31]

1.4 Iridium

No sooner had the Pt compounds been exploited than the d^7 element iridium, and its groupmate rhodium, had attracted the scientists interests as potential Pt alternative in cancer treatment, but it took longer to accelerate enough the Ir very slow aquation kinetic by ligand substitution to make its complexes actually bioactive.[15,25,32]

Iridium complexes had shown effective in a range of biomedical applications such as protein and peptide labelling and sensing, cellular and tissue imaging and anticancer.[32-40]

At the beginning, most efforts had been poured for Ir(I) complexes exhibiting square-planar geometry, as seen for cisplatin, but Ir(III) compounds have demonstrated effective and taken the scene, mostly as organo-iridium complexes.[32]

Amid other metals, such as Mn, Fe, Co and Ru,[41-43] iridium has shown effective as carbon monoxide-releasing molecules (**CORM**s) as well.[43,44]

Carbon monoxide (**CMO**) has been recognized as a viable therapeutic molecule for an assortment of conditions and mechanisms (Figure 2) including cancer but, on the flip side, the very low binding selectivity the CMO has towards plenty of biomolecules can easily turn it into a poison rather than a remedy.[45]

Here-hence the need for CORMs as it had been demonstrated that carbon monoxide release could realise selectively and modulated under certain conditions once bound to a metal.[45,46]

The CMO release has been reported to occur in different ways according to the core metal and its ligands, including unmodulated thermal activation,[47] simple hydrolysis in physiological buffers,[47] enzymatic catalysis,[48,49] or by photo-activation.[50,51]

Anyhow, a rational development of CORMs passes through a comprehensive understanding of their pharmacological mechanisms. Therefore, the comprehension of the interaction of CORMs with biological macromolecules, mainly plasma proteins, cannot be left apart, but a few studies have taken this aspect into account by now.[52-56]

This work will address for new insights on the interaction between a novel Ir-based CORM ($IrCl_5CO$)[43] and the bovine pancreatic ribonuclease A, a model protein system (see Chapter 6 – page 87).[57]

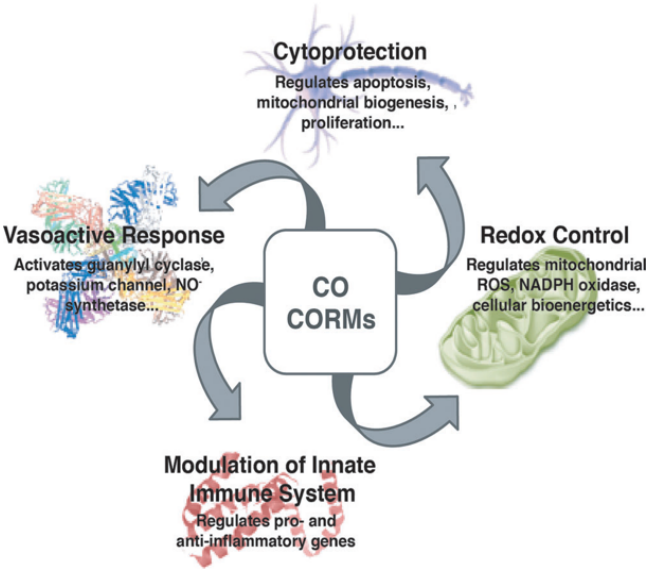

Figure 2 - Biological effects of carbon monoxide delivered as a gas or as a CO-releasing molecule (CORM).[52]

1.5 Ruthenium

Ruthenium deserves a special mention in the metal-based drug file as its complexes are doubtless the most promising, interesting and studied all over the current inorganic chemotherapeutic scenario.[15] Ruthenium drugs as anti-tumour agents had been first tested by Clarke *et al.* but it took a while for Ru-drugs to find actual deployment since the first synthesised complexes suffered mainly from very low solubility.[58-61]

Most of the early efforts have been put-in to solve this very issue and, albeit none of the complexes proposed has achieved to reach actual clinical usage as yet, two acclaimed complexes, namely †NAMI-A (New Anti-tumour Metastasis Inhibitor), *and* ‡KP1019, have both reached phase II in clinical trials showing remarkable performances.[11,16,58,59,62]

A little more in detail, NAMI-A yet exhibits some curbs because of its sudden ligand swapping within minutes in aqueous environment at physiological pH and temperature.[63,64] This makes NAMI-A nearly inactive towards primary cancers, whilst expressing appreciable anti-metastatic action.[58,60,64,65] Consequently, it became clear that its activity could not relate directly to the nuclear DNA binding.[66,67] Clues about the NAMI-A interaction with actin-type surface proteins[68,69] and extracellular collagens matrix,[70,71] both involved in well-known mobility frameworks of metastatic cells, suggest possible protein-mediated mechanisms to explain the anti-metastatic virtues of NAMI-A.[64,68-73]

The KP1019 complex has been introduced at roughly the same time as NAMI-A but, on the contrary, it is much more stable in

---

†imidazolium trans-[tetrachloro-(S-dimethyl-sulfoxide)(1H-imidazole)ruthenate(III)]

‡indazolium [trans-tetrachlorobis(1H-indazole)ruthenate(III)]

physiological conditions and shows more favourable cellular uptake kinetics than NAMI-A.[23,24,74-76]

KP1019, and even more its derivative KP1339, are curiously and providentially completing what left uncovered by NAMI-A. It indeed possesses slight anti-metastatic activity but striking strength against primary cancers as well as towards some cisplatin-resistant tumours.[4,58,74,77]

A number of studies have definitively casted off the paradigm of the exclusive interaction with DNA, bringing hints for diverse mechanisms of action mostly entailing Ru-protein dealings.[72,73,78,79] This prompted to broaden the knowledge about the underlying structural basis in the endeavour to mature the big picture of selective Ru-drug delivery and targeting.[16-18,80]

Ruthenium-based drugs owe much of their success in the current anticancer panorama to the ease they access different oxidation states under physiological conditions.[16,81] Ru(III) is the dominant and most stable form though marginally anticancer active and largely bound to blood-plasma proteins once administered, essentially acting as a prodrug form.[4,58,64] In fact, its anti-tumour potential has been proven to rely on the reduction to Ru(II),[61,82,83] which is widely recognised to be the utmost anticancer-active ruthenium form.[4,58,64] Ru(II), alike Ru(IV), can be promptly accessed in the presence of ordinary biological reducing or oxidising agents, particularly abundant within cancer cells environs.[4,25,64,82-85] Hypotheses have been advanced for Ru(V) species within cells as well, but this stays controversial.[58,86]

These alluring traits of the ruthenium redox chemistry resemble the "*activation by reduction*" theory that, first postulated for Pt(IV) complexes, has proven somewhat successful among the whole set of different strategies for selectively releasing and/or activating

higher oxidation state complexes that, accordingly, are to be referred to as prodrugs.[64,82,87]

The bedrock for the edge that ruthenium has over Pt or Au is the octahedral geometry that its complexes exhibit (Ru(II) commonly have also *piano-stool* pseudo-octahedral geometry).[58,88,89] The octahedral coordination geometry grants superior flexibility, meant in terms of chances for tuning their selective targeting and activation compared to Pt-complexes,[30,59,73,81] *i.e.* by tweaking the valuable axial ligands for fine-tuning the steric, electronic and hence thermodynamic and kinetic properties of the complexes.[15,64,73] Ultimately, the aggregate of these features leads to a general lower toxicity compared to Pt compounds, though retaining an excellent *in-vivo* anticancer activity.[16,90,91]

In spite of sparkling research activity, challenging issues remain. Developing selective targeting and activation is the foremost priority for addressing side effects and improving medicine effectiveness. Besides and surprisingly, the structures, speciation in biological environs, exact molecular targets and acting mechanisms have not yet been elucidated for a significant number of approved and in-development drugs either.[16] A deeper insight into these pharmacokinetics and pharmacodynamics aspects may also lead to fresh and efficient drug-designs for treating a wider host of diseases yet not tackled.

This text addresses for the investigation of some key physical chemical properties of AziRu, a novel Ru-based prodrug derived from NAMI-A (see Chapter 7 – page 107).

1.6 Metal nanoparticles

Nanoparticle research is nowadays a cutting-edge area of intense scientific efforts due to the huge pool of actual and potential applications in biomedical, optics, electronics, engineering and a variety of diverse fields. This comes from the large number of special properties compared to bulk material that the nanoparticles (**NP**s) exhibit. By far the most investigated nanoparticle systems are gold nanoparticles (**AuNP**s).[92] Their properties tightly relate to size, shape, aggregation and local environ state (as a rule a thumb for each nanoscale system).

Optical properties are the utmost apparent feature which depend mostly on size, shape and dielectric constant of the surrounding environ. AuNPs exhibit a distinctive size-dependent wine-red colour when sphere-shaped because of the Surface Plasmon Resonance (**SPR**) effect.[92-94] SPR generates from the interaction between electromagnetic radiation of an appropriate wavelength and the metallic surface, resulting in an electric field on the nanoparticles surface that triggers the enhancement of the incident field by several magnitudes.[93-96]

This huge magnification of the electric field adjoining the NPs (as well as rough metal surfaces) is the source of the sturdy enhancement in the Raman scattering cross-section known as Surface Enhanced Raman Scattering (**SERS**), first observed by Fleischman, back in 1974.[92,97]

Because of these exceptional features, AuNPs found a rich variety of applications in industry, and progressively in consumer markets, in a large assortment of areas *i.e.* nano-catalysis, sensing, storage and computing devices, nano-devices, nano-labelling, bioimaging and therapeutic purposes.[93,98-101]

Medicinal and biotechnological applications greatly benefited from the large AuNPs biocompatibility, which made of theme appealing, among other purposes, for anticancer intents.[102-104] Furthermore, AuNPs have large and tuneable absorption in the near infrared (**NIR)** spectral region, where most of tissue components are nearly transparent, making of theme the perfect candidates for *in-tissue* sensing and photo-therapy.[102-105] Indeed, the NIR-related photo-thermal effect have also been profitably exploited to selectively kill tumour cells *in-vivo*.[92,93,106,107]

The very high AuNPs SERS allows to sniff out minute concentration and led to further advances in molecular detection: trace analysis of various organic compounds, biomolecules and even bacteria and viruses, antigens, carbohydrates, polluting agents, proteins and nucleic acids up to 10^{-9} M, and more.[92,95,96,108-115]

AuNPs also exhibit very appealing catalytic properties *e.g.* can convert the highly toxic carbon monoxide (**CMO**) to the less troublesome carbon dioxide,[116,117] catalyse hydrogenation processes,[98] pesticides degradation[118] or enhance visible light optical absorption within solar cells.[98]

Interestingly, catalytic properties have been demonstrated to be size- and shape-dependent likewise optical features.[98,119,120]

Efforts have been spent for developing high-yield hybrid catalytic systems made up by coupling AuNPs and enzymes either in solution or in crystalline state.[121-124]

Herein I will discuss about new structural findings concerning these newly proposed catalytic hybrid systems (see Chapter 4 – page 61).

1.7 Aims and Targets

This brief introduction to the metallic world guided the reader through interesting spotlights that make the study of the interaction between either *metal-ions and metal-nanoparticles* with protein systems very appealing from a variety of perspectives. The anticancer purpose remains as the forefront due to its uncountable social impact. A deeper comprehension of key aspects driving the functioning of these systems may spring new interesting outlooks for the development of some alluring potential anticancer drugs.

Besides metal-based drugs, the methodological approach herein adopted efficiently works also for studying metal-containing protein systems and it has been successfully deployed to enquire into the interaction between the Zn-containing protein human carbonic anhydrase II (**hCAII**) and some of its inhibitors (see Chapter 5 – page 73).

This work is to be meant as consolidating the relatively novel and progressively spreading *methodological approach* named *Raman-assisted Crystallography* (**RAC** from now on), which combines strengths from Raman microspectroscopy and X-ray crystallography techniques for overriding their respective weaknesses, by securing structural and physical-chemical information for either metal-based drugs and metal-containing proteins. RAC has been deployed as pivotal tool besides a set of common spectroscopic techniques.

X-ray crystallography stays as the golden standard for structural investigation providing nearly atomic resolution data though yet having some limitations. Raman microspectroscopy thus turns useful as a source of valuable data for integrating crystallographic records.

The synergy of these two techniques has been progressively thriving during the last decade and a brief introduction to the RAC concept and its applications, in addition to some theoretical pills about the two techniques it relies on, are discussed in the section to come. Detailed methodological and technical information are provided within each experimental section in the chapters to follow, whilst here is a brief summary of the investigated:

- In chapter 2 early RAC experimental setup is proved by detecting Hg^{2+} insertion and its induced structural modifications within a single protein crystal.
- In chapter 3 a combination of ultrahigh resolution X-ray data and online Raman spectroscopy for the characterisation of the X-ray induced photodamage on single protein crystal.
- Chapter 4 confutes previous crystallographic evidences for the AuNPs co-crystallization within lysozyme crystals.
- Chapter 5 addresses illustrates the disambiguation of the binding mode of a new carbonic anhydrase inhibitor via RAC.
- Chapter 6 addresses for the Ir-based CORM binding to proteins and thereon CO release.
- Chapters 7 and 8 discuss about the structural and physical-chemical characterisation of the selective reduction/release mechanism from proteins of a ruthenium-based prodrug, by means of RAC and electro-SERS. Part of these activities have been brought out during my stay at the TUB in Berlin.

1.8 Raman-assisted Crystallography

This section provides a brief introduction to the concepts beyond the experimental approach adopted in this thesis, yielding a brief and basic theoretical introduction to the techniques it relies on, redirecting to each experimental section for further detailed information.

The Raman scattering phenomenon has been named after the Indian physicist who first had discovered the inelastic scattering of light phenomenon, back in 1928.

It relies on the inelastic scattering of a small fraction of monochromatic light at frequencies determined by the structure of the molecule and the resulting scattered light can have either higher (Stokes scattering) or lower (anti-Stokes scattering) energy than the incident beam.

Raman spectroscopy provides detailed vibrational information concerning the structure of molecules as the position and intensity of spectral features return the molecular structure and can be used to determine the chemical identity of the sample.

Compared to other renowned spectroscopic technique, *e.g.* FT-IR, Raman spectroscopy diffusion had deeply suffered from the lack of highly bright light sources because of the very low signal-to-noise ratio it offers. The blossoming technologies of lasers, charge-coupled detectors and filters had significantly enlarged the horizons of this non-destructive, highly sensitive and informative vibrational spectroscopy across the fields of chemistry, biology, physics, geology, pharmacology, forensics, pharmaceuticals, materials science, cultural heritages and others.[125]

Amid this large landscape of possibilities, from the standpoint of this work the foremost interest for deploying Raman spectroscopy

is the opportunity to obtain information-dense spectra of proteins. The perspective for a Raman characterization of proteins has been first drawn by Edsall back in 1938[126] but 20 years had gone before the very first spectrum of lysozyme had been achieved.[127] An actual structural interpretation could be advanced a dozen years later once Tobin,[128] Lord and Yu[129,130] provided the earliest laser-powered Raman spectra of proteins. The laser era, alongside the collection of Raman spectra from protein crystal, granted a fair increase in the signal-to-noise ratio allowing the first steps towards the Raman-based structural investigation of proteins. Resonance Raman (**RR**) spectroscopy came next, first on rhodopsin from bovine retina,[131] then on metallo-proteins paving the way for the fruitful haemoprotein branch.[132-135] It consists in the large enhancement of the Raman signals by using exciting wavelength in the absorption range of the sample.[136]

Several Raman-active vibrational modes serves as fingerprints for the structural analysis of peptides at sub-atomic resolution as the precise wavenumbers of many bands strongly depend on inter- and intra- molecular effects *e.g.* peptide-bond angles and hydrogen-bonding patterns, permitting a sensitive interpretation of the secondary structure arrangement.

The secondary structure interpretation mostly relies on the amide bands position and shape: nine normal modes are allowed for the amide band of proteins that are named A, B, and I to VII in order of decreasing wavenumber and reveal the main polypeptide chain structure regardless the contributions from side groups.

The Amide A and B (from the NH stretching mode, around 3500 and 3100 cm^{-1} respectively)[137] are usually little informative as they both fall in the region of the Raman-active water region (ν_1 OH stretching).[137,138]

The most informative amide I band (C=O stretching mode), almost entirely buried under the ν_2 OH bending modes of water at IR analysis, is clear at Raman spectroscopy.[139] On the contrary, the amide II band, from the N-H bending and the C-N stretching in the 1480–1580 cm^{-1} range is barely Raman-active and usually of little relevance in the interpretation of complex spectra. Amide III band, 1230-1330 cm^{-1}, arises from the C-N stretching and from the N-H bending and represents a useful fingerprint for the secondary structure besides the amide I. The remaining amide bands (IV - OCN bending, V - out-of-plane NH bending, VI - out-of-plane C=O bending and VII - skeletal mode) exhibit very weak activity and are usually hidden by other spectral features from the amino acids side chains.[138,139]

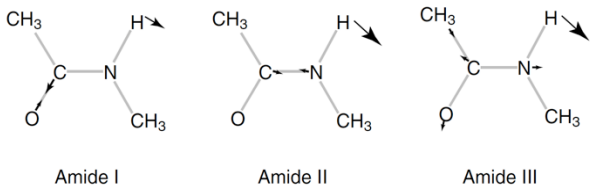

Figure 3 – Scheme of Amide I-III modes.

In addition to the amide bands, many other spectral features referring to the amino acid side-chains are indeed clearly apparent. The side-chain vibrational modes of aromatic residues have been pin-pointed by Harada and Takeuchi.[140] The Raman bands around 1360 and 1340 cm^{-1} are known as the tryptophan doublet, and its relative ratio, I_{1360}/I_{1340}, reflects the hydrophobic/hydrophilic environments of the Trp residues.[141] Another band around 880 cm^{-1} is representative for the Trp and their environ.[141] Two features at 860 and 830 cm^{-1} are diagnostic for the tyrosine and their local microenvironment. The couple is known as the Tyr doublet and arises from the in-plane breathing of the and out-of-plane deformation modes.[142] Raman spectroscopy is also very sensitive towards the sulphur-containing residues and their relative

conformations. In the low frequency region, the *ggg* conformations generates spectral features around 508-512 cm^{-1} whereas the *tgg* at 523-528 cm^{-1} and the *tgt* at 540-545 cm^{-1}.[138] Sulphur-containing methionine residues can be detected within the range 700-725 cm^{-1} but these are fairly unlinked from the conformation.[138]

Raman spectroscopy is useful also for acquiring information related to the primary structure of proteins, *e.g.* to detect the selenio-methionine incorporation.[143] It serves as a non-destructive and selective fingerprint for the tertiary structure as well. Indeed, Raman spectroscopy has been deployed to obtain information particularly related to the active site of enzymes.[144,145] Intermolecular interactions can be surveyed withal, like ligands binding or enzymatic catalytic processes.[146,147]

Anyhow, although Raman spectra provide such a powerful information-dense data batch, when it comes to protein structure none compares to X-ray crystallography. Since the first haemoglobin and myoglobin structures have been Noble Prize awarded in 1962,[148] the X-ray crystallography dominion remains uncontested and, to date, the Protein Data Bank accounts for some hundred twenty thousand crystallographic records.[149]

Briefly, the X-rays radiation spans from 10 to 10^{-2} nanometres and the typical wavelength adopted for crystallography is around 1 Å (10^{-1} nm), which is on the scale of covalent chemical bonds and the radius of a single atom. Incident photons thus get elastically scattered by electrons in the atomic shells. Scattered photons mostly elide each other by destructive interference, a few specific scattering directions satisfy the Bragg's condition[150] (Figure 4) and produce constructive interference

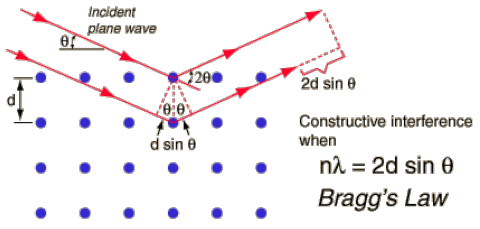

Figure 4 – Scheme for the Bragg's diffraction condition.

instead that translate into reflexes on the detector. Each reflex gets indexed using Miller indices (hkl), representative for the vector whose length equals the reciprocal of the distance between the Bragg's planes that originated the reflex itself.

The Fourier transform to follow re-enacts the relationship between each Miller's vector with hkl coordinates and the electron density (σ) in the real space:

$$\sigma_{hkl} = \frac{1}{V}\sum_{hkl}\left|F_{(hkl)}\right|e^{(i\alpha_{hkl})}e^{[-2\pi i(hx+ky+lz)]}$$

with V being the volume of the crystalline unit cell, $\alpha_{(hkl)}$ the phase associated to the structure factor amplitude $|F_{(hkl)}|$: this latter is experimentally measured while the phase is not, setting up the phase issue that can be addressed with different methods, described elsewhere.[151-153] By iterative stages, the protein model structure gets refined at nearly atomic resolution giving unmatched structural details. Anyway, the final three-dimensional model, hence the information one can retrieve form it, suffers from technical and theoretical limitations as well as potential data misinterpretations, mostly depending on quality of the crystal.

Resolution is usually the most limiting variable defining the impassable limit for the atomic coordinates, and for structure above 1.2 Å it is virtually impossible to determine the coordinates for hydrogen atoms. Moreover, X-ray crystallography not always allows to unambiguous discern between atoms with close Z number, such as oxygen from nitrogen or even carbon, and their assignment within the electron-density maps are mostly deductive. As a consequence, the actual a certain degree of ambiguity challenges the crystallographer to a reasoned interpretation. Is that a water or a metal atom? The complexity arises as the number of deducible information lessen, for example in the interpretation of ligands and their interaction modes.

In addition to the intrinsic uncertainty of atom coordinates addressed by the resolution value, most of the proteins usually do not strictly comply to the ideal highly-ordered definition showing intrinsic disorder as some regions of the molecule may adopt different and sufficiently stable conformations in different copies of the molecule. Some protein domains, *e.g.* large loops and random coils segments, are so much intrinsically disordered that it is impossible to define any proper crystallographic model sometimes. Major advances in the chase of higher and higher resolution limits and data quality have been achieved by synchrotron light sources, which guarantee highly intense, collimate coherent radiation. Anyhow, this came with a trade off in terms of increased photodamage, a worrying crystallographic issue though cryo-cooling techniques partially addressed the problem.[154]

Third and fourth generation synchrotron beam lines rapidly warp the diffractive capacity of the protein crystal resulting in two sort of damage even under cryo condition: global and specific. The former reveals through diffraction quality decay in terms of highest resolution shell loss, unit-cell volume expansion, reduction of the signal-to-noise ratio and increased mosaicity. On the contrary, specific damage concerns the electron density surrounding specific atoms and/or portions of the protein structure.[155]

Disulphide bonds gets very rapidly distorted, reduced, and broken eventually, aspartates and glutamates are decarboxylated, methionine suffer for S-C cleavage and tyrosine may possibly, though yet disputed,[155] lose their OH group.[156-164] Utterly, these individual events may prompt severe global structural modifications and mislead the experimental interpretation.[154,165,166]

The jointing limits and strengths of Raman spectroscopy and X-ray crystallography draws for a solid reciprocal supportive integration,

which has begun to establish in recent years as Raman-assisted crystallography (RAC).[167]

Macromolecular crystals indeed provide very good conditions for efficient Raman protein spectra collection because of their very high protein concentration (can be assumed at an upper limit). As aforementioned and in addition to, Raman spectroscopy is relatively little affected by the solvent usually, and represent a very well suited complementary tool to X-ray crystallography.

The Raman-assisted crystallography is being deployed for an increasing variety of purposes. It served for identifying intermediates of the reaction catalysed by the superoxide reductase,[147] proving selenium-containing methionine incorporation prior anomalous scattering experiments,[143] or for monitoring the ligand binding/release within the protein crystal and its modification.[18,168,169]

2

Spotting Hg^{2+} within protein crystals

> *"A complex system that works is invariably found to have evolved from a simple system that worked. A complex system designed from scratch never works and cannot be patched up to make it work. You have to start over with a working simple system.*
>
> *-The Gall's Law-"*

This section describes a simple yet very effective Raman-based approach to detect the insertion of mercury ions into cysteine pairs within protein single crystals, as a first step toward proving know-how, technical set-up a feasibility of the RAC approach. The method has been developed using bovine insulin as the model system by applying an effective mercuration protocol: a TCEP-induced disulphide bridges reduction within the crystal, is followed by an overnight reaction with a $HgCl_2$ solution producing Hg-derivative crystals. Raman spectra collected on these derivative crystals, kept in the mother liquor, reveal a characteristic Raman band that has been assigned to a -S-Hg-S- bridge formation. This analysis provides Raman-based markers for the mercury binding to cysteines and further proves the reliability of the Raman-based approach for the detection of interacting metals with protein systems, as well as providing precise structural information as confirmed by comparison with X-ray clues.

2.1 Introduction

Protein crystals distinguish themselves in the crystalline world because of their very high solvent content (up to 60%) compared to small molecule crystals, making of them gel-like rather than a classic solid, and must be constantly dunk in their mother liquor or will dissolve otherwise upon drying.

Derivative protein crystals are prepared either via co-crystallization of protein and reactant or via reactant soaking from the mother liquor into the protein crystal through the large solvent-accessible channels within the solid phase.

Metal binding to proteins is an open research field in crystallography and the adoption of microspectroscopic techniques, including Raman spectroscopy, are constantly thriving and spreading over this bio-structural research areas.

Both inorganic[170] and organic[171] mercury compounds, such as Hg^{2+} ions, methyl- and ethyl- mercury,[172] are known since long as toxic agents in several poisoning mechanisms e.g. alteration of cell membrane permeability,[173] non-specific inhibition of several enzymes, synaptic transmission and neural fibre degeneration, nephrotoxicity, alteration of cholinergic neurotransmission functionalities, immuno-toxicity, and reduction of haemoglobin's oxygen-carrying capacity.[174] Finally, they are also likely carcinogenic, even though yet not completely demonstrated due to the need for long term data collections.[175]

Mercury toxicity mechanisms essentially link up with two main types of actions: i) protein binding (enzymes, receptors, structural proteins etc.), and ii) interaction with nucleic acids.[176,177] In particular, numerous toxic effects of both organic and inorganic mercury compounds are attributable to the capability of these

substances of interacting in different ways with the side chains of protein residues, causing a number of effects.

Among the many possible interactions of mercury compounds with protein atoms, the most common is through the binding with sulphur atoms of cysteines, resulting in relatively stable Hg-cysteine complexes. The formation of such complexes has been demonstrated to alter the protein folding seriously.[177-179]

Valuable information on Hg^{2+} reactivity with amino acid side chains comes from fundamental bioinorganic studies, which had demonstrated the formation of $^{+}$Hg-S-Cys and Cys-S-Hg-S-Cys complexes either, mostly depending on the proximity of the cysteines. On the other hand, because of the presence of the alkane chain, organic compounds do not form –S-Hg-S- bridges. For example, in the case of methylmercury, H_3C–Hg–S–Cys forms are well known for the mammalian thioredoxin system.[180]

Although Hg^{2+} preferentially reacts with –SH groups, it is known to react with different side chains as well. Evidences for the interaction of Hg^{2+} with histidine has been collected since 1950s. Because of the relationships between histidine and histamine, widely involved in local immune responses, Hg^{2+} poisoning triggers severe immune system diseases.[179] Furthermore, oxygen atoms of Asp and Glu residues COO^{-} groups are highly sensitive target towards mercury as the carboxyl group readily reacts with almost any mercury compound forming organo-mercury salts. Amide residues are known to have a key role in Hg–DNA binding[181] and amide groups of amino acid residues are potential binding targets as well, thus making virtually any protein liable for mercury attack.

Herein, the bovine insulin crystals have been adopted as model system. It differs from its human counterpart only in three amino acid residues, is composed by two polypeptide chains: chain A has 21 amino acids and chain B has 30 amino acids. *Two disulphide*

bridges (between residues A7 and B7, and A20 and B19) covalently tether the chains. Moreover, chain A contains an internal disulphide bridge (between residues A6 and A11 - Figure 5). Notably, the position of these three disulphide bonds is invariant in mammalian forms of insulin making of it perfectly fitting for the extent of this work *i.e.* the definition of a simple practical protocol for detecting the Hg^{2+} insertion into protein crystals via Raman microscopy.

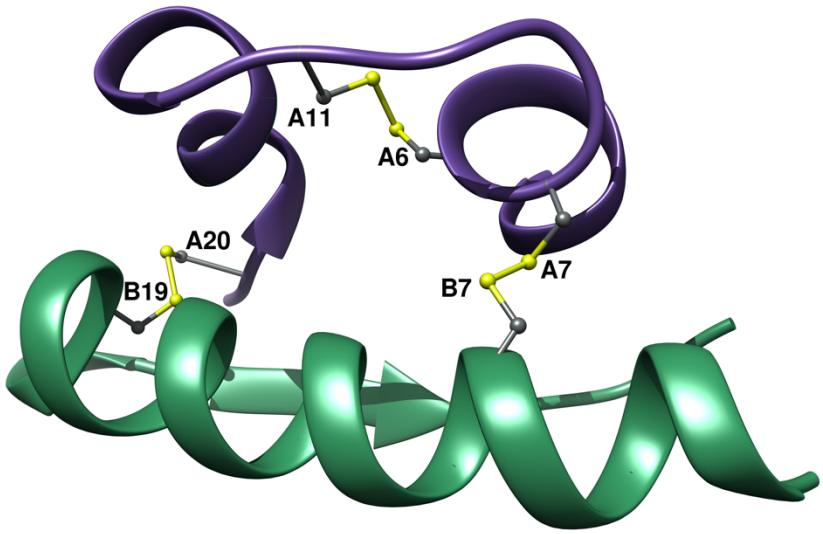

Figure 5 - Cartoon representation of the bovine insulin structure (PDB code 1ZEH), chain A is dark purple, chain B green. Disulphide bridges are also shown as balls and sticks.

2.2 Experimental

Crystals of bovine insulin had been grown using the vapour diffusion hanging drop method. Crystallization conditions had been optimised starting from condition reported in literature for the human variant.[182] Very well-shaped but tiny crystals grew in these conditions (≤30 μm) but much larger crystals had been successfully obtained by "poisoning" with Tacsimate, which slows down the crystallization process and therefore prompts a noticeable increase of crystal size (>100 μm).

Optimal crystallisation condition had been identified and best crystals have been obtained from crystallisation solutions containing 3% v/v acetone, $5 \cdot 10^{-2}$ mol L^{-1} sodium citrate at pH 6.3, 10^{-3} mol L^{-1} $ZnCl_2$, 5% v/v Tacsimate at pH 7.0, all at a 1:1 protein-to-reservoir ratio in 1 μL drops and using an initial bovine insulin concentration of 0.5 mg mL^{-1}.

These crystals diffracted X-rays at about 2 Å resolution and have a solvent content as high as 35%.[183]

A two-step mercuration protocol has been adopted: first, the S-S bridges reduction to the highly reactive free –SH thiol groups by using a $8 \cdot 10^{-2}$ mol L^{-1} solution of tris[2-carboxyethyl]phosphine chloride (TCEP) as reducing agent, whose pH had been adjusted to 7.0 by NaOH addition, as previously reported.[182] Reduced crystals had been handled and stored in an oxygen-free atmosphere (nitrogen box at 1 ppm O_2) in order to prevent re-oxidation. Crystals had been soaked overnight in a saturated aqueous solution of $HgCl_2$ and $2 \cdot 10^{-2}$ mol L^{-1} sodium citrate at pH 6.3.

Raman data had been collected using a commercial JASCO NRS-3100 Raman microscope system and either a 514 nm and 647 nm laser lines from Ar^+ and Kr^+ tubes, respectively. Laser power at

the sample has been kept as low as 1 mW to keep any chance of photo-dissociation phenomenon out.

Raman spectra acquired for bovine native insulin crystals, TCEP-reduced and upon Hg^{2+}-soaked crystals are reported in Figure 6 (see below). To account for possible background interferences, the spectrum of the mother Raman spectra of the mother liquor are also reported.

The prominent protein features include the Amide I band located at around 1659 cm^{-1}, which is a signature of the α-helix insulin secondary structure[184] and a 1680 cm^{-1} shoulder related to the ß-sheet secondary structure,[182] the CH_2/CH_3 bending vibration at 1448 cm^{-1}, Amide III in various conformations at 1268 and 1207 cm^{-1}, C–N stretching at 1026, 1058, 1090, 1123 and 1154 cm^{-1}, ring vibrations of the phenylalanine moiety at around 1000 cm^{-1}, and a prominent peak at 508 cm^{-1} assigned to the disulphide S-S stretching mode. Deepening, the peak at 508 cm^{-1} relates to the gauche–gauche–gauche (*ggg*) conformation of the three torsional angles in the C-S-S-C groups, according to PDB entries 2A3G and 4E7T and literature.[185]

It is worth noting that the initially well-diffracting insulin crystals become totally disordered upon TCEP reduction (data not reported). Raman analysis clearly shows the reason for such a tremendous drop of crystal quality since, upon the addition of TCEP, the amide bands are replaced by a single ß-sheet marker band at 1673 cm^{-1}. This spectral change is assigned to an α-helix to ß-sheet transition occurring upon reduction of the disulphide bridges, in agreement with earlier reports from human insulin.[182]

Concomitant with this secondary structure transition, the 508 cm^{-1} band, clearly visible in the native crystal spectrum, becomes featureless in the reduced form, consistently with the S–S reduction to SH groups.

Upon Hg^{2+} soaking, the Amide I band at 1673 cm^{-1} is still present, indicating that mercuration does not affect the secondary structure, but a new very intense spectral feature appears at 335 cm^{-1} (Figure 6). This band has been assigned to the -S-Hg-S- stretching, in agreement with previous studies performed on cysteine crystals and solutions, where the -S-Hg-S- mode has been reported to be at 334 cm^{-1},[186] and on various mercapto-compounds, where the -S-Hg-S- mode has been reported to occur in the range 290-390 cm^{-1}.[187]

This study is a valuable reference for Hg^{2+} binding to two Cys residues within a protein crystal. The 335 cm^{-1} Raman band is detectable with ease even using low laser power, as in this work to reduce any risk of photo-dissociation, because this band characterises for a very high intensity, remarkably comparable to Amide I band arising from the contribution of fifty amide bonds

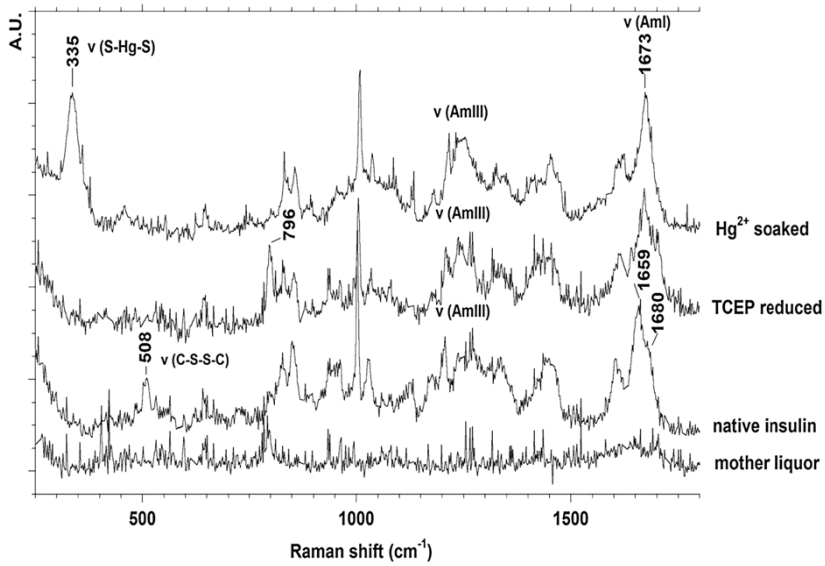

Figure 6 - Raman spectra of bovine insulin crystals. In the native insulin spectrum, a clear band at 508 cm^{-1}, referred to S-S stretching, and a band at 1659 cm^{-1}, related to an α-helix Amide I, are present. Because of the reduction of S-S bridges to SH groups, TCEP addition causes the disappearance of the 508 cm 1 band in the corresponding spectrum. In both TCEP and Hg^{2+} soaked insulin spectra, a single ß sheet related band at 1673 cm^{-1} is observed, due to an a-helix to b-sheet transition. A band at 796 cm 1 is visible only in the TCEP reduced spectrum and is likely due to TCEP itself. The spectrum of the precipitating solution, where the crystal is always kept, is also reported as ''mother liquor''.

whereas only three –S-Hg-S- bridges can be formed per insulin molecule. The high Raman intensity of the -S-Hg-S- band probably relates to the presence of the highly polarisable heavy atoms Hg and S, hence triggering very high Raman cross-sections confirming Raman spectroscopy as a very sensitive technique for the detection of mercury binding, even for a low Hg^{2+}/residues ratio, bearing in mind the very low mean content of Cys residues in proteins, as low as 3%.[188]

Two different laser lines had been deployed (514 and 647 nm) to rule out line-related dissociation phenomena (Figure 7). Anyhow, the spectra obtained by exciting with 514 and 647 nm are extremely similar as they both show the same very intense band at 335 cm^{-1}. However, it should be stressed that this Raman marker is likely to apply only to -S-Hg-S- bridges, and that specific markers for free SH groups producing S-Hg^{+} species need further investigation. No additional bands, potentially due to different Hg^{2+} binding modes, had been observed.

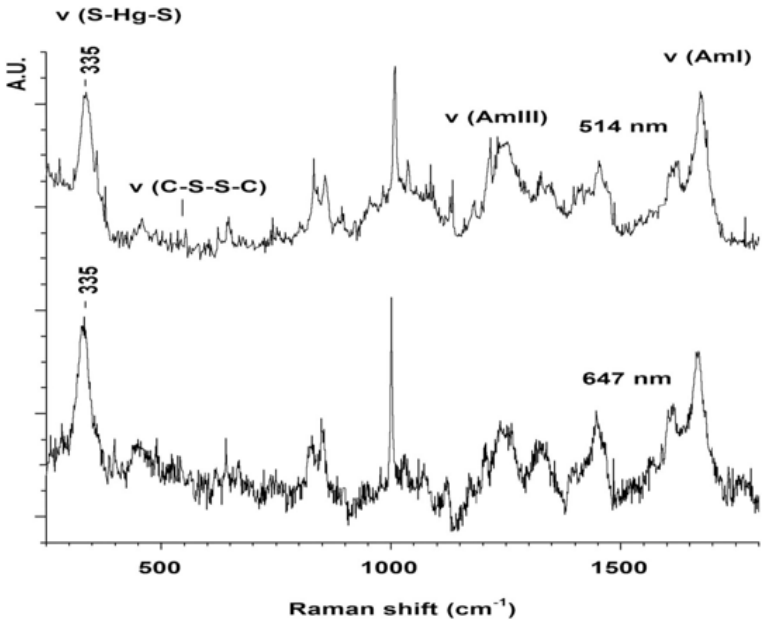

Figure 7 - Comparison of Raman spectra of Hg^{2+} soaked crystals obtained by using the 514 nm laser line (upper curve), and the 647 nm laser line (lower curve). No appreciable difference is observed. In agreement with previous results, the -S-Hg-S- band at 335 cm^{-1} is present in both spectra with almost the same intensity.

2.3 Conclusions

This Raman microspectroscopy study on bovine insulin single crystals provides simple and effective mercuration protocol via prior TCEP-induced reduction of disulphide bonds. It also provides a sensitive experimental method to detect Hg^{2+} binding into cysteine pairs by recognising a very strong Raman band around 335 cm^{-1} as a marker for -S-Hg-S- bridge formation.

Further application of such procedure to free cysteines could be of interest for the preparation of isomorphous derivative crystals, often used in protein crystallography.

At last, the crystallographic findings on spoiling of the crystal diffracting power upon reduction could be explained trough Raman spectroscopy, which gave evidences for the $\alpha \rightarrow \beta$ transition.

3

Rac for Photodamage Detection

“...light creates,
light preserves,
light destroys…
-PJ Bailey, Festus-”

…and though the light itself cannot even sketch up a crystal, as sure as death can destroy it. And we had lit up a crystal to cast light on the highly relevant, yet not completely established mechanisms of X-ray radiation damage on protein structure. This section addresses for the innovative adoption of Raman microspectrophotometry to follow the X-ray induced chemical modifications on the structure of the model protein bovine pancreatic ribonuclease (RNase A). The combination of dose-dependent Raman spectra and ultrahigh resolution (eight structures between 0.85 and 1.17 Å) allowed to the direct observation of several radiation damage events, including covalent bond breakages and radical species formation. This work provides relevant qualitative and quantitative results for a deeper understanding of the X-ray induced photodamage on single protein crystals, as well as Raman markers for its detection, possibly paving the way for a novel effective supportive method for X-ray data collection at synchrotron beam lines.

3.1 Introduction

Major advances in the chase of higher and higher crystallographic resolution limits and data quality have been achieved by synchrotron light sources, which guarantee highly intense, collimate coherent radiation. Anyhow, this came with a trade off in terms of increased photodamage, a worrying crystallographic issue even though cryo-cooling techniques partially addressed the problem. For decades, structural changes induced by the radiation damages have been unrecognized but, once systematic studies have been performed, it has been shown how these events may affect the process of structural solution and the quality of the refined models. X-ray induced photodamage is a phenomenon caused mainly by **a)** the direct interaction between molecules in the crystal and the beam and **b)** the reactivity of radicals formed and propagated throughout the crystal. Two distinct indicators of damage as a function of dose have been identified in terms of global and specific damage.[189] The former results in a loss of the measured reflections at highest resolution shells, decrease of the I/σ ratio, variation of unit-cell volume, increase of the Rmerge or Rsym values, which measure the internal consistency of X-ray diffraction data, increase of the Wilson B-value for the data and of atomic displacement parameters (B-factors) of the atoms in the refined model, rotation of the molecule within the unit cell and often an increase in crystal mosaicity. Specific damages include the appearance in solved structures of artefacts possibly affecting the interpretation of protein biological functions,[190,191] like side-chain structural and chemical modifications, disulphide bond breakage ionization,[159,160,192,193] metal reduction,[194] ligand photodissociation.[195] Raman spectra of a protein represent molecular normal modes of vibration and can be used as a sensitive, non-destructive and

selective fingerprint for protein primary,[196] secondary,[138] and tertiary structure especially related to active sites,[144,197] of intermolecular interactions and dynamics *e.g.* ligand binding and enzyme reactions.[147,198] Coupled with X-ray crystallography, Raman microscopy can yield subtle in-crystallo information about the status of chemical events that occur in the crystal, including X-ray induced chemical modifications.[55,168,195,196,199,200] Few examples of Raman microscopy detection of radiation damages have been published: these studies mainly focus on Br dissociation from DNA[201] and disulphide bridge reduction.[199] On the basis of this work, a mechanism of disulphide bridge repair has been also proposed.[199] This joint approach has been also adopted for assessing the structural bases for a transient X-ray induced photo-bleaching in a green fluorescent protein.[202] In 2013, the first Raman-assisted crystallographic evidence of the X-ray induced NO-photodissociation at a 3rd generation synchrotron (Swiss Light Source) has been reported.[195]

Herein we use a combined crystallographic-Raman microscopy experiment to address the effect of an increasing radiation dose on the structure of the model protein bovine pancreatic ribonuclease (RNase A), in a cryo-cooled crystal. The section provides the Raman markers of photodamage, including methionine demethylation and decarboxylation of Asp/Glu residues. RNase A has been chosen as subject of our study since it has been used as a model protein in a number of different fields,[203] including folding,[204] protein synthesis,[205] enzymology,[206] protein aggregation[207] and protein metalation[17,208-210] and has already been used to study the effects of X-ray dose on protein structure (PDB code 2BLP);[211] it is commercially available at high purity and has small size (124 residues). The protein contains four disulphide bridges, no Trp

residues and its crystals diffract at ultrahigh resolution (between 0.85 and 1.17 Å) even after extensive damages have occurred.
This work is particularly addressed to those analytical applications in which Raman microspectroscopy assists X-ray crystallography.[212] Currently, several facilities allocate Raman microspectroscopy online with X-ray beamlines. Ultimately, herein a Raman-based protocol of X-ray induced photodamage is proposed, whose spectral assignments have been supported by ultra-high resolution crystallographic data collected at different X-ray dose.

3.2 Methods

3.2.1 RNase A Crystallization

RNase A crystals have been prepared as previously described.[213-215] Briefly, lyophilized protein was dissolved in 20 mM sodium citrate pH 5.3 and used at a concentration of 30 mg/mL. The protein was inserted into glass capillaries, frozen at -20 °C to obtain a clear interface where 10 µl precipitating solution of 99.9% isopropanol was loaded. For cryo-protection, a crystal has been transferred to a solution containing 60% isopropanol, 20 mM sodium citrate buffer pH 5.3 and 15 % (v/v) glycerol and kept there for one minute.

3.2.2 X-ray data collection and refinement

Diffraction data on a single crystal were collected at the PXII beamline of Swiss Light Source (SLS) at eight different X-ray doses, i.e. between 2 and 24 MGy. Data collection statistics are reported in Table 2. The X-ray dose has been evaluated by using the software RADDOSE.[216] The crystal diffracts at ultrahigh resolution (0.85 Å) and even when it receives a dose of 24 MGy, a complete data set has been collected at quasi-atomic resolution (1.17 Å). All data sets have been collected at 100 K using glycerol as cryo-protectant and processed with the HKL-2000 program suite.[217] The refinements have been performed using SHELX-L.[218] The structures anisotropically refine to values of R_{factor} and R_{free} in the range 0.09-0.16 and 0.12-0.23 respectively. Details on refinements statistics are reported in Table 1.

Radiation damage has been identified by inspecting the 2Fo-Fc, Fo-Fc and Fo-Fo electron density maps and calculating both B_{damage} and $B_{effective}$, as recently reported by Garman and coworkers.[219,220] B_{damage} and $B_{effective}$,[219] have been evaluated using both models refined

isotropically and anisotropically. When multiple conformations of a residue are present, they had been replaced by the highest occupancy conformation.

Table 1 – Refinement statistics. Values in brackets refer to the highest resolution shell.

Dose	2	5	8	11	14	17	20	24
Resolution (Å)	50[0.85]	50[0.85]	50[0.92]	50[0.92]	50[1.02]	50[1.02]	50[1.08]	50[1.17]
Working set (N.)	74099	77419	64628	59671	47263	41368	30341	23647
Test set (N.)	3888	4106	3415	3131	2455	2165	1559	1251
Rfactor (%)	11.61	9.77	10.60	11.13	13.18	14.01	15.00	16.11
Rfree (%)	14.98	12.22	13.63	14.10	16.53	17.80	21.52	23.14
Rall (%)	12.14	10.28	10.89	11.66	13.45	14.56	16.09	17.34
Non-hydrogen atoms (N.)	1377	1390	1398	1351	1345	1303	1301	1195
Mean B-value ($Å^2$)	15.57	15.28	16.74	17.09	19.17	19.13	21.02	19.16
Ramachandran statistics								
Favoured (%)	98.4	98.4	97.5	97.5	97.5	97.5	97.5	97.5
Allowed (%)	1.6	1.6	2.5	2.5	2.5	2.5	2.5	2.5
Outliners (%)	0	0	0	0	0	0	0	0

Table 2 - Data collection statistics of RNase A crystal at different X-ray dose. Values in brackets refer to the highest resolution shell.

Dose (MGy)	2	5	8	11	14	17	20	24
Space Group	p21	p21	p21	p21	p21	p21	p21	p21
a (Å)	29.12	29.16	29.18	29.21	29.24	29.25	29.25	29.26
b (Å)	37.97	37.96	38.04	38.06	38.09	38.10	38.09	38.09
c (Å)	52.54	52.72	52.65	52.72	52.77	52.80	52.82	52.82
α (°)	90.00	90.00	90.00	90.00	90.00	90.00	90.00	90.00
β (°)	105.83	105.80	105.85	105.88	105.88	105.89	105.91	105.91
γ (°)	90.00	90.00	90.00	90.00	90.00	90.00	90.00	90.00
Cell Volume (Å^3)	55900.2	56151.7	56221.5	56390.3	56516.0	56580.8	56614.6	56600.7
Res. limits (Å)	50-0.85 [0.88-0.85]	50-0.85 [0.88-0.85]	50-0.92 [0.95-0.92]	50-0.92 [0.95-0.92]	50-1.02 [1.06-1.02]	50-1.02 [1.06-1.02]	50-1.08 [1.12-1.08]	50-1.17 [1.21-1.17]
Observations	297362	314305	496316	335098	363201	183087	136313	102155
Unique observations	92774 [8302]	95598 [9346]	76213 [7459]	73777 [7198]	54830 [5380]	51404 [4981]	41153 [4029]	32132 [3153]
Completeness (%)	96.0 [86.2]	97.8 [95.9]	98.7 [97.4]	96.2 [94.2]	98.9 [97.7]	91.9 [89.6]	88.7 [87.6]	88.1 [86.5]
Average multiplicity	3.2 [2.6]	3.3 [3.2]	6.5 [6.7]	4.5 [4.6]	6.6 [6.4]	3.6 [3.4]	3.3 [3.3]	3.2 [3.1]
Rmerge (%)	0.067 [0.387]	0.047 [0.353]	0.075 [0.440]	0.050 [0.471]	0.094 [0.451]	0.056 [0.431]	0.07 [0.57]	0.07 [0.47]
Mosaicity	0.304	0.335	0.356	0.396	0.437	0.436	0.461	0.471
I\σ	8.3 [2.2]	38.7 [2.5]	11.25 [3.89]	9.89 [2.53]	10.15 [4.29]	8.65 [2.47]	8.12 [2.48]	7.90 [2.29]

3.2.3 On line Raman microscopy

To precisely follow the progress of X-ray-induced structural damage on crystalline RNase A, Raman spectra have been collected prior and after each X-ray diffraction data collection, restoring each time the same crystal orientation, using an on-line Raman spectrometer setup, the upgraded version of the as previously described system.[221] The spectra have been recorded using 785 nm laser light excitation.

3.3 Results and discussion

3.3.1 Raman microscopy

X-ray diffraction data collection assisted by online Raman acquisition, prior and after data collection, have been performed. Non-resonant Raman spectra of RNase A before and after eight successive data set are shown in Figures 8 and 9 whereas details are reported in each residue-specific section (see below). The high signal-to-noise ratio of the spectra originates from the high protein concentration in the crystal, the low solvent content, and the cryogenic temperature (100 K). The spectra display a series of bands that, based on previous assignments,[130,222] report on vibrational modes associated with disulphide bonds (522 cm^{-1}), methionine (665 and 724 cm^{-1}), acidic residues (Glu and Asp, 1410 cm^{-1}), as well as backbone amide bonds (amide I band around 1650 cm^{-1}, not shown). At increasing adsorbed dose, by comparing successive Raman spectra (prior and after X-ray exposure), multiple Raman markers indicate the occurrence of photochemical events. Indeed, the intensity of several Raman bands associated to the aforementioned side chains decrease, while novel Raman bands appear possibly due to the formation of photoproducts. Some Raman bands from residues expected to be unaffected (e.g. the band at 1007 cm^{-1} arising from the angular bending of the Phe ring),[223] shows to be actually dose-independent and hence taken as internal quantitative standard for spectral normalisation. Amide band for all the collected spectra are invariably at 1650 cm^{-1} (data not shown), coherently with no change in the secondary structure as confirmed by electron density maps. Sections 3.3 reports on how these photochemical damages can be associated with the breakage of disulphide bonds, decarboxylation of acid residues (Asp and Glu and C-terminus), and breakage of covalent C-S bonds in Met. X-ray

induced modification via Raman microscopy, and in terms of ultrahigh resolution crystallography.

A possible involvement of Tyr side chains appears unlikely, since electron density maps do not indicate significant modifications of the side chain of Tyr residues, in agreement with data by Gerstel et al.[219]

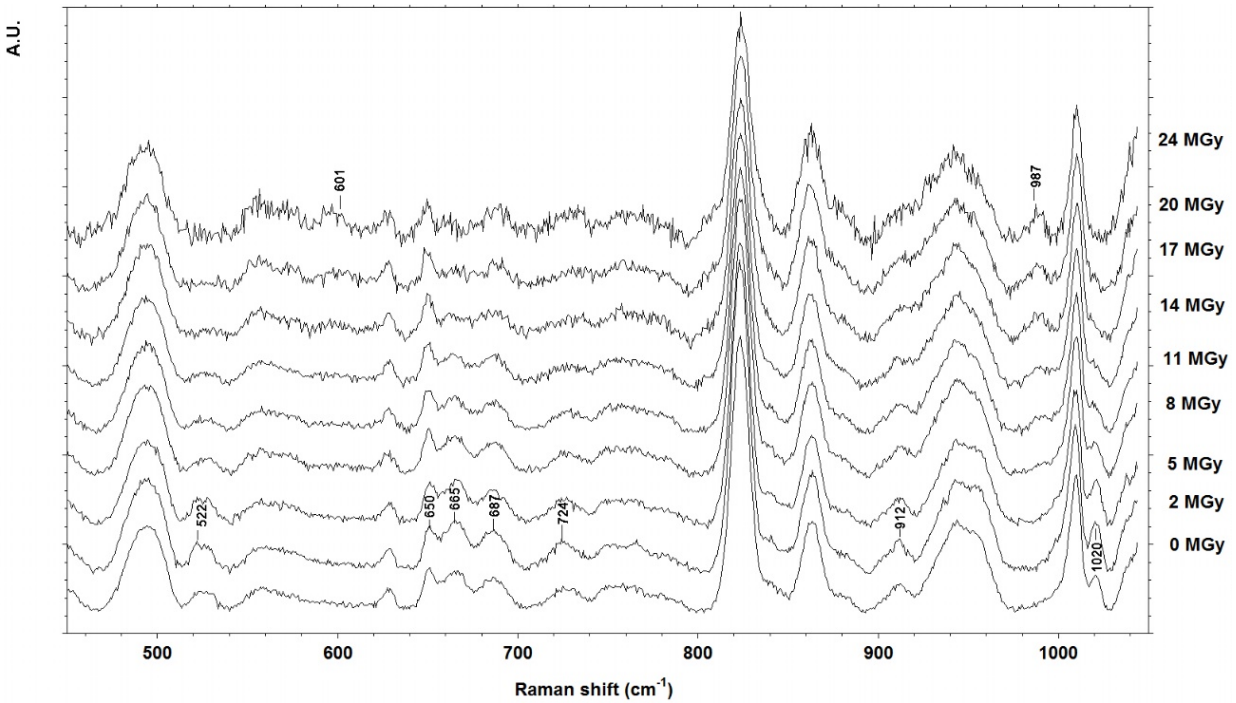

Figure 8 - Low frequency non-resonant Raman spectra of RNase A crystals as function of absorbed X-ray dose. Excitation line is 785 nm (10 mW at the sample), exposure time 120 s. Spectral resolution 8 cm^{-1}. Raman spectra are normalised with Phe signal at 1007 cm^{-1} as a reference.

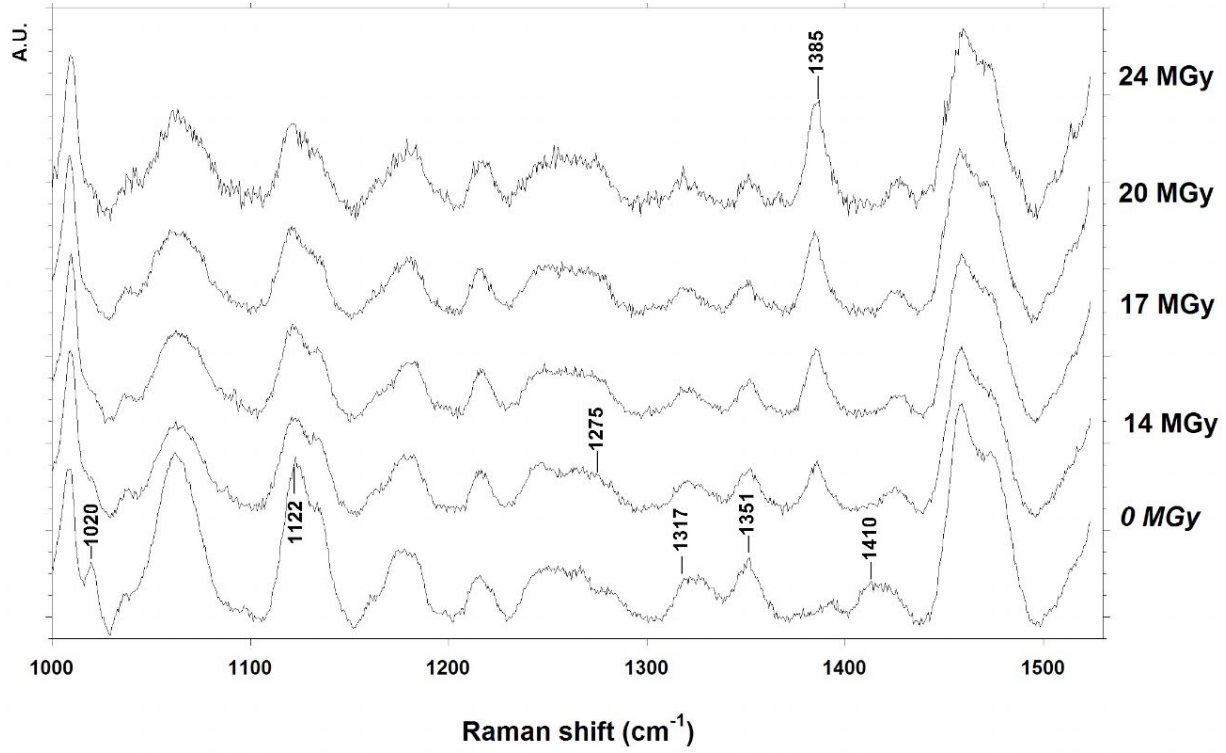

Figure 9 - Medium frequency non-resonant Raman spectra of RNase A crystals as a function of absorbed X-ray dose. Excitation line is 785 nm (10 mW at the sample), exposure time 120 s. Spectral resolution 8 cm^{-1}. Raman spectra are normalised towards Phe signal at 1007 cm^{-1}.

3.3.1.1 Disulphide bonds

Raman band at 522 cm^{-1}, typically assigned to -S-S- stretching in a *ggt* conformation,[224] decreases as dose arises (Figure 10) suggesting the disulphide bond breakage. Raman-assisted crystallography breakage of disulphide bridge has been already characterized in previous works.[199]

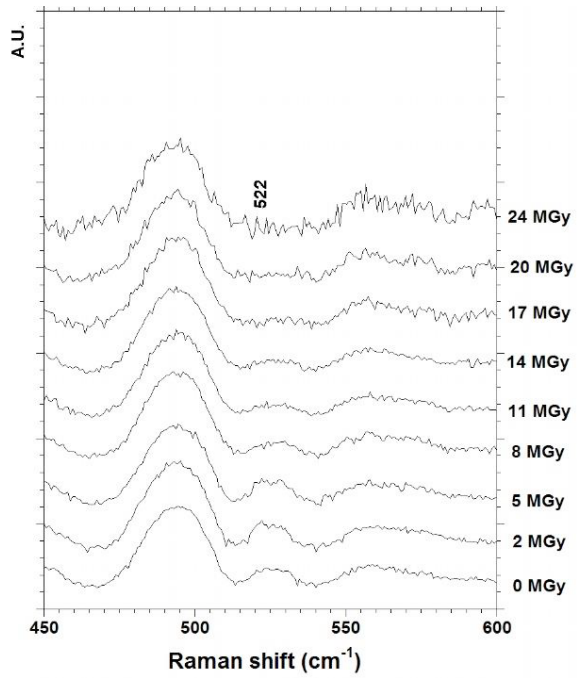

Figure 10 - Detail for the rapidly decreasing band at 522 cm^{-1} related to the –S-S- modes of disulphide bridges.

3.3.1.2 Aspartic and Glutamic residues

Both Asp and Glu residues are expected to suffer for decarboxylation as dose arises[159,160,162,193] leading to CO_2 release eventually. Raman spectra do highlight the decarboxylation event occurring for both Asp and Glu residues (Figure 11): a fast decreasing band (disappearance over 14 MGy) at 1410 cm^{-1} has been assigned to -CO_2^- groups, whereas two appearing bands at 1275 and 1385 cm^{-1} possibly refer to the CO_2 related vibrations (lower and upper Fermi dyad band, respectively). The arising 1385 cm^{-1} band has been interpreted as relating to the •CH_3 photoproducts. This band can be used as diagnostic of Asp and Glu

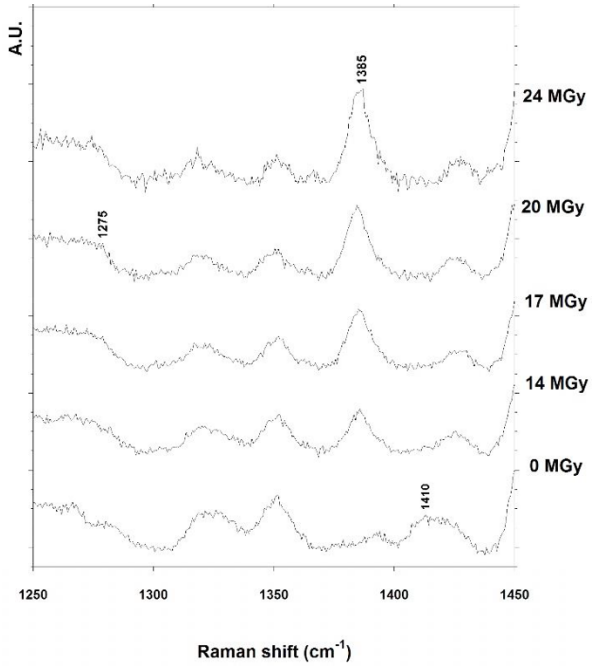

Figure 11 – Medium frequency non-resonant Raman spectra showing the decrease of the 1410 cm^{-1} band from Asp/Glu -CO_2^- terminal groups and two rising bands at 1275 and 1385 cm^{-1} from the Fermi's dyad of CO_2.

photodamage, (only) when it appears in combination with the 1275 cm^{-1} feature. Otherwise it can refer to the demethylation of Met residues (see below).

3.3.1.3 Methionine residues

The -C-S-CH_3 group of methionine is expected to be a high sensitive photodamage target according to previous remarks.[163,164,225] In the low-frequency region, three bands have been assigned to methionine-related photodamage events: two fading-out features at 665 and 724 cm^{-1} respectively, and a new rising band at 601 cm^{-1} (Figure 12). According to Culka et al.[226] the 665 and 724 cm^{-1} bands have been assigned to –C-S- stretching modes of Met. The slow reduction of these bands suggests the rupture of CG-SD and SD-CE bond within the Met side chains, as observed from electron densities (see below, Figure 21). The 601 cm^{-1} arising band over 17 MGy has been assigned to an out-of-plane deformation of •CH_3 radicals, according to literature.[227] In the medium-frequency region, Raman spectra show a clearly arising band at 1385 cm^{-1}

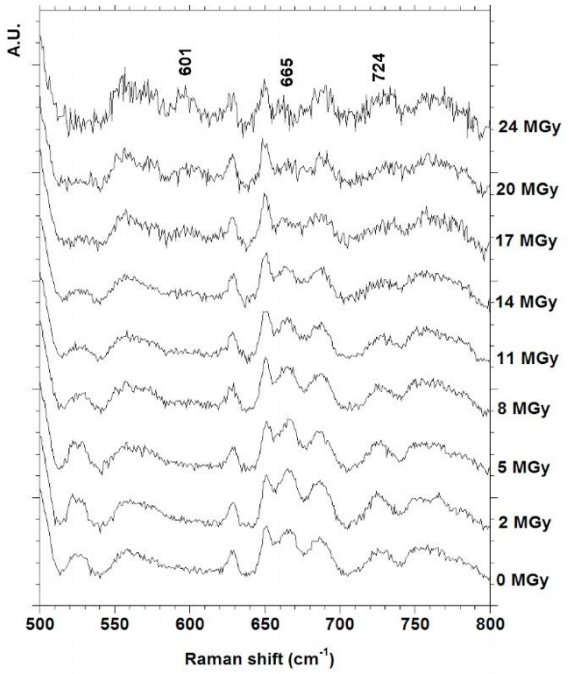

Figure 12 - Low frequency non-resonant Raman spectra showing a new rising band at 601 cm^{-1} assigned to •CH_3 radicals formation and two fading-out bands at 665 and 724 cm^{-1} diagnostic for –C-S- stretching modes of methionines.

which has been assigned to in-plane modes of $\bullet CH_3$ radicals.[227] The appearance of the two features at 601 and 1385 cm^{-1} can be assumed as markers for photodamage affecting methionine.

3.3.2 X-RAY CRYSTALLOGRAPHY

The eight crystal structures have the same overall secondary structure but a high number of tertiary structure modifications are clearly apparent. To follow, this work addresses for both the global and specific damage events by analysing electron-density maps, global crystallographic parameter, atom occupancy factors and the recently defined $B_{effective}$ and B_{damage} towards the arising X-ray dose elsewhere defined (see 3.3.2 – page 48).[219]

3.3.2.1 GLOBAL INDICATORS

Traditional parameters used to describe radiation damage in a protein crystal are diffraction limit, unit cell volume, crystal mosaicity and I/σ(I) ratio. RNase A crystals had diffracted at quasi-atomic resolution even once exposed to 24 MGy, indicating this system to be assuredly "X-ray proof". However, analysis of the global parameters for successive data collections reported in Figures 13-15 clearly indicate a significant damage. In fact, an

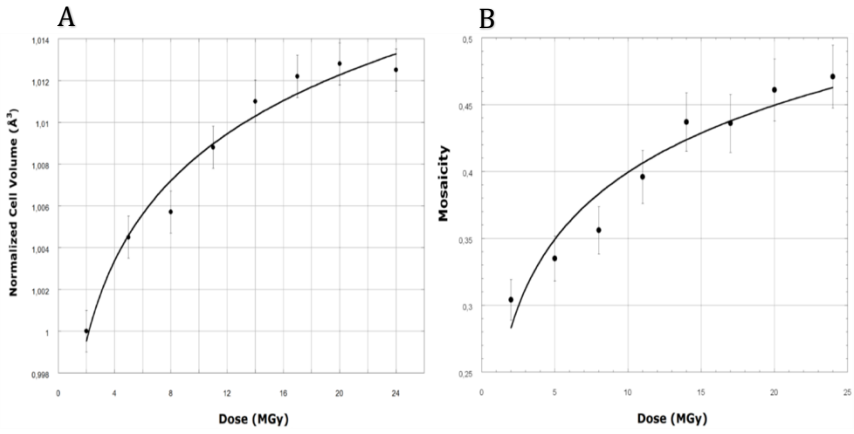

Figure 13 - A) Normalised cell volume (Å^3) and B) mosaicity towards arising absorbed dose.

increase in the unit cell volume normalised to the cell volume of the first data set (Figure 13A), an increase in the crystal mosaicity (Figure 13B) and R_{merge} Figure 14 and a decrease in I/σ(I) (Figure 15) indisputably indicate the photodamage occurrence.

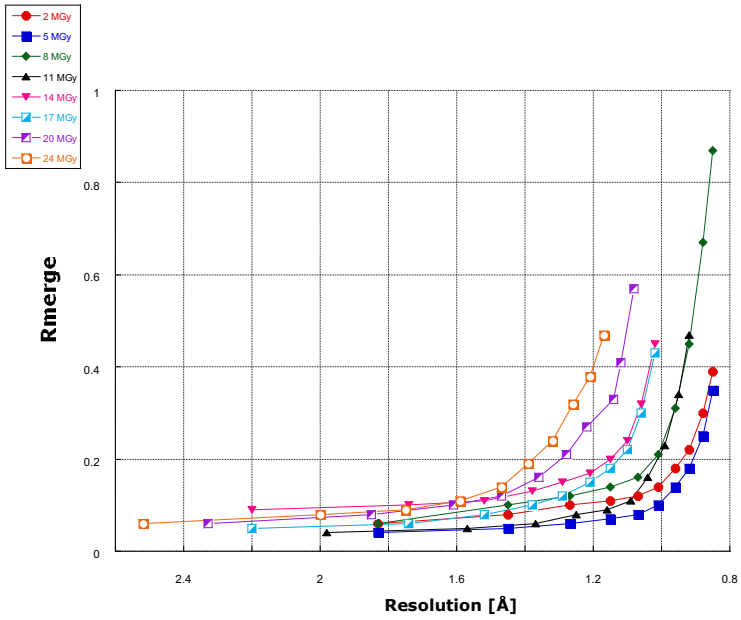

Figure 14 - Rmerge trends as function of arising dose for all of the eight data collections.

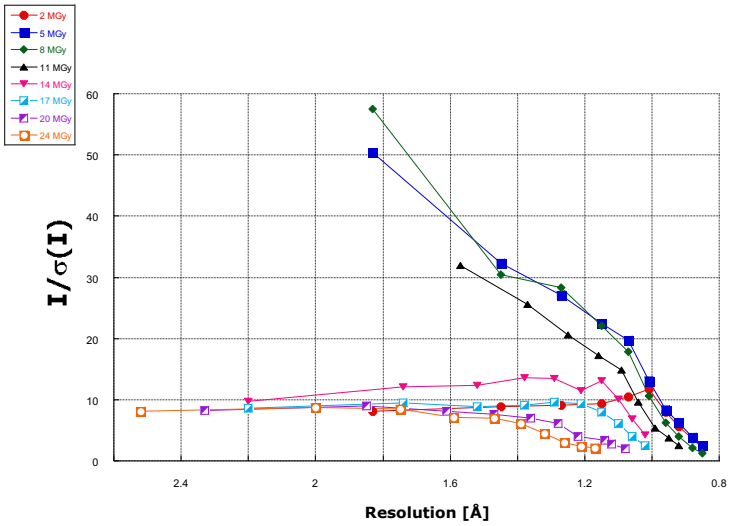

Figure 15 - Signal to noise ratio as a function of resolution (Å) for each dataset.

3.3.2.2 Specific damage

The parameters that were used to identify and quantify specific radiation damage are numerous. B-factors and relative isotropic B-factors can be certainly used to follow the progression of damage of groups of atoms within a protein structure, but they cannot be used to compare results obtained using different proteins. Recently, novel general parameters have been proposed: B_{damage}, which is defined as the B-factor of an atom *x*, normalized to the average value obtained for all atoms in a packing density environment similar to that of the atom *x,* and $B_{effective}$ that Garman and co-workers calculate using non-H atoms and isotropic B-factors.[219] Taking advantage from our well-refined atomic resolution structures, the more informative anisotropic B-factor have been used and their distribution and value as function of dose have been evaluated. As a comparison, isotropic B-factors have been also used not remarking decisive differences (data not shown).

As expected and in agreement with Raman data, analyses of Occupancy factors, B_{damage} and $B_{effective}$ had allowed to the detailed identification of specific damage occurring at Met, Asp and Glu side chains of RNase A, as well as on its C-terminal Val. More in detail, the ultrahigh resolution data allowed for a precise estimate of occupancy factors as function of dose whose trends clearly increase but for Met29, Figure 16. Coherently, $B_{effective}$ and B_{damage} parameters both increase as dose grows (Figures 17 and 18).

The $-CO_2^-$ group of all Asp and Glu residues in our structures are liable to specific radiation damage. Analysing the electron-density maps reported in Figures 19-22, decarboxylation is evidenced for both Asp and Glu residues. Interesting, electron density maps also reveal CO_2 loss from the C-terminal carboxylate Figure 22.

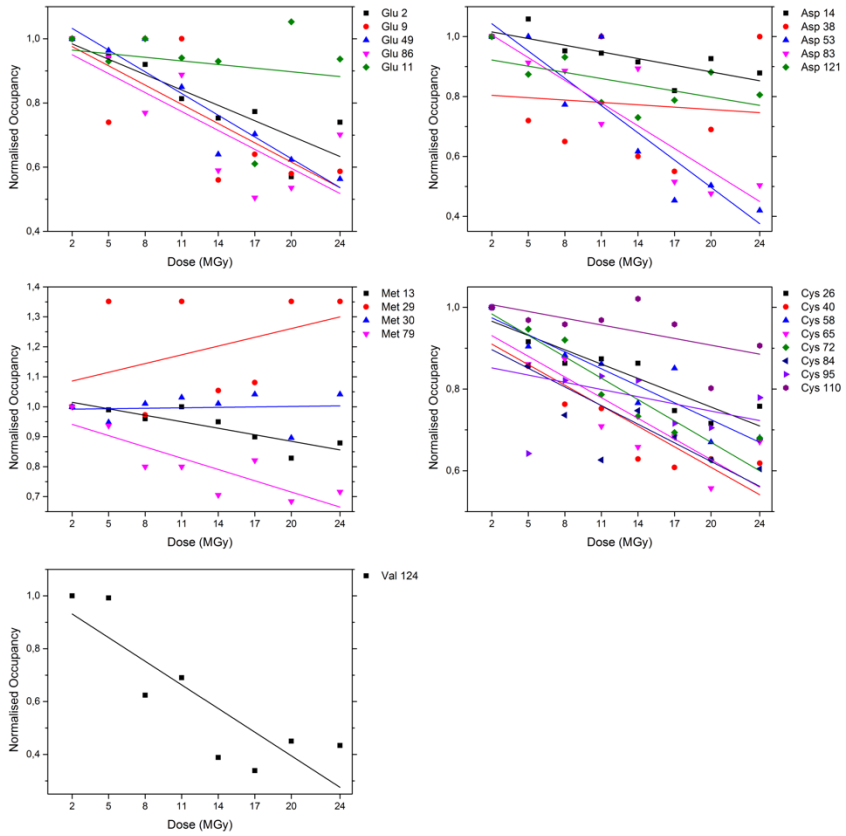

Figure 16 - Occupancy trends for damaged groups as a function of the arising dose (between 2 and 24 MGy), normalised using the lowest dose dataset (2 MGy) as reference. For Glu and Asp residues the mean occupancy value of their CO_2 terminal groups is reported. Met panel reports the occupancy trends for SD whereas SG is reported for Cys residues. Val124 trend refers to the C-terminal CO_2 tail mean occupancy.

Regarding the Met side chains, data reveal a clear reduction of electron density around CE atom of, up to the complete disappearance of density over the 11 MGy threshold (Figure 21) for Met29. At a deeper inspection, the Met side chain electron density maps also show a less pronounced yet decreasing trend for the CD atom compared to CE atom. This should indicate that radiation damage leads to both $\bullet CH_3$ and, less abundant, $\bullet SCH_3$ free radicals. Generally speaking, such highly reactive species are likely to diffuse throughout the crystal affecting other chemical groups, or

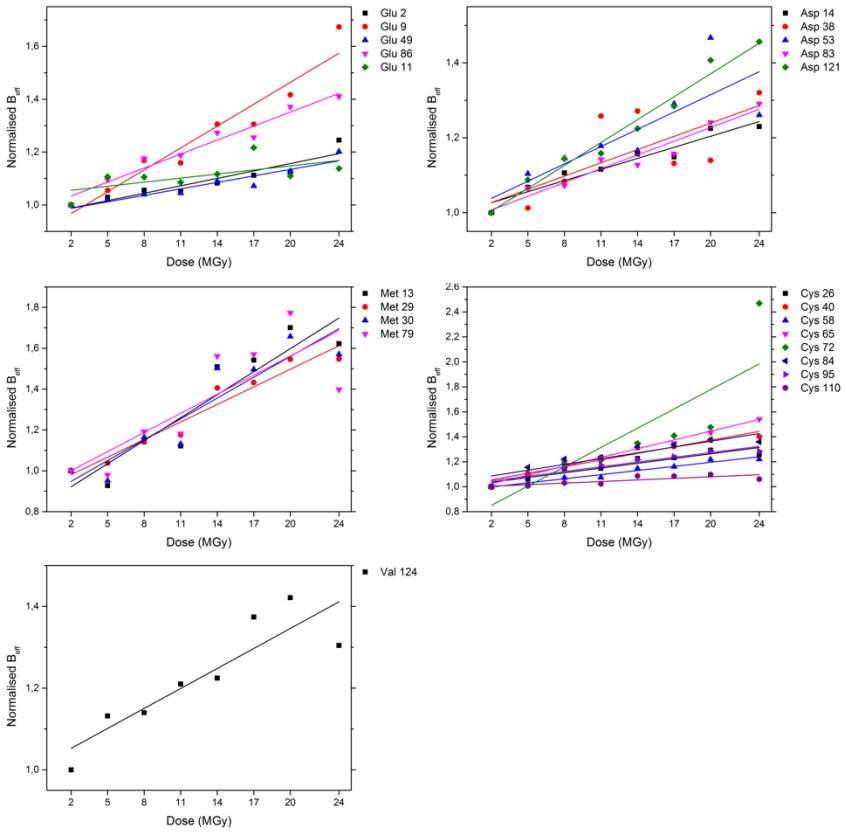

Figure 17 - $B_{effective}$ trends for damaged groups as a function of the arising dose (between 2 and 24 MGy), normalised towards the lowest dose dataset (2 MGy). B_{eff} are calculated as the ratio between the mean B value of the affected group and the average of all non-hydrogen and non-solvent atoms in the structure. For multi-conformation residues, only the highest occupancy conformation has been taken into account.

may rapidly back-react possibly explaining the persistent sulphur density.

As a final comment, the rupture of disulphide bridge has been commonly found in radiation damage studies and according to Raman spectra the disulphide bridges are the most sensitive groups of RNase A. Refinement of occupancy factors of the side chain atoms of Cys suggests that free Cys are present in a very small amount (<15%) in our structures. These data suggest that the mechanism of S-S bond repair proposed by Carpentier et al.[199] is probably operative also in this case.

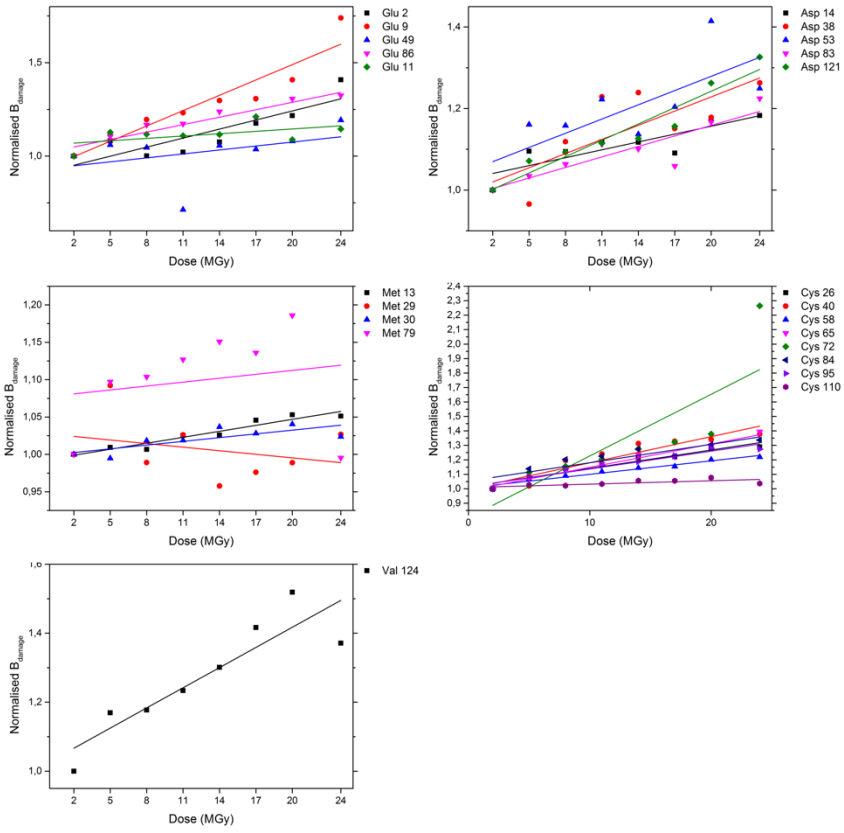

Figure 18 - B_{damage} trends for damaged groups as a function of the arising dose (between 2 and 24 MGy), nomalised towards the lowest dose dataset (2 MGy). B_{dam} are calculated as the ratio between the mean B value of the affected group and the average of all non-hydrogen atoms within a radius of 6 Å. B-values have been refined anisotropically by fixing to 1.00 the occupancy of the highest occupancy alternate conformation where present.

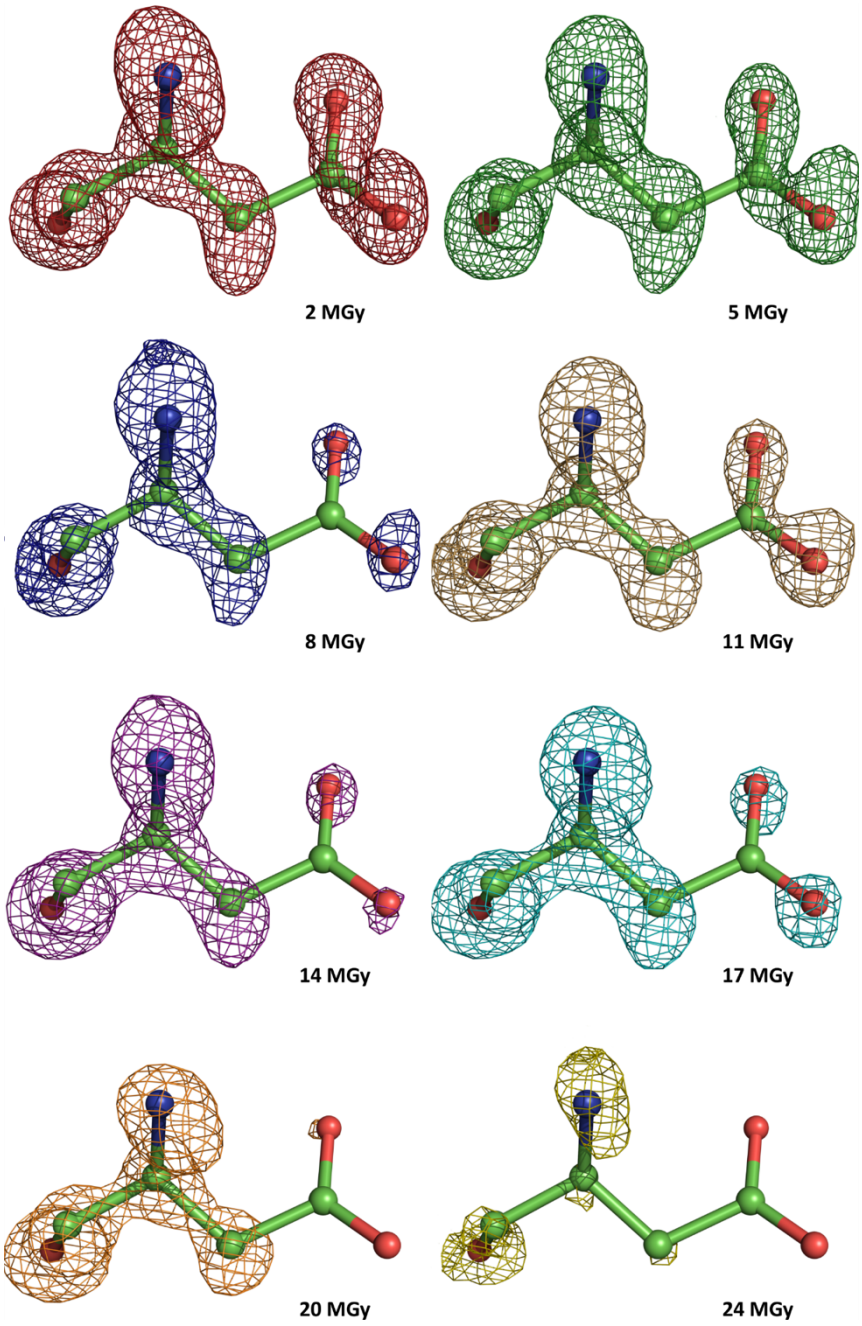

Figure 19 - Specific structural damage suffered by Asp38 side chain within a cryo-cooled crystal of RNase A during sequential dataset collections at the SpectroLab PX12 beamline - SLS. For a meaningful comparison between maps computed from different datasets, each map has been normalised using the 2 MGy Cα density as reference, that is electron density maps for each analysed residue have been scaled at the same electrons per $Å^3$ level of as the α-carbon of the corresponding 2 MGy map residue.

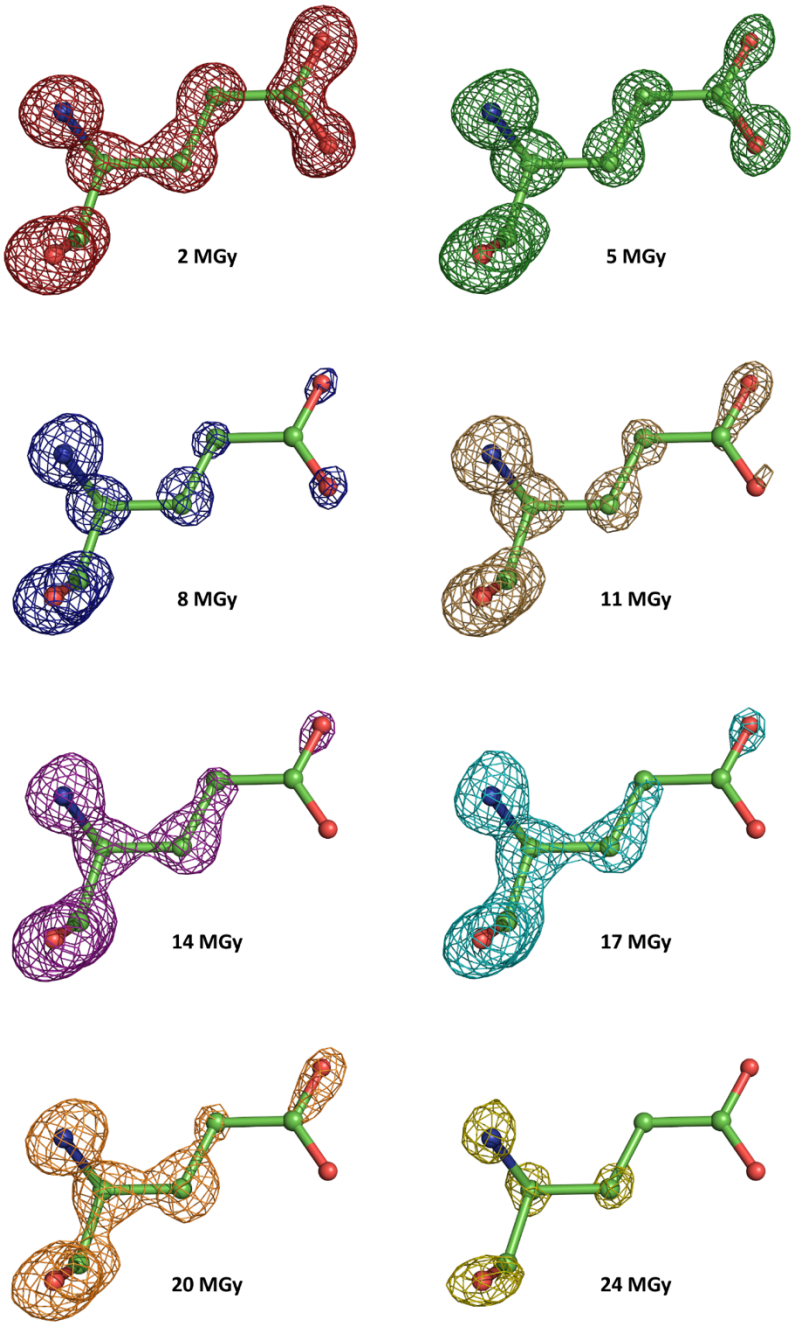

Figure 20 - Specific structural damage suffered by Glu111 side chain within a cryo-cooled crystal of RNase A during sequential dataset collections at the SpectroLab PX12 beamline - SLS. For a meaningful comparison between maps computed from different datasets, each map has been normalised using the 2 MGy Cα density as reference, that is electron density maps for each analysed residue have been scaled at the same electrons per $Å^3$ level of as the α-carbon of the corresponding 2 MGy map residue.

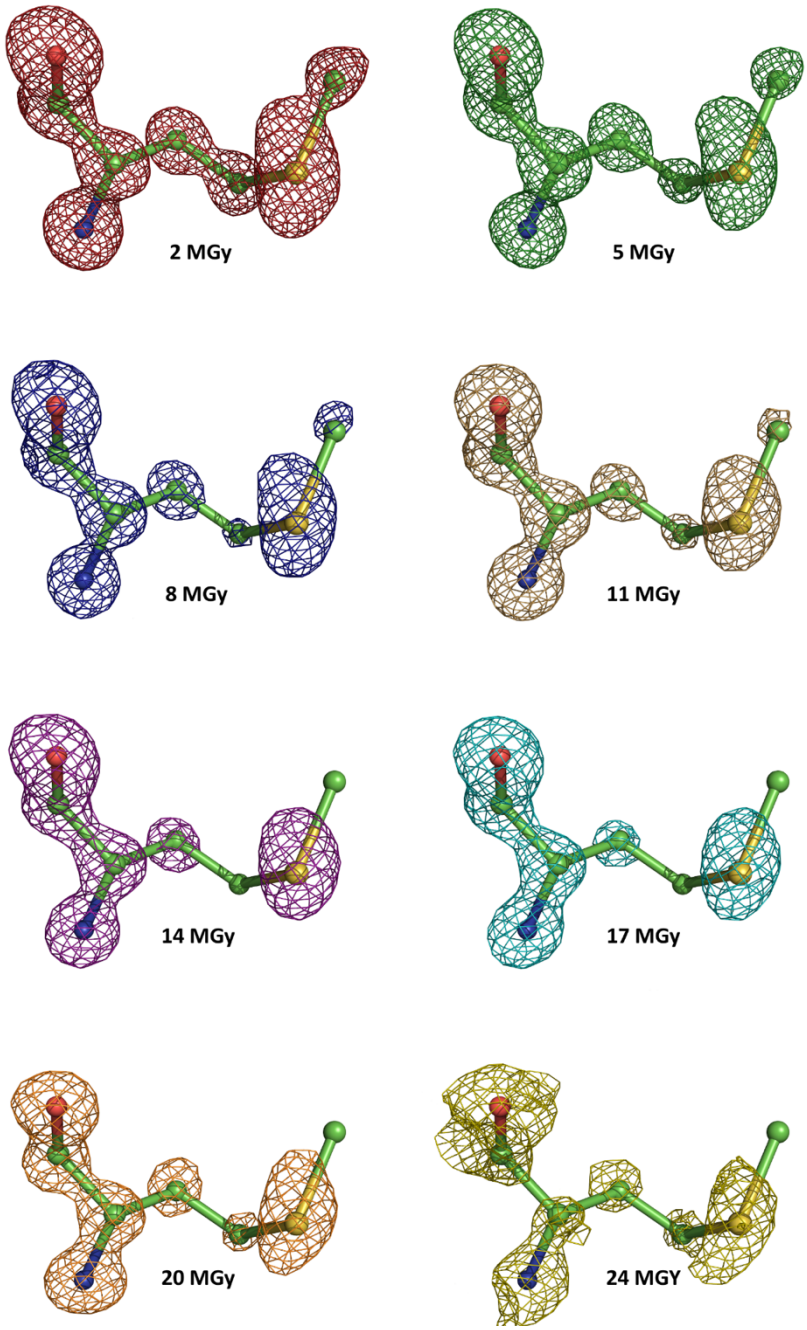

Figure 21 - Specific structural damage suffered by Met29 side chain within a cryo-cooled crystal of RNase A during sequential dataset collections at the SpectroLab PX12 beamline - SLS. For a meaningful comparison between maps computed from different datasets, each map has been normalised using the 2 MGy Cα density as reference, that is electron density maps for each analysed residue have been scaled at the same electrons per $Å^3$ level of as the α-carbon of the corresponding 2 MGy map residue.

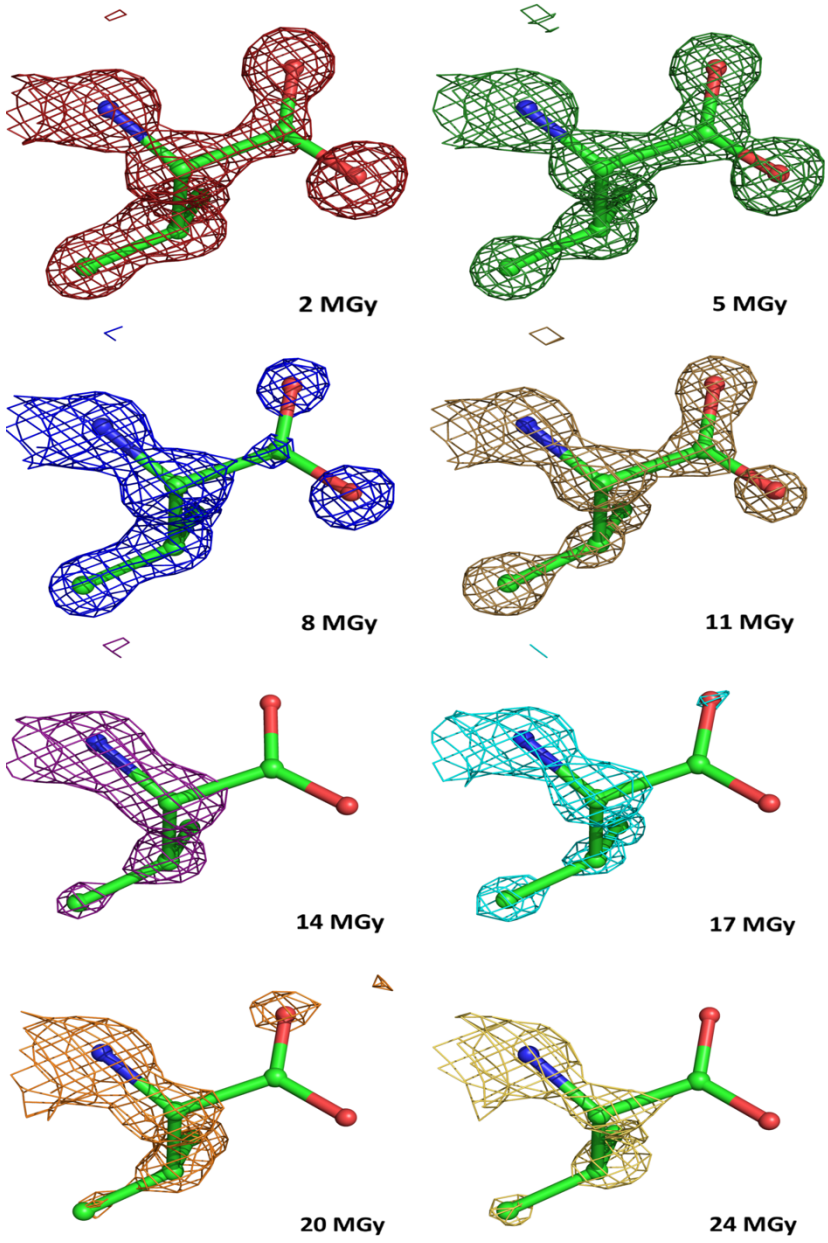

Figure 22 - Specific structural damage suffered by the C-terminal of Val124 carboxylate within a cryo-cooled crystal of RNase A during sequential dataset collections at the SpectroLab PX12 beamline - SLS. For a meaningful comparison between maps computed from different datasets, each map has been normalised using the 2 MGy Cα density as reference, that is electron density maps for each analysed residue have been scaled at the same electrons per $Å^3$ level of as the α-carbon of the corresponding 2 MGy map residue.

3.4 Conclusions

This study is among the trailblazing examples of Raman-assisted crystallography study for the evaluation of radiation damage in proteins and surely the very first providing:

I. Raman markers for the Asp/Glu *decarboxylation* and C-S *breakages* in Met residues.
II. Combines Raman microscopy with *ultrahigh resolution* data.

The aggregate of these findings points out the strong agreement with crystallographic data as appreciable from the analysis of global and specific damage indicators, including the decarboxylation of Asp and Glu side chains, decarboxylation of the C-terminal tail, breakage of S-C and S-S bonds (that are likely re-formed in most cases). Ultimately, this combined crystallographic and spectroscopic method has provided an effective experimental protocol for the in-situ detection of the ongoing radiation damage in cryo-cooled protein crystals via Raman microscopy.

It could trace the path for better and proper planning of X-ray data collections, that is, minimizing the adsorbed dose while maximizing the information that can be obtained from macromolecular crystals acquiring the highest possible resolution data compliant with the absence of artefacts.

Mindful of these findings, particularly during synchrotron data collections, attention should be paid to:

I. The 500-550 cm^{-1} region, possibly informative about S-S rupture.
II. Two fading-out bands, at 601 and 1385 cm^{-1}, and two arising signals, at 665 and 724 cm^{-1}, concerning Met.

III. The Fermi dyad bands at 1275 and 1385 cm^{-1} and the 1410 cm^{-1} growing feature, diagnostic for Asp and Glu and C-terminal decarboxylation events.

It is also possible to provide quantitative information on the dose needed to produce the observed effects, that is pointing out the residue-specific susceptibility to X-ray radiation. As widely expected, disulphide bridges are the foremost victim (at about 2 MGy). The Glu decarboxylation comes next at about 5 MGy closely followed by Asp at roughly 7 MGy. The rupture of C-S bonds in Met side chains comes at approximately at 13 MGy at last.[159,160,193]

These Raman-assisted ultrahigh resolution data could be useful for future studies and for a better understanding of how to optimize the dose lifetime of macromolecular crystals so that solid guidance can be provided to crystallographers. They also demonstrate the capabilities of ultrahigh-resolution crystallography teamed with Raman microspectroscopy to reveal important details of the radiation damage mechanisms, such as the formation of methyl radicals and C-terminal region decarboxylation. Indeed, the relevant Raman assignment of free CO_2 and free CH_3 radicals represent a few and far between case of crystallography-assisted Raman spectroscopy. Definitively, this Raman-assisted crystallography protocol can provide a standard microspectroscopic procedure for evaluating the X-ray induced photodamage in protein crystals, by performing Raman spectrum prior and after X-ray exposure particularly during synchrotron crystallographic studies.

4

All that glitters ain't gold

"*All that glisters is not gold-*
Often have you heard that told.
Many a man his life hath sold
But my outside to behold.
Gilded tombs do worms enfold.
Had you been as wise as bold,
Young in limbs, in judgment old,
Your answer had not been inscrolled
Fare you well. Your suit is cold-
Cold, indeed, and labor lost.

- The Merchant of Venice- "

This section confutes previously reported structural crystallographic evidences concerning the co-crystallization of gold nanoparticles within protein crystals. A first unsuccessful Raman investigation prompted a deeper reanalysis structural data deposited in the Protein Data Bank and crystallographic evidences for a misinterpretation are reported.

4.1 Introduction

The high ordered structure of protein single crystals has drawn increasing attention in the study of protein-based templates for the fine tuning of nanomaterials. Most of the early efforts have been, and continue to be, spent for the study of in-solution protein system that modulate growth and shape, thus the properties, of nanomaterials, particularly nanoparticles.[228,229] As previously mentioned (see section 1.6 - page 12), gold nanoparticles (AuNPs) are surely the most studied and probably the utmost appealing nanoscale system. The crystalline arrangement of proteins grants sufficiently broad intra-crystal channels to settle nanoparticles and substantially slows down their very fast formation kinetics allowing for a finer control of AuNPs in size.

These captivating hybrid systems are attracting increasing interest in terms of hybrid nanocatalysts, meant as systems taking advantage from catalytic properties either from the crystalline enzyme and its nanoparticle counterpart.

Early works had been conducted mostly by using cross-linked proteins but crosslinking spoils the protein tertiary structure likely hampering or at least modifying its catalytic behaviour.[230]

A deeper comprehension of these systems goes through a better understanding of the underlying structural bases. Wei and co-authors[121] firstly provided a most interesting insight into the co-crystallization process between native lysozyme single crystals and in-situ grown gold nanoparticles, by using the Au(I) precursor $ClAuS(CH_2CH_2OH)_2$. This method sensibly slows down the growth of nanoparticles giving the authors a unique chance to characterise the progression of the reaction in a reasonable time scale, study the distribution of gold nanoparticles within the crystal by using transmission electron microscopy (TEM) and electron tomography

(ET). To this point, authors had been able to follow the growth of AuNPs within the crystal by following the colour shift of this latter from colourless to red, a transition due to the surface plasmon resonance (SPR) band of AuNPs.[98] TEM and ET strongly supported this record providing further details concerning the time-dependent AuNPs growth kinetic within the crystal.

Remarkably, the AuNPs-holding lysozyme crystals did not lose their X-ray diffracting power confirming that no major rearrangements of the protein structure had occurred, by contrast with the previous reports from cross-linked protein crystals. Authors indeed adopted X-ray crystallography to further shed light on the mechanism underlying the AuNPs formation within the crystal from the Au(I) precursor and on the structural aspects of the possible interactions between AuNPs and the three-dimensional crystalline protein.

4.2 Results

Basing on their X-ray data and successive growth stages (PDB accession codes 3P4Z, 3P64, 3P65, 3P66, 3P68), the authors advanced a structural-based interpretation for the AuNPs formation within the crystal.

In the attempt to reproduce the procedure proposed by Wei et al.,[121] we have been able to obtain very well diffracting crystal of lysozyme in the presence of the $ClAuS(CH_2CH_2OH)_2$ precursor.

Anyhow, the analysis of the X-ray data collected from these crystals gave no any evidence for the presence of Au atoms within the structures.

This finding prompted us to consider and analyse the experimental data and refined models deposited by Wei et al. in the Protein Data Bank (codes 3P4Z, 3P64, 3P65, 3P66, 3P68). These structures account for nine different gold atoms (four isolated gold atoms and a 5-atom cluster). Three out of these five structures show a single gold ion bound to His15 and to a monoatomic ligand (Figure 23), which Wei et al. reasonably modelled as a chloride ion, considering that lysozyme crystals were grown in high NaCl concentrations. Finally, five more gold ions are clustered together in the last two

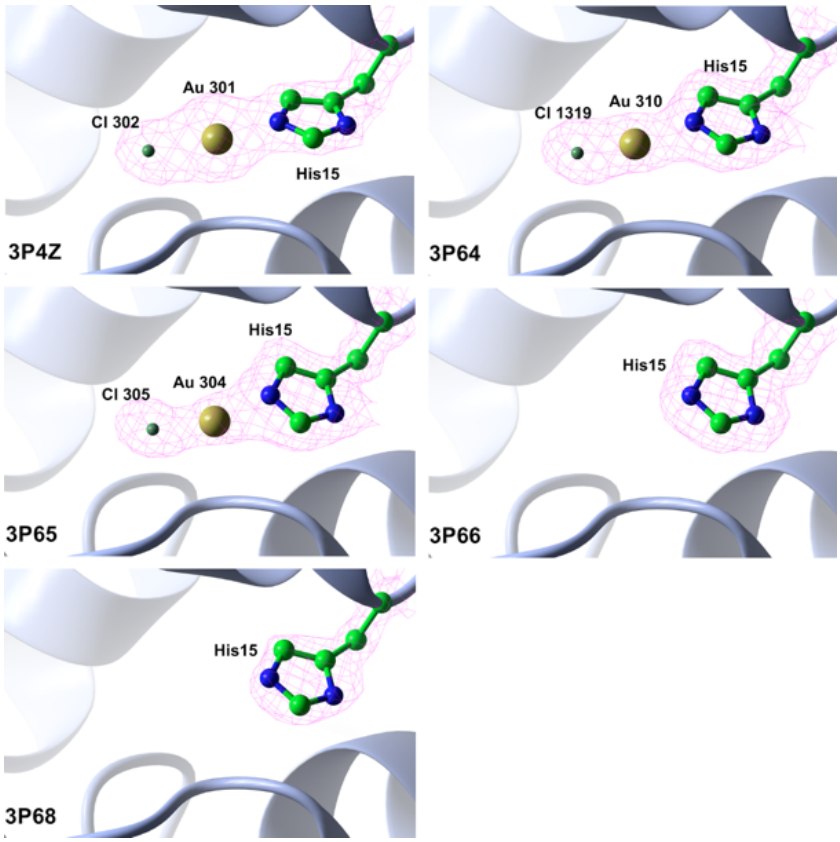

Figure 23 - 2Fo-Fc electron density maps (0.5 $e^-/Å^3$) of the Au^+ binding site close to His15 calculated by using data deposited in PDB by Wei et al. Au^+ ion is coloured in yellow, whereas the Cl^- ion is reported in green. The side chain of His15 is also shown.

deposited crystal structures. For eight out of the nine gold atoms found in the structures deposited by Wei et al., it has been possible to demonstrate that the authors' interpretation inaccuracy.

Surveying our previous and PDB deposited data either, almost all gold atoms have been placed by Wei et al. where Cl^- or Na^+ ions are usually found in isomorphous crystals of lysozyme grown using condition similar to those adopted in the case: NaCl as a precipitant and sodium acetate as buffer solution.

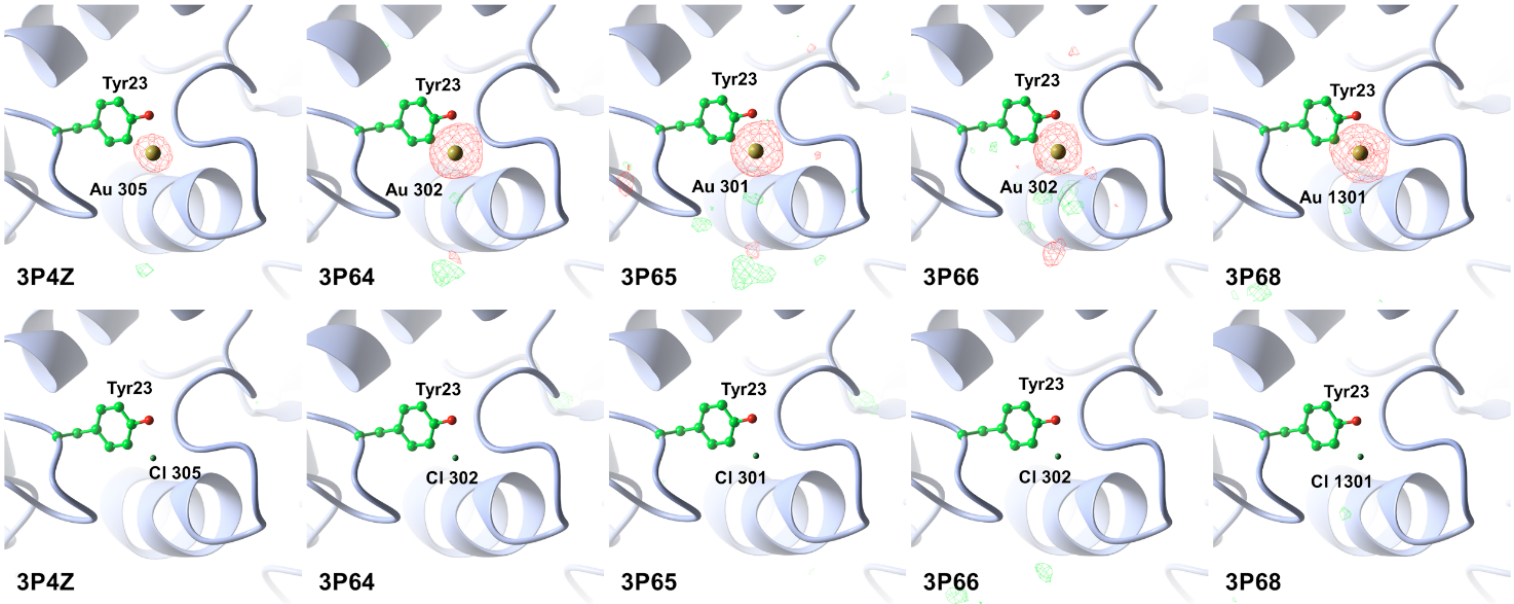

Figure 24 - Electron density difference maps (0.4 $e^-/Å^3$) of the "gold atom binding site" close to Tyr23. Negative peaks are coloured in red, whereas positive peaks are in green. Maps in the upper row are calculated by using the coordinates deposited in PDB, whereas those reported in the lower row are obtained using coordinates that include the substitution of the gold ion with a chloride ion. In addition, Au ions are widely known to form their most stable complexes with "*soft*" donor atoms such as P, S or N; by contrast, in these crystal structures the Au ions have been invariably placed in atypical coordination, e.g. close to Tyr23, Ser24 or Thr43.

The analysis of electron density maps has unveiled large negative peaks at the position of Au atoms (Figures 23-27), representative for an over-interpretation of the local electron density.

By performing independent refinements using structure factor deposited by Wei et al., these negative peaks had disappeared once gold atoms had been replaced by Cl^-, Na^+ ions or even water molecules.

The simple replacements had prompted significant reduction of both R-factor and R-free (that is, a better agreement between structural models and experimental crystallographic data) in all the modified five structures (Table 3).

Definitively, three out of five crystal structures solved by Wei et al. are much more likely to be wild-type lysozyme models, with only one Au^+ ion bound to His15, rather than crystallographic structures for the protein-nanoparticles adduct. The last two crystal structures are gold-free.

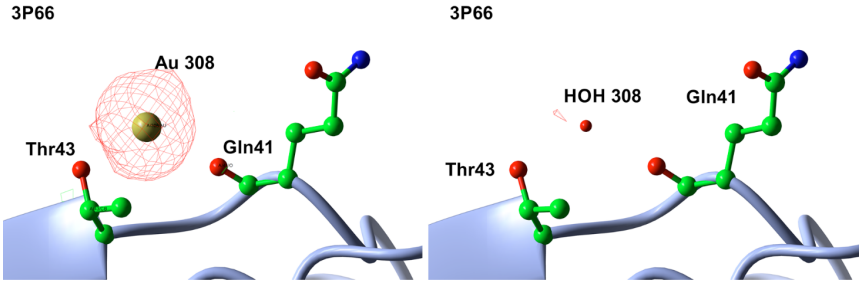

Figure 25 - Electron density difference maps (0.4 $e^-/Å^3$) of the "gold atom binding site", close to Thr43. This site has been found exclusively in the structure deposited in the PDB with code 3P66. Negative peaks are coloured in red, whereas positive peaks are in green. Maps in the left panel are calculated by using the coordinates deposited in PDB, whereas those in the right one are obtained using coordinates that include the substitution of the gold ion with a water molecule.

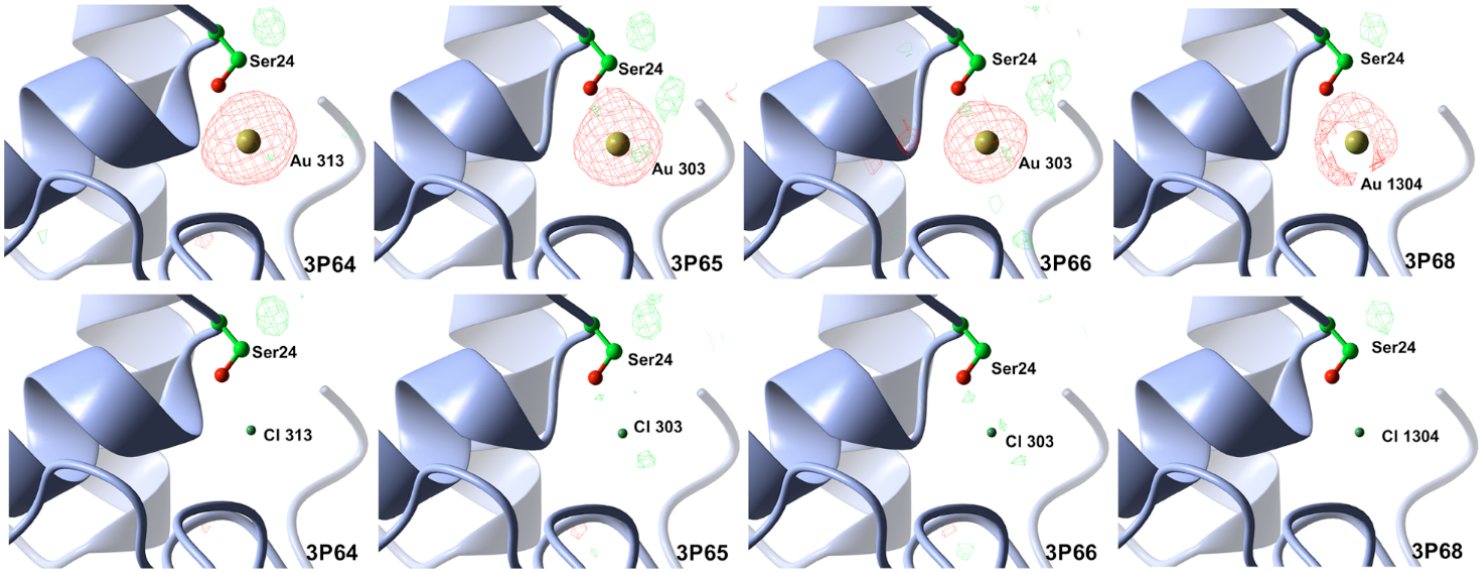

Figure 26 - Electron density difference maps (0.4 $e^-/Å^3$) of the "gold atom binding site" close to Ser24. This site has not been observed in the structure deposited in the PDB with code 3P4Z. Negative peaks are coloured in red, whereas positive peaks are in green. Maps in the upper row are calculated by using the coordinates deposited in PDB, whereas those reported in the lower row are obtained using coordinates that include the substitution of the gold ion with a chloride ion.

The aggregate of these findings weakens, but do not invalidate the hypothesis suggested by Wei et al.[121] of a protein-mediated metal ion transfer preceding the nanoparticle formation, a result that has recently been supported by Baksi et al.[231] However, the structural analysis proposed by Wei et al.[121] cannot stand to unveil protein-gold nanoparticle interactions because no gold atom is unambiguously found in the lysozyme structures reported, apart from one ion bound to His15 in the first three structures. This means that structural data on biomolecule-directed gold clusters is still lacking and the molecular bases of protein-gold nanoparticle recognition requires further investigation.

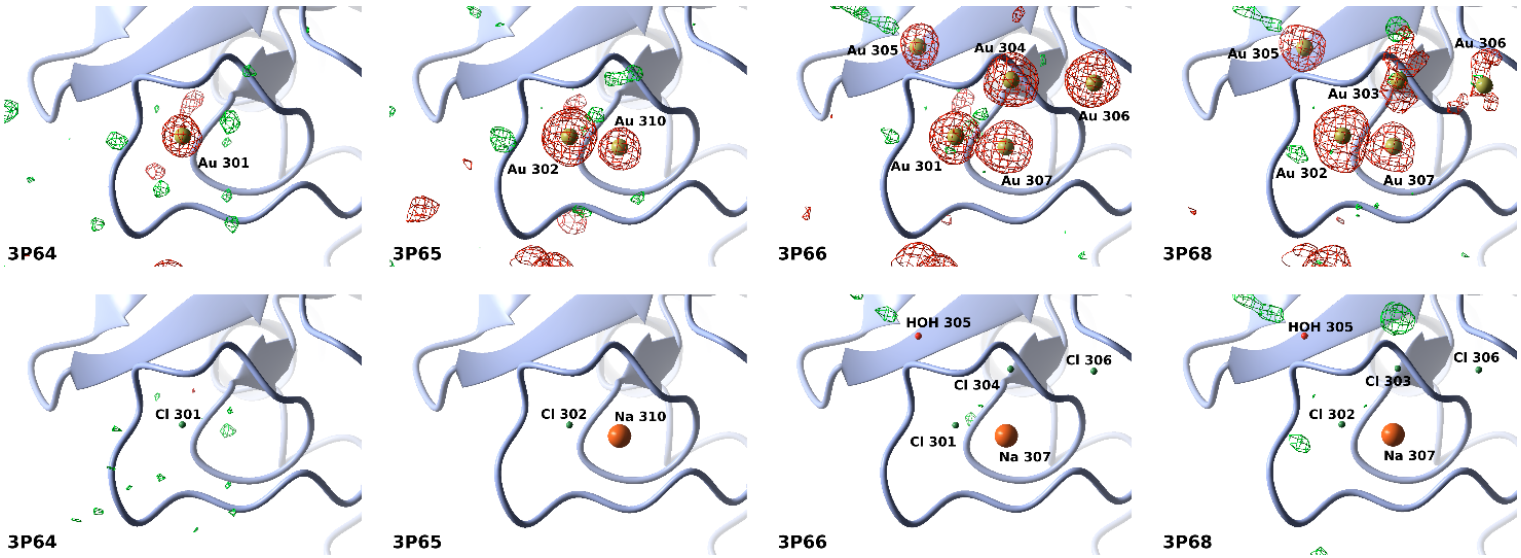

Figure 27 - Electron density difference maps (0.4 $e^-/Å^3$) for the proposed "gold cluster". Negative peaks are coloured in red, whereas positive peaks are in green. Maps in the upper row are calculated by using the coordinates deposited in PDB, whereas those reported in the lower row are obtained using coordinates that include the substitutions of the gold ions with a water molecule, one sodium ion and three chloride ions.

Table 3 - R-factor and R-free values before and after substitution of proposed gold atoms, except the Au^{+} close to His15.

PDB entry	Rvalue before	Rvalue after	Rfree before	Rfree after	Substitutions	
					before	after
3P4Z	0.197	0.193	0.257	0.256	Au 301	Cl 301
3P64	0.214	0.189	0.243	0.218	Au 301 Au 302 Au 313	Cl 301 Cl 302 Cl 313
3P65	0.218	0.182	0.244	0.204	Au 301 Au 302 Au 303 Au 310	Cl 301 Cl 302 Cl 303 Na 310
3P66	0.241	0.172	0.271	0.211	Au 301 Au 302 Au 303 Au 304 Au 305 Au 306 Au 307 Au 308	Cl 301 Cl 302 Cl 303 Cl 304 HOH 305 Cl 306 Na 307 HOH 308
3P68	0.225	0.192	0.253	0.231	Au 301 Au 302 Au 303 Au 304 Au 305 Au 306 Au 307	Cl 301 Cl 302 Cl 303 Cl 304 HOH 305 Cl 306 Na 307

5

Zinc-binding hCA II inhibitor

5.1 INTRODUCTION

Carbonic anhydrases (CAs) are ubiquitous metallo-enzymes that catalyse the reversible CO_2 hydration reaction.[232,233] They are widespread in all the kingdoms of life and encoded by six evolutionarily unrelated gene families, namely α-, β-, γ-, δ-, ζ- and η-CAs.[232,234] Human (h)CAs belong to the α-class and exist in 15 isoforms differing each other by molecular features, oligomeric arrangement, cellular localization, tissue distribution, and kinetic properties.[232] Bearing in mind the critical role of the reaction catalysed by CAs, these enzymes are involved in a variety of physiological/pathological processes, consequently becoming high-value targets for pharmaceutical research, and a number of studies have been reported on CA inhibitors (CAIs) in recent years.[232,235-238] In particular, the elucidation of their mechanism of action went through crystallographic analyses of several enzyme-inhibitor adducts allowing to determine the molecular bases of enzyme-inhibitor interactions.[232] The most effective CAIs are sulphonamide/sulfamate-based molecules interacting with the enzyme active site by coordinating the zinc ion and displacing a water molecule/hydroxide ion;[232] however, these molecules are generally poorly selective towards different CA isoforms. To this end, new zinc binding groups are continuously tested to advance in the identification of isoform-selective CAIs.[239,240]

Herein, RAC has been deployed to support and disambiguate structural aspects for the inhibition mechanism of a newly synthesised CAI, hydroxylamine-O-sulphonamide **1** (Figure 28), a molecule containing two zinc binding groups, namely the sulphonamide and hydroxylamine. This molecule has been

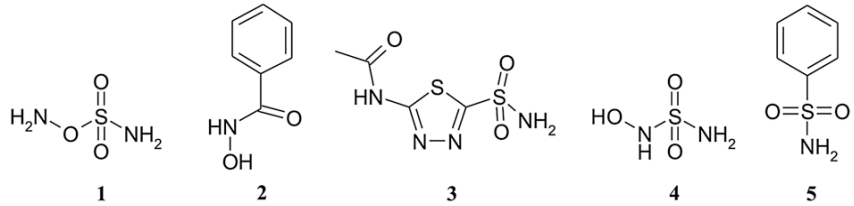

Figure 28 - Chemical structures of compounds 1–5.

synthesised by co-authors at the CNR Institute of Biostructures and Biomages – Naples, who also performed the inhibition profile study towards the different hCAs isoforms.

The opening hypothesis was that two functional groups could give an ambidentate character to this derivative. Previous data show compound **1** to possesses interesting inhibition profiles and binding modes towards hCA isoforms, as it can bind the Zn ion of CA active site with both Zn-binding groups, suggesting that the derivatisation of the sulphonamide nitrogen and of the hydroxylamine moiety can be used to obtain new classes of inhibitors.

5.2 Experimental and Results

The inhibition profile of **1** against all catalytically active hCA isoforms was investigated by co-authors showing that this molecule has a rather variable behaviour against different isoforms. Indeed, **1** behaves as a potent inhibitor towards hCA II and hCA VA, (K_Is of 50.9-55.5 nM), as a medium-strength CAI towards several other isoforms (e.g. IV, IX and XII - K_Is of 133.6–161.9 nM), whereas hCA III, VII and XIII are inhibited with constants in the 326–608 nM range. Three isoforms (hCA I, VI and XIV) are not inhibited significantly by compound **1**. This unique profile is of interest for developing new inhibitors.

5.2.1 X-ray crystallography

To elucidate the binding mode of **1** to the CA active site, the structure of the adduct that this molecule forms with the best characterized hCA isoform, namely hCA II, has been solved (accession code 4YVY). The hCA II/**1** crystals have been obtained and the three-dimensional structure has been analysed through difference Fourier techniques by co-authors.

Inspection of the initially calculated electron density maps in the active site cavity has showed clear evidence for the binding of the inhibitor to the catalytic zinc ion. Anyhow, these maps have not allowed for unambiguously discriminating the inhibitor binding mode though being very well defined. Indeed, two different models fit in and compatible with the electron density maps: the first one - hereafter indicated as binding *mode A* - with the catalytic zinc ion coordinated by the sulphonamide nitrogen and the second one – binding *mode B* from now on - where the coordination was due to the hydroxylamine moiety in a side-on (η^2) fashion (Figure 29).[241]

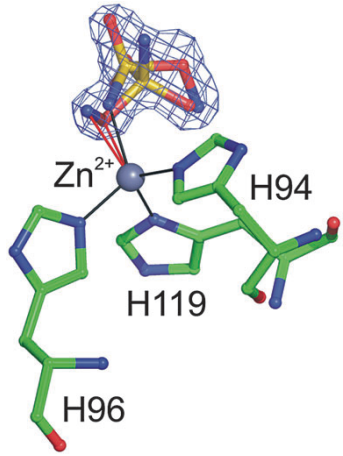

Figure 29 - Active site region in the hCA II/1 adduct, showing the sA-weighted |Fo–Fc| OMIT map (contoured at 3.0σ). The two possible coordination modes of inhibitor 1 are reported. The zinc ion coordination is drawn in black and red for binding modes A and B, respectively.

5.2.2 Raman microspectroscopy

To get preliminary information on the Zn^{2+} coordination in the hCA II/**1** complex, Raman microspectroscopy has therefore been performed on the hCA II single crystals with or without the inhibitor either (Figure 30).

All of the Raman data collections have been carried out using a Jasco NRS-3100 microscope and a 514 nm line from a Ar^{+} laser as light source. A 20x objective granted a focused spot size of approximately 2 μm while laser line rejection has been guaranteed by a holographic notch filter. The Raman backscattering has been collected at 180° by using a 0.1 mm slit and a 1200 grooves/mm grating, corresponding to an average spectral resolution of 7 cm^{-1}. The minimum exposure time of collected spectra has been 60 seconds by using a Peltier-cooled 1024x128 pixel Andor CCD photon detector. Wavelength calibration has been performed by using cyclohexane as a standard. Raman microspectroscopy measurements on hCA II crystals have been conducted keeping

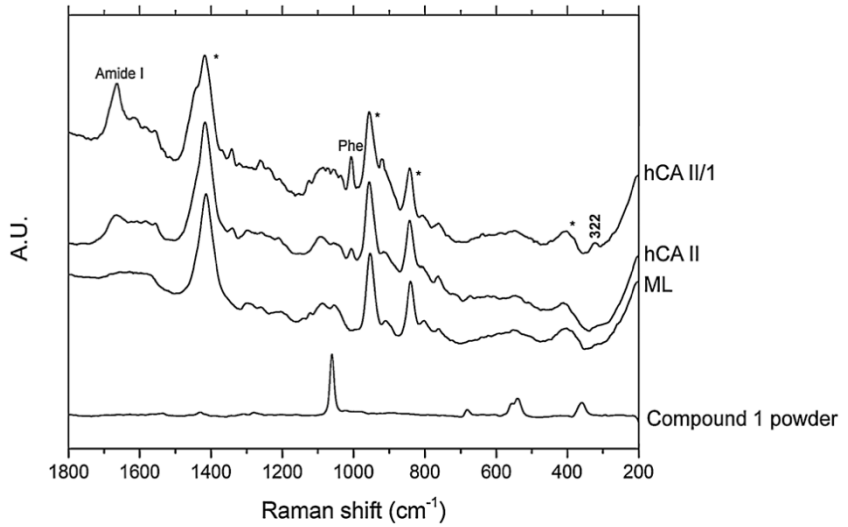

Figure 30 - Raman spectra of the hCA II native crystals, inhibitor 1 and hCA II/1 complex crystals. Mother liquor (ML) is also reported to detect signals from it (*).

crystals into a drop of mother liquor, using a common 24-well hanging drop crystallization plate.

Several Raman signals from hCA II have been clearly observed in the crystal (e.g. amide I band at around 1666 cm^{-1}, and Phe ring band at around 1007 cm^{-1}) besides strong signals from mother liquor. Upon inhibitor **1** addition, these signals are almost unaltered whereas a novel significant Raman band appeared at around 322 cm^{-1}. This band is absent in the spectra collected from the native crystals, the inhibitor powder and the mother liquor (Figure 30) and could confidently be assigned to vibrational modes related to the binding of the inhibitor to the enzyme, in particular, to stretching modes between Zn^{2+} and O and/or N atoms. Unluckily, no aid came from literature for unambiguous assignment. A crystallography-assisted Raman analysis has been therefore adopted and further Raman experiments have been performed on hCA II native crystals soaked with two different inhibitors, namely compounds **2** and **3** in (Figure 28), whose Zn^{2+} ion coordination had been defined clearly and unambiguously by previous crystallographic investigations.[242,243]

Explicitly, inhibitor **2** coordinates the catalytic zinc ion through O atoms,[242] whereas compound **3**, the widely known CA inhibitor acetazolamide (**AZM**), binds via the sulphonamide nitrogen atom, the very same way described above for the binding mode A.[243]

Raman spectra of the hCA II/**2** adduct did not show any band at around 322 cm^{-1} whereas those on the hCA II/**3** complex exhibited

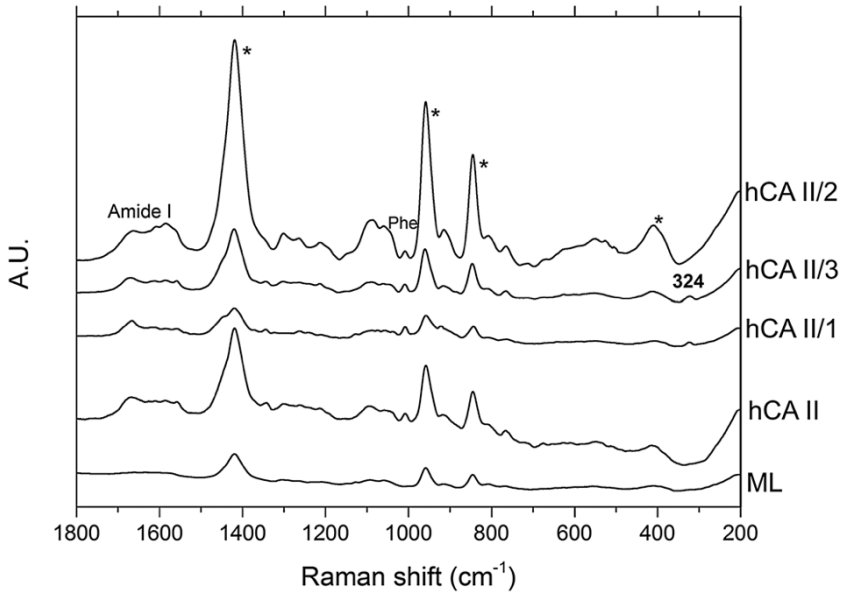

Figure 31 - Raman spectra comparison among wild type hCA II and three complexes with the corresponding compounds.

a clear Raman signal at around 324 cm^{-1}, very close to the one seen in the hCA II/**1** adduct (Figure 31).

Thus, these crystallography-assisted Raman data suggested that in analogy with the hCA II/**3** complex, at least partial Zn^{2+} ion coordination occurs via the sulphonamide nitrogen atom in the adduct under investigation, even though it has not been possible to utterly rule out alternative coordinations.

Regrettably, no Raman data were available for side-on Zn^{2+}-ligand coordination. To this end, some DFT[244,245] and Raman data gathered form other metals with nitrosyl or peroxo-species have been taken into account.[245,246] DFT calculations foreseen significant structural differences between end-on and side-on coordination,[245] while Raman data pointed out a noteworthy switch in the low frequency mode between end-on and side-on-metal–ligand coordination.[247] Raman spectra did not show any additional signal beyond the one at 322 cm^{-1} corresponding to the **AZM**-like coordination, prompting the hypothesis that the alternative side-on coordination

of the hydroxylamine moiety was not detectable by Raman microspectroscopy due to low Raman cross-section. At this point, the side-on frequency mode have been assumed not to fall below the end-on **AZM**-like Raman band (around 322 cm^{-1}), thus allowing for the quantitative analysis reported below. Indeed, considering the hCA II/**3** adduct binding to exclusively occur via N-coordination,[243] our Raman analysis also permits a putative quantitative evaluation for the **AZM**-like binding in the hCA II/**1** complex. More in detail, by assuming the Raman cross-section of the Zn^{2+}–N band at around 322 cm^{-1} to be the same for either the hCA II/**1** and hCA II/**3** complexes, and using the signal of the Phe band at 1007 cm^{-1} as an internal reference for spectra normalization, a fraction of 0.4±0.1 has been evaluated to be bound as AZM-like for compound **1**.

Altogether, Raman data hence suggest that 40% of the coordination of the catalytic Zn^{2+} ion in the hCA II/**1** complex occurs through the sulphonamide nitrogen (*binding conformation A*) and for the remaining 60% through binding coordination not identifiable from Raman experiments.

5.3 Discussion

Basing on these data, the two initially hypothesised alternative binding conformations have been modelled in the electron density maps (Figure 29). The atomic occupancy factors Q have thus been refined by fixing their respective B-factor to values comparable to those of the solvent within the active site. Interestingly and in good agreement with Raman spectroscopy data, the occupancy factors Q have been pinpointed at 0.33 and 0.34 for binding conformation A and B respectively. Since the aggregate of inhibitor binding conformations Q adds up to 0.67 and residual electron density yet was appreciable in the surrounding of the zinc ion, an alternative water molecule coordinated to the zinc ion at Q=0.33 has been added to fill-up the gap. The protein–inhibitor interactions for both binding modes A and B are shown in Figure 32.

Interestingly, though a number of studies suggest that sulphonamides generally coordinate to the catalytic zinc ion through a deprotonated nitrogen atom, the pKa values calculated by co-authors for the hydroxylamine and sulphonamide moieties

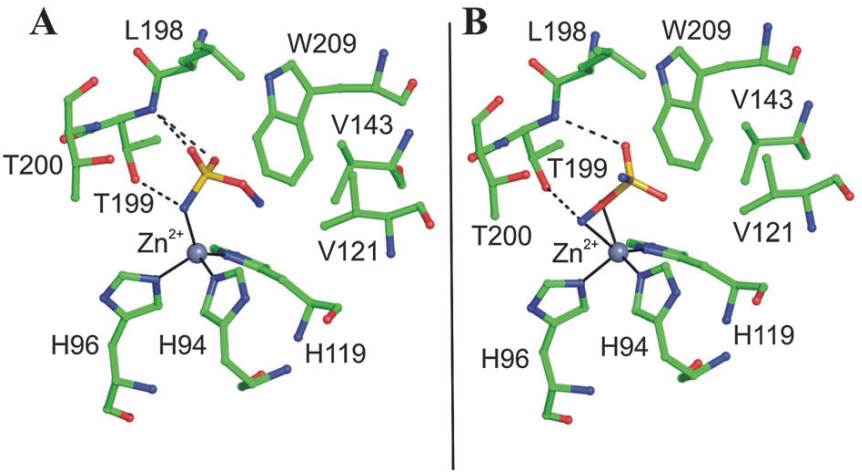

Figure 32 - Zn^{2+} coordination geometry in the hCA II/1 adduct for binding conformation A (A) and B (B). Hydrogen bonds and residues forming van der Waals interactions are also reported.

of compound **1** using the Marvin software[248] gave different indication. At the pH condition adopted for crystallization experiments, the inhibitor exists as a non-deprotonated form in both binding forms.

It is worth noting that compound **4**,[249] a strictly related isomer of compound **1** (Figure 28), adopted only one conformation within the hCA II active site, coordinating the zinc ion through the sulphonamide nitrogen atom, as observed in conformation A of the hCA II/**1** adduct.

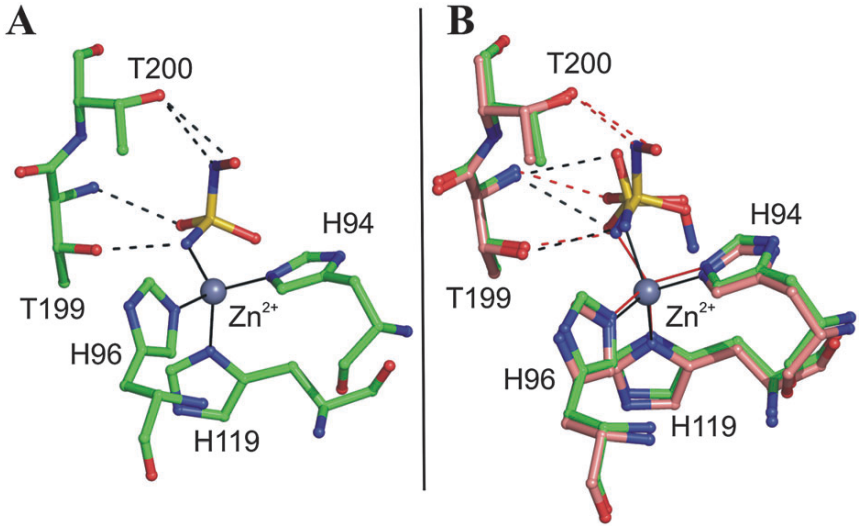

Figure 33 - (**A**) Zn^{2+} coordination geometry in the hCA II/4 adduct (PDB code 2O4Z). (**B**) Structural superposition of **1** in conformation A and **4** when bound to the hCA II active site. The active site residues of hCA II/**1** and hCA II/**4** adducts are coloured in pink and green, respectively. Inhibitor polar interactions are drawn in black for hCA II/1 and red for hCA II/4.

The inhibitor binding mode observed in hCA II/**1** has been compared to that of a classical benzene-sulphonamide, namely compound **5**[250] (Figure 33A and B). Interestingly, while the sulphonamide moiety of **1** in the binding conformation B is perfectly superimposable to the sulphonamide group of **5**, the same moiety in binding conformation A assumes a position completely different from that of benzene-sulphonamide **5**.

On the basis of these data, it is possible to hypothesise that derivatization of compound **1** on the hydroxylamine moiety, thus forcing the binding conformation A, could allow the inhibitor to interact with regions of the active site not yet explored using classical benzene-sulphonamides.

Altogether, these results strongly suggest that the hydroxylamine-O-sulphonamide inhibitor represents an interesting lead compound alternative to the classical sulphonamides for the development of more selective CAIs.

The last few years saw the discovery of an entire new range of CAIs possessing a variety of non-classical inhibition mechanisms.[232]

Indeed, for more than 60 years, since the report of sulphonamides as CAIs, the drug design landscape has been dominated by these compounds and their isosteres, the sulphamates and sulphamides.

They possess a rather simple inhibition mechanism, as they bind in deprotonated form to the metal ion from the active site, as the fourth ligand.[232] However, starting from 2008 completely new chemotypes were reported as CAIs: the coumarins,[251] the polyamines,[252] dithiocarbamates,[253] xanthates,[254] hydroxamates,[242] sulfocoumarins,[255] carboxylates, etc.[240,256] Many of them possess an inhibition mechanism strikingly different compared to the classical one. Some of these inhibitors anchor to the zinc-coordinated water molecule (polyamines, sulpho-coumarins, and some carboxylates),[252,255,256] others bind towards the exit of the active site cavity in the activator-binding site (coumarins and their derivatives),[251,257,258] whereas some carboxylates are even observed to be bound out-of-the active site.[240] The compound investigated here, hydroxylamine-O-sulphonamide 1, although possessing a simple chemical structure, is unique due to its versatility in inhibiting these enzymes, being the first example in which two alternative coordinations to the metal ion were evidenced. As aforementioned,

compound **1** is partially coordinated classically, as all sulphonamides/sulphamates, binding the Zn^{2+} ion through the sulphonamide nitrogen and partially through the hydroxylamine moiety in a side-on (η^2) fashion, which is a common inhibition pattern for this family of enzymes. The aggregate of these facets can definitely be exploited for drug design purposes as the chemical simplicity of compound **1** is amenable to elaboration through medicinal chemistry purposes.

Besides chemical implications and medicinal exploits, we herein shown an original crystallography-assisted Raman spectroscopy approach for investigating the binding mechanism of compound **1** to hCA II. This approach allowed to identify and disambiguate the hydroxylamine-O-sulphonamide binding modes to Zn^{2+} and proved to have a more general utility in the investigation of metal ion coordination when standalone X-ray crystallography or Raman microspectroscopy cannot provide unarguable response.

6

Iridium CO-releasing molecule

A combination of mass spectrometry, Raman microspectroscopy, circular dichroism and X-ray crystallography has been used to obtain detailed information on the reaction of an iridium-based CO-releasing molecule (Ir-CORM), Cs_2IrCl_5CO, with a model protein, bovine pancreatic ribonuclease. The results show that Ir-compound fragments bind to the N-terminal amine and close to histidine and methionine side chains, and the CO ligand is retained for a long time. The data provide helpful information for identifying protein targets for Ir-CORMs and for studying the mechanism that allows them to exhibit their interesting biological properties.

6.1 Introduction

The properties of some metal-containing compounds in the treatment of selected human diseases have been known since long but, after the cisplatin breakthrough and its derivatives in the treatment of tumours, the interest of the scientific community towards the synthesis and characterization of potential drugs based on metal compounds has sensibly grown and numerous complexes of diverse metals, including iridium, have been tested as pharmacological agents. Tough the mechanisms of action of these compounds have not yet been entirely deciphered, it is as clear as day that DNA is not the sole primary target, as for Pt based drugs.[4,91,259]

The study of the interaction of metal-based drugs with proteins is thus of crucial importance to unveil the mechanism of action of these important pharmacological agents and several reviews have been published in this field.[260-262]

Among the metal-based drugs, CO-releasing molecules (CORMs from now on)[46,263-266] based on complexes of Mn, Fe, Co, Ru and Ir,[41,55,267,268] are drawing increasing attention from medicinal (inorganic) chemists because of their promising bactericidal,[41,47] anti-inflammatory,[269,270] anti-apoptotic,[270] anti-microbial[271] and anti-proliferative properties.[272]

To understand the biological properties of CORMs in detail, it is important to characterise their interactions with possible biological targets, to define the binding sites of the metal, and to determine which among the original ligands are still present upon formation of the adduct. The binding of CORMs to proteins can play an important role in their activation, transport, and in-vivo excretion.[273] A few structural studies of protein-CORM adducts have been performed, but the knowledge of how CORMs recognise

proteins and of the mechanism which allows CORMs to release CO in the presence of a protein is still rather limited. Crystallographic studies on the first protein-CORM adduct, carried out using hen egg white lysozyme (HEWL) as a model protein, have demonstrated that the Ru complex CORM-3 can bind to surface histidine and aspartic residues.[54] Subsequently, it has been shown that ruthenium-based CORMs can bind HEWL at diverse sites, i.e. close to His15, Asp18, Asp101 and Asp119.[53,274]

Recently, a structural characterisation of the adducts that are formed when HEWL reacts with the Ir-based CORM Cs_2IrCl_5CO has been performed.[43,55] It has been found that the adducts can be formed via covalent or non-covalent interactions either. Six different binding sites have been identified (His15 (site 1); Ser24, Asn27, and Val120 (site 2); Asn65 and Pro79 (site 3); Asp18 (site 4); Asn59, Trp62, Trp63, and Ala107 (site 5); and Asn46 and Thr47 (site 6)), although His15 seems to be the primary anchoring site for the Ir derivatives. Loss of CO in the crystal state has been also observed both via X-ray crystallography and Raman microspectroscopy.[55]

This section addresses for the investigation of the reactivity of Cs_2IrCl_5CO with the model protein bovine pancreatic ribonuclease (RNase A) by using mass spectrometry (MS), X-ray crystallography and Raman microspectroscopy. The stability of the adduct formed upon reaction of the protein with the potential metallo-drug has been also evaluated using circular dichroism.

6.2 Experimental section

6.2.1 Crystallization and data collection

The crystals of the adduct formed in the reaction between RNase A and $IrCl_5CO_2^-$ were obtained using a soaking procedure. In particular, crystals of RNase A have been grown over two weeks using a hanging-drop vapour-diffusion method with a reservoir solution containing 22% PEG 4K and 10 mM sodium citrate at pH 5.1. They have been soaked with a saturated solution of Cs_2IrCl_5CO. After four days (**crystal 1**) and two months (**crystal 2**) of soaking, these crystals have been fished out with a nylon loop, flash-cooled without cryoprotectants at 100 K using nitrogen gas and dehydrated under air,[275] as performed in other works.[276,277]

Data have been collected at 1.85 and 2.29 Å resolution for crystals 1 and 2, respectively, at the CNR Institute of Biostructure and Bioimages, Naples - Italy, using a Saturn944 CCD detector along with CuKα X-ray radiation from a Rigaku Micromax 007 HF generator, and processed using HKL2000. Details of the data collection statistics are reported in Table 4.

Table 4 - Data collection and refinement statistics. Values within brackets refer to last resolution shell.

Data collection	Crystal 1	Crystal 2
PDB code	5JMG	5JML
Space group	*C*2	*C*2
Unit cell parameter		
a (Å)	99.9	99.6
b (Å)	32.6	32.4
c (Å)	72.3	72.6
α (°)	90.0	90.0
β (°)	90.3	90.0
γ (°)	90.0	90.0
Observed reflections	55 190	24 425
Unique reflections	19 871	10 756
Resolution (Å)	72.27–1.85 (1.88–1.85)	72.59–2.29 (2.34–2.29)
Completeness (%)	97.8 (93.5)	96.5 (97.8)
Rmerge (%)	6.3 (40.6)	13.9 (55.7)
$I/\sigma(I)$	10.9 (2.3)	10.7 (2.0)
Multiplicity	2.8 (1.7)	2.3 (2.3)
Refinement		
Resolution (Å)	72.27–1.85	72.59–2.29
Number of reflections in working set	18 853	9837
Number of reflections in test set	1017	490
R factor (%)	17.2	22.4
R free (%)	22.6	29.3
R all (%)	17.5	22.7
Number of non-hydrogen atoms	2238	2027
Mean *B*-value (Å)	26.4	35.5
Ramachandran plot statistics		
Most favoured/additional allowed (%)	95.1/4.5	95.1/4.5
Generously allowed/disallowed (number of residues)	0/1	0/1
R.m.s.d. bonds (Å)	0.016	0.012
R.m.s.d. angles (°)	2.4	2.5

6.2.2 Structure solution and refinement

The structures of the two RNase A-$IrCl_5CO_2^-$ adducts have been solved with PhaserMR, using the A chain of the PDB file 1JVT as a starting model.[278] As expected,[278] these crystals contain two molecules in the asymmetric unit (molecule **A** and molecule **B**). The refinements have been carried out with CCP4 Refmac5[279] using

NCS restraints while the model building, map inspections and model adjustments have been manually performed with Coot v0.8.6.[280] The structures have been refined up to R-factor/R-free values of 0.172/0.226 and 0.224/0.293 for crystal 1 and crystal 2, respectively.
Table 1 reports the refinement statistics. Figures were created using the UCSF Chimera Package.[281] The refined structural models and structure factors were deposited in the Protein Data Bank as entries **5JMG** and **5JML** for crystal 1 and crystal 2, respectively.

6.2.3 Raman microspectroscopy

Raman microscopy spectra for the RNase A crystals and for crystals of the RNase A-$IrCl_5CO_2^-$ adduct have been collected by using a commercial Jasco N3100 microscope apparatus, Raman spectra of the Cs_2IrCl_5CO powder have been collected as references as well. A 514 nm excitation wavelength and a power at the sample of 3 mW have been used. The spectra resolution 7 cm^{-1}.

6.2.4 Mass spectrometry

MS analysis has been performed by co-authors using an LCQ DECA XP Ion Trap mass spectrometer (ThermoElectron) equipped with an OPTON ESI source (operating at a 4.2 kV needle voltage and 320 °C). The mass spectra have been recorded continuously over the mass range 400-2000 Da in positive mode.
Multi-charge spectra have been deconvoluted using a BioMass program included in the Bioworks 3.1 package provided by the manufacturer.

6.2.5 CIRCULAR DICHROISM

CD spectra of RNase A and of the adduct formed between the protein and $IrCl_5CO_2^-$ after 24h of incubation with 1:1 and 1:10 protein to metal ratios were recorded at 10 °C using a Jasco J-710 spectropolarimeter equipped with a Peltier-thermostated cell holder (Model PTC-348WI - Jasco).

The mean residue molar ellipticity, [θ] in deg cm^2 $dmol^{-1}$, has been calculated using the equation:

$$[\theta] = [\theta]_{obs} \times MRW/(10lc)$$

where $[\theta]_{obs}$ is the ellipticity measured in degrees, MRW is the mean residue molecular weight, c is the protein concentration in g mL^{-1} and l is the optical path length of the cell in centimetres.

Far-UV measurements (190-250 nm) have been carried out using a 0.1 cm path length cell and a protein concentration of 0.1 mg mL^{-1} in a 10 mM Tris-HCl buffer, pH 7.4. Prior the measurements, the instrument has been calibrated with an aqueous solution of d-10-(+)-camphorsulphonic acid at 290 nm. Thermal unfolding curves for the protein and the adduct have been recorded using the temperature mode at 222 nm with the same experimental conditions, meaning protein concentration of 0.1 mg mL^{-1} in a 10 mM Tris-HCl buffer at pH 7.4.

6.3 Results and discussion

6.3.1 Mass spectrometry

In order to study the reactivity of Cs_2IrCl_5CO with proteins, RNase A has been incubated in the presence of the Ir compound for 24h with a 1:10 protein to metal ratio, and the resulting products have been analysed using electrospray ionization mass spectrometry (ESI-MS). The results of this analysis are reported in Figure 34. The spectra of RNase A incubated in the presence of $IrCl_5CO_2^-$ reveal that a number of different Ir compound fragments can bind to the protein. In particular, when compared to RNase A spectra, new peaks have been detected in the ESI-MS spectra of the adduct, that have been assigned to a complex formed by RNase A with fragments like $-[IrCl_4CO]^-$ and $-[IrCl_3(H_2O)CO]$. Interestingly, more than one Ir fragment could bind to the protein at the same time and the observation of these peaks suggests that the CO is retained upon protein binding, while a Cl^- ligand is released.

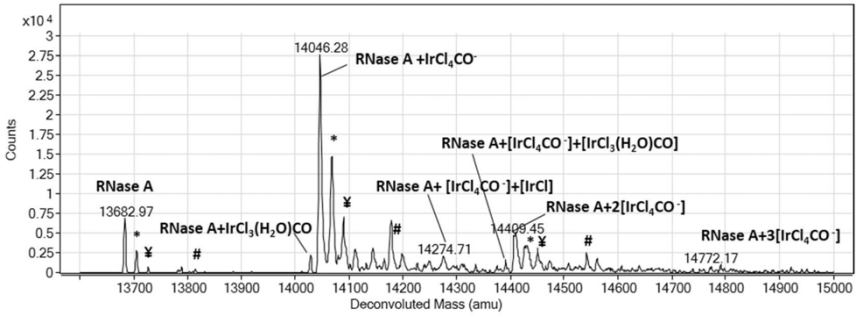

Figure 34 - Deconvoluted ESI-MS spectra for RNase A incubated for 24h at room temperature with 10^{-3} mol L^{-1} Cs_2IrCl_5CO dissolved in water (complex/protein = 10:1) in 20 mmol L^{-1} ammonium acetate buffer, pH 6.8. The symbols indicate the main peaks of several adducts: *: RNase A + Na^+, ¥: RNase A + $2Na^+$, #: RNase A + Cs^+.

6.3.2 CIRCULAR DICHROISM

In order to verify the effect of the $IrCl_5CO_2^-$ binding on the RNase A structural stability, CD spectra have been recorded (Figure 35) and the signal intensity at 222 nm monitored for increasing temperature values (from 10 °C to 95 °C - Figure 36). The far UV-CD spectra of RNase A and of the adducts formed upon 24h of incubation of the protein in the presence of the Ir compound at 1:1 and 1:10 protein to metal molar ratios are indistinguishable (Figure 36) at 10 °C in 10 mM Tris-HCl buffer at pH 7.4. They contain typical fingerprints of α/β proteins and the inspection of unfolding curves clearly indicates that the thermal denaturation of RNase A is not affected by the $IrCl_5CO_2^-$ binding (Figure 36).
These findings demonstrate that the binding of $IrCl_5CO_2^-$ fragments to RNase A does not perturb the overall protein conformation or structural stability neither.

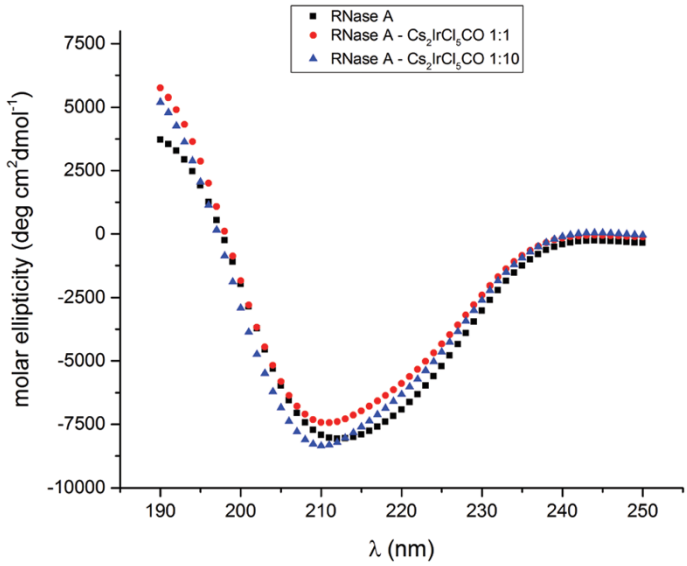

Figure 35 - Far-UV CD spectra of RNase A and RNase A-$IrCl_5CO_2^-$ adducts formed with 1:1 and 1:10 protein to metal molar ratios. Spectra have been collected at 10 °C using a protein concentration of 0.1 mg mL^{-1} in a 10 mM Tris-HCl buffer, pH 7.4.

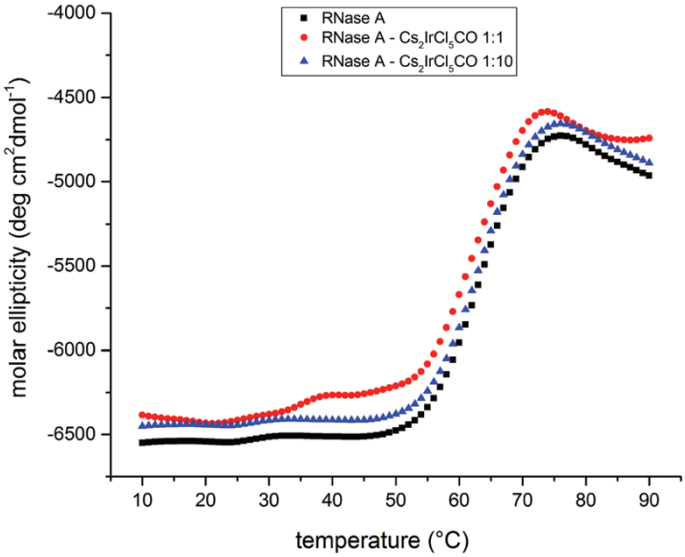

Figure 36 - Thermal denaturation of RNase A and RNase A-$IrCl_5CO_2^-$ adducts formed with 1:1 and 1:10 protein to metal molar ratios, as obtained from CD spectroscopy at 222 nm. Measurements have been carried out in 10 mM Tris-HCl buffer, pH 7.4, using an enzyme concentration of 0.1 mg mL^{-1}. Heating rate was 1.0 °C min^{-1}.

6.3.3 STRUCTURE OF THE ADDUCTS

To explore the reactivity of $IrCl_5CO_2^-$ with RNase A on structural ground, the structure of the adducts has been determined by X-ray crystallography, using two different datasets both collected on monoclinic crystals grown under the same conditions and containing two RNase A molecules in the asymmetric unit. These crystals differ each other in soaking time of the Ir compound. X-ray diffraction data for the first crystal have been collected after four days of soaking in a saturated solution of Cs_2IrCl_5CO, whereas data for the second crystal have been collected after two months. Interestingly, the two structures show a different number of Ir-compound binding sites. Indeed, five sites have been identified in crystal 1 (N-terminal amine, Met29, His105 and His119 in molecule A and His119 in molecule B), whereas eight sites have been found in crystal 2 (N-terminal amine, Met29, His12, His105 and His119 in molecule A, His12, His105 and His119 in molecule

B). In both cases, the structure of the protein is not significantly affected by the reaction with the CORM: the four disulphide bridges are retained and the CA root mean square deviations from a ligand-free protein under the same experimental conditions (PDB code 1JVT) is in the range 0.19-0.42 Å.

Figure 37 illustrates the asymmetric unit content for the structures of the two RNase A-$IrCl_5CO_2^-$ adducts.

The final model obtained for the RNase A-$IrCl_5CO_2^-$ adduct in crystal 1 (Figure 37A) includes 2238 non-hydrogen atoms and has been determined at a 1.85 Å resolution. This structure refines to an R-factor of 0.172 (R-free 0.226). The average B-factor for all atoms of the structure is 26.4 $Å^2$. A full list of the refinement statistics is reported in Table 1. Figure 38 shows the 2Fo-Fc electron density maps for the five Ir-compound binding sites identified in this structure. The occupancy factors for the Ir atoms are in the range 0.30-0.60. In molecule A, at the first Ir compound binding site, i.e. close to N-terminal amine, the Ir atom is bound to a Cl^- and is in contact with the side chain of Arg85 from a symmetry-related molecule (Figure 38A). This finding indicates that upon hydrolysis, Cs_2IrCl_5CO can act as a cross-linker, bridging different protein chains, as already observed for cisplatin and other metallodrugs.[282,283] At this site, the electron density maps do not allow for a complete elucidation of the iridium coordination sphere.

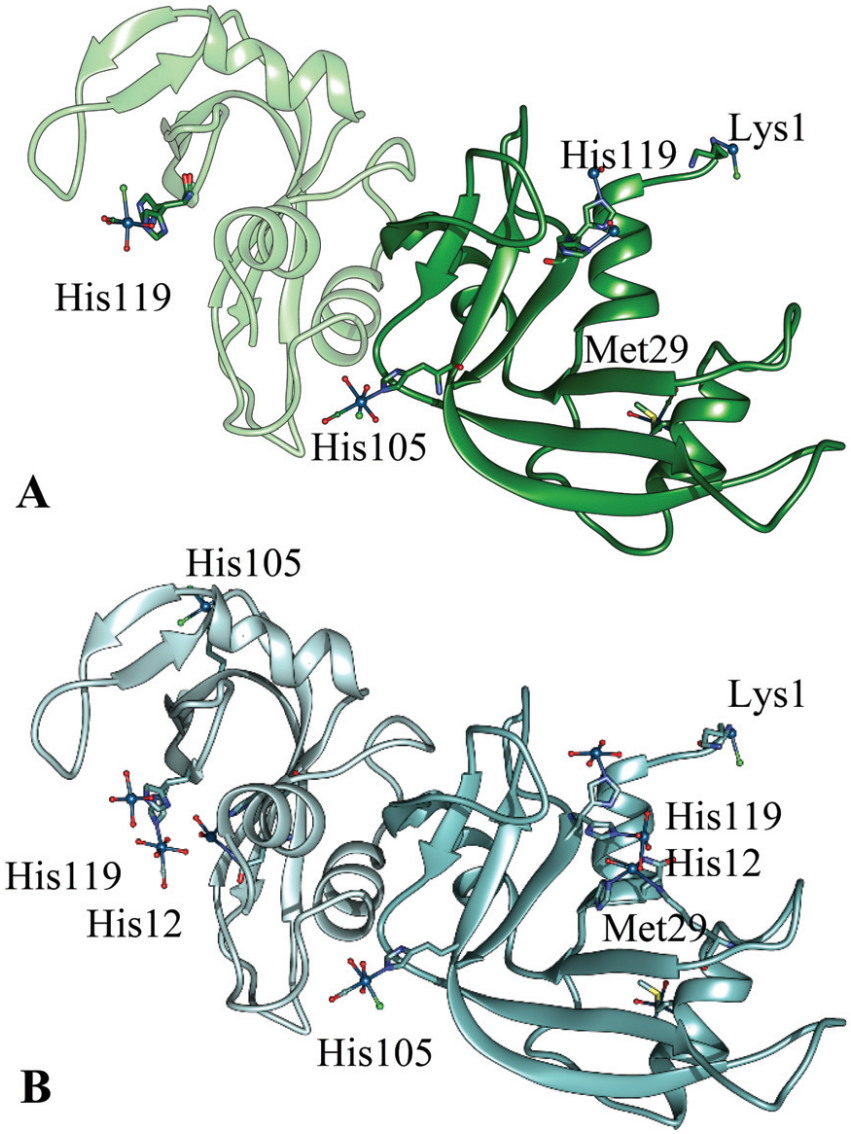

Figure 37 - Cartoon diagram of the RNase A structures in the asymmetric unit from crystal 1 (**A**) and crystal 2 (**B**). Ir compounds are represented by ball and stick structures, as are the residues involved in the compound recognition (N-terminal Lys, His12, Met29, His105, and His119). Molecule A is on the right.

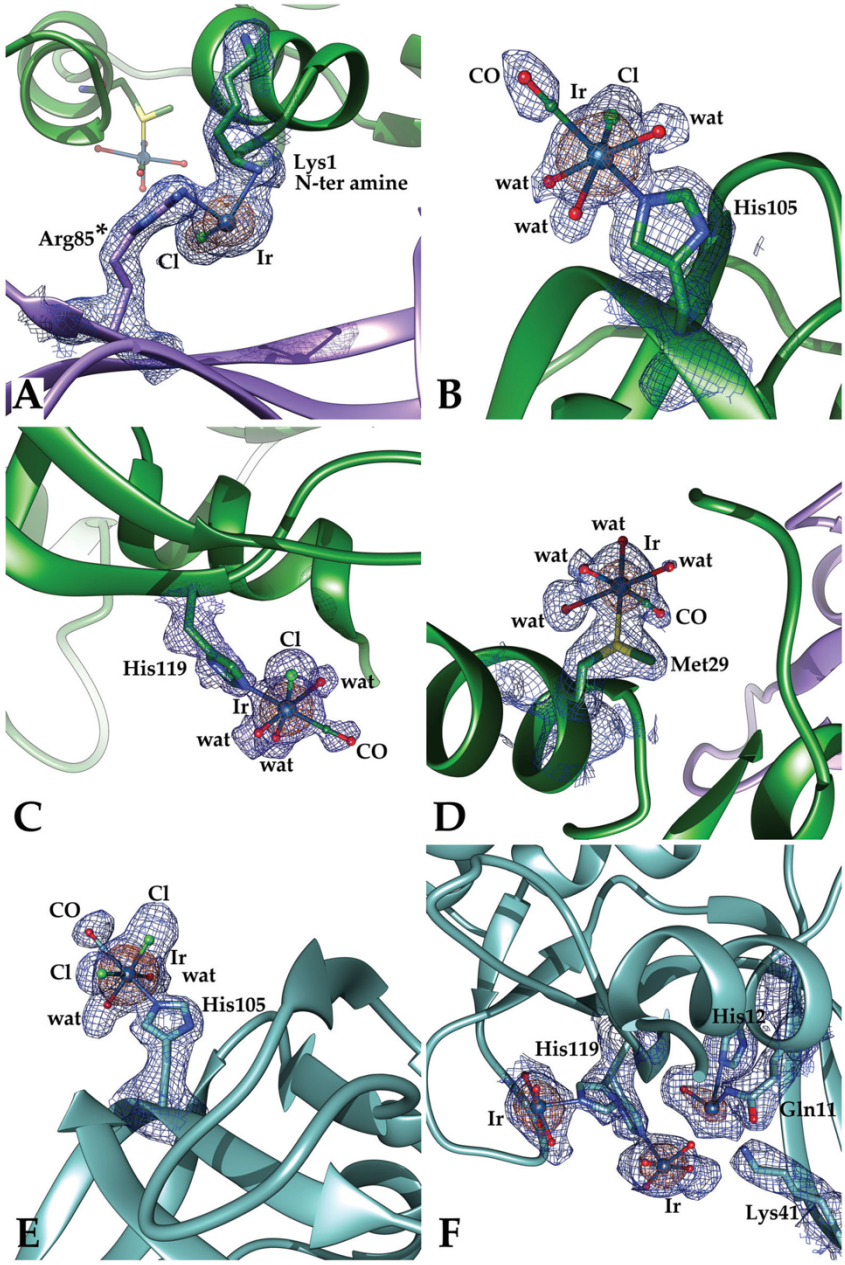

Figure 38 - Details of the $IrCl_5CO_2^-$ binding sites in crystal 1 (**A**–**D**) and of the additional $IrCl_5CO_2^-$ binding sites in crystal 2 (**E**, **F**). (**A**) N-terminal amine (molecule A), (**B**) His105 (molecule A), (**C**) His119 (molecule B), (**D**) Met29 (molecule A); (**E**) His105 (molecule B of crystal 2); (F) His12 in the active site cleft (molecule A from crystal 2). 2Fo-Fc electron density maps are contoured at 1.5σ (blue) and 2.5σ (orange) levels.

In molecule A, at the binding site close to the His105 side chain, a $[IrCl(H_2O)_3CO]^{2+}$ fragment is bound to the protein (Figure 38B). The same fragment is bound to the active site residue His119 of molecule B (Figures 38C and 39). The product of hydrolysis of this fragment, i.e. $[Ir(H_2O)_4CO]^{3+}$, is linked to the Met29 side chain of molecule A (Figure 38D), with a CO ligand occupying an equatorial position with respect to the Met side chain. The observation of this binding site is interesting because even though Ir-based compounds are known to bind protein sulphur sites,[55] the interaction between sulphur containing residues and Ir complexes has never been described from a structural point of view. Finally, the Ir compound fragment bound to His119 of molecule A presents a metal coordination shell completed by water molecules (Figure 39).

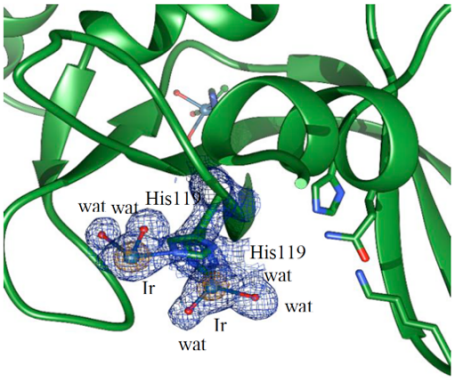

Figure 39 - Details for the $IrCl_5CO_2^-$ binding site close to His119 of molecule A from crystal 1. 2Fo-Fc electron density map is contoured at 1.5 σ (blue) and 2.5 (orange) level.

The structure of the RNase A-$IrCl_5CO_2^-$ adduct in crystal 2 has been refined at a lower resolution (2.29 Å). This model includes 2027 non-hydrogen atoms and refines to an R-factor of 0.224 (R-free 0.293). In this structure, three additional Ir binding sites were identified compared to those observed in crystal 1 (Figure 38 E, F). The occupancy factors of the Ir atoms are in the range 0.30-1.00. A full list of the refinement statistics is reported in Table 4. The first two additional binding sites are close to His12 in the two molecules, in the active site clefts. In these sites, the metal is bound to His12 and Gln11 side chains (Figure 38F) and is modelled as an alternative to the Ir compound bound to His119.

The other additional binding site has been observed at the side chain of His105 of molecule B (Figure 38E). Here, a $[IrCl_2(H_2O)_2CO]^+$ fragment is bound to the protein.

Interestingly, in this structure the fragment bound to His119 of molecule B ($[Ir(H_2O)_4CO]^{3+}$) is different when compared to the one found in crystal 1 ($[IrCl(H_2O)_3CO]^{3+}$ - Figure 38C), suggesting that ligand exchange processes are possible upon protein binding.

Additional details of the Ir compound fragments identified in the two structures are reported in Table 5.

Table 5 - Additional details of the Ir compound fragments identified in the two structures of RNase A–$IrCl_5CO_2^-$ and the interactions that they form with protein residues

	Crystal 1				Crystal 2			
Chain	Site	Fragment[a]	Interaction	Distance (Å)	Site	Fragment[a]	Interaction	Distance (Å)
A	**His 105**	$[IrCl(H_2O)_3CO]^{2+}$	Ir E–Cl2	2.0	**His 105**	$[IrCl(H_2O)_3CO]^{2+}$	Ir E–Cl3	2.3
			Ir E–HOH3	2.0			Ir E–HOH2	2.0
			Ir E–HOH4	2.3			Ir E–HOH4	2.0
			Ir E–HOH5	2.5			Ir E–HOH5	2.0
			Ir E–NE2	2.2			Ir E–NE2	2.3
			Ir E–C6	2.3			Ir E–C 6	2.0
	Met 29	$[Ir(H_2O)_4CO]^{3+}$	Ir L–C2	2.0	**Met 29**	$[IrX(H_2O)_3CO]^{3+}$	Ir L–C 2	2.0
			Ir L–HOH3	2.6			Ir L–HOH3	2.0
			Ir L–HOH4	2.9			Ir L–HOH4	2.0
			Ir L–HOH5	2.6			Ir L–HOH5	2.0
			Ir L–HOH6	2.0			Ir L–SD 29	2.3
			Ir L–SD	2.6				
	His 119 A	$[Ir(H_2O)_2X_3]^{3+}$	Ir G/A–HOH 2/A	2.0	**His 119 A**	$[Ir(H_2O)_4X]^{3+}$	Ir G/A–His119/A NE2	2.2
			Ir G/A–HOH 260	2.7			Ir G/A–HOH 2/A	2.0
			Ir G/A–His 119 ND1/A	2.6			Ir G/A–HOH 3/A	2.0
			Ir G/A–His 119 ND1/B	2.4			Ir G/A–HOH 4/A	2.0
							Ir G/A–HOH 5/A	2.0
	His 119 B	$[Ir(H_2O)_3X_2]^{3+}$	Ir G/B–His119 NE2/B	2.3	**His 119 B**	$[Ir(H_2O)_4X]^{3+}$	Ir G/B–His119/B NE2	2.3
			Ir G/B–HOH 2/B	2.4			Ir G/B–HOH 2/B	2.0
			Ir G/B–Glu111 OE2/B	3.0				
			Ir G/B–HOH 134	2.9			Ir G/B–HOH 3/B	2.0
			Ir G/B–HOH 199[a]	2.8			Ir G/B–HOH 4/B	2.0
							Ir G/B–HOH 5/B	2.0
	Lys 1	$[IrClX_4]^{2+}$	Ir F–Lys1 N	2.8	**Lys 1**	$[IrClX_4]^{2+}$	Ir M–Cl 2	2.6
			Ir F–Cl2	2.3			Ir M–N	2.3
			Ir F–Arg85[a] NH2	2.7				
					His 12	$[Ir(H_2O)X_4]^{3+}$	Ir J/A–His12 NE2	2.8
							Ir J/A–HOH 2/A	2.0
							Ir J/A–Gln11 NE2	2.6
B	**His 119 A**	$[IrCl(H_2O)_3CO]^{2+}$	Ir I/A–Cl 2/A	2.7	**His 119 A**	$[Ir(H_2O)_4CO]^{3+}$	Ir I/A–His 119/A NE2	2.2
			Ir I/A–HOH 3/A	2.5			Ir I/A–HOH 2/A	2.0
			Ir I/A–HOH 4/A	2.0			Ir I/A–HOH 3/A	2.0
			Ir I/A–HOH 5/A	2.0			Ir I/A–HOH 4/A	2.0
			Ir I/A–C 6/A	2.0			Ir I/A–HOH 5/A	2.0
			Ir I/A–His119/A NE2	2.2			Ir I/A–C 6/A	2.0
					His 119 B	$[Ir(H_2O)_4X]^{3+}$	Ir I/B–His 119/B NE2	1.9
							Ir I/B–HOH 2/B	2.0
							Ir I/B–HOH 3/B	2.0
							Ir I/B–HOH 4/B	2.0
							Ir I/B–HOH 5/B	2.0
					His 105	$[IrCl_2(H_2O)_2CO]^+$	Ir F–Cl 2	2.2
							Ir F–Cl 3	2.6
							Ir F–HOH 4	2.0
							Ir F–HOH 5	2.6
							Ir F–NE2	2.2
							Ir F–C	2.0
					His 12	$[Ir(H_2O)X_4]^{3+}$	Ir K/B–His12 NE2	2.7
							Ir K/B–HOH 2/B	2.1
							Ir K/B–Gln11 NE2	2.6

[a] Water molecule ligands in the identified Ir compound fragments could be deprotonated.

6.3.4 Raman microspectroscopic studies

Raman spectra have been collected to obtain unambiguous evidence of the presence and persistency (no release) of CO within the crystals of the adduct (Figure 40). The Cs_2IrCl_5CO powder shows signals due to Ir-Cl bond stretching in the 300-400 cm^{-1} region and a signal at about 2080 cm^{-1} assigned to the CO ligand, also according to previous findings.[55]

Looking at the spectra collected over 2 weeks from the $IrCl_5CO_2^-$ soaking, it shows that the metallo-drug is able to enter into the protein crystals as marked by the appearance of the high-frequency band at 2073 cm^{-1}, after just a few minutes from the Ir soaking. This spectral feature it due to the CO bound to the metal centre and remains stable for two weeks suggesting that the CO ligand is not released under the experimental conditions.

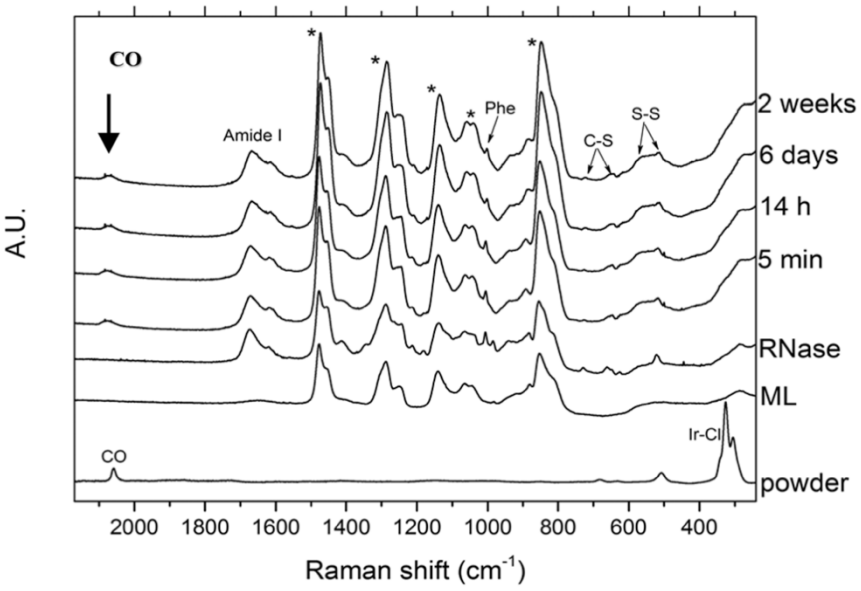

Figure 40 - Raman spectra of the Cs_2IrCl_5CO powder and RNase A crystal, and of protein crystals soaked in a saturated solution of Cs_2IrCl_5CO as a function of time. The star refers to signals from the buffer. Excitation line wavelength is 514 nm with power at the sample of 3 mW and spectral resolution of 7 cm^{-1}. The CO band persistency indicates that no CO release is occurring in the crystals of the adduct.

This is conflicting with evidences form previous study on the reactivity of the same compound within lysozyme crystals,[55] where $IrCl_5CO_2^-$ has been shown to be able to release the CO ligand as demonstrated by the appearance of new Raman spectral features in the 2000-2200 cm^{-1} region (CO stretching region, see Figure 9 and 10 in Petruk et al.[55]). In addition, the band at around 300 cm^{-1} related to the Ir-Cl stretching appear sizeably attenuated in the case of RNase A, differently from previous Raman records from the lysozyme-$IrCl_5CO_2^-$ adduct (crystals grown in 1.2 M NaCl).[55] The different behaviour clearly relates to the NaCl-free condition for the study the formation of the RNase A-$IrCl_5CO_2^-$ adduct, which likely undergoes to hydrolysis reaction. By contrast, the much slower Cl^-/H_2O exchange observed for the HEWL-$IrCl_5CO_2^-$ adduct relies and the high concentration of Cl^- ions in the solution used to obtain the HEWL crystals.

6.4 Conclusions

Interactions between CO-releasing compounds and biological macromolecules have received increasing attention over the past decade. Here I reported a combination of spectrometric spectroscopic crystallographic investigations for unveiling the molecular bases of protein/Ir-based CORM recognition.

Basing on findings in this work, the following concluding marks can be drawn:

a) $IrCl_5CO_2^-$ tightly binds to RNase A at its N-terminal amine and at the His12, His105, His119 and Met29 side chains. Histidine residues have been earlier found to bind Ir-based metallo-drugs in other structures,[55] but details for the Met-Ir interactions and for the N-terminus involvement have never been shown before though sulphur-containing ligands are strong binding sites for heavy transition metal ions. For example, it has been shown that cisplatin and carboplatin bind to the sulphur atom of Met29 of RNase A,[209,282,284] to the cytochrome c Met65 sulphur atom,[285] and to the Met side chains of Na^+/K^+ ATPase[286] and human serum albumin.[287]

b) $IrCl_4CO_2^-$ and the products of its hydrolysis bind to the protein.

c) the formation of the adduct does not significantly affect the overall enzyme structure.

d) the RNase A-$IrCl_5CO_2^-$ adduct is stable under the investigated experimental conditions.

e) the adduct formed in the reaction between RNase A and the $IrCl_5CO_2^-$ compound retains a significant amount of CO for at least two months, further confirming the idea that the

formation of complexes between proteins and CORMs can be used for modulating the kinetics of CO release.[55,288,289]

f) the adduct has the same thermal stability as the ligand-free protein.

These findings gain a larger relevance putting this work in the general framework of iridium compound-protein interactions.

Iridium complexes have received considerable attention in very diverse fields such as catalysis,[290] optoelectronics and inorganic photochemistry,[290,291] medicinal inorganic chemistry and biology.[292] Furthermore, they work as chemo-sensors for live cell imaging and in-vivo tumour imaging,[37,293] as well as protein-protein interaction inhibitors. Negatively charged Ir complexes alike $(IrCl_6)^{3-}$ have been proved to bind basic protein regions i.e. His residues through nucleophilic substitution of a metal ligand, usually a chloride, by the imidazole.[55]

Taking advantage of these properties, the cyclometalated Ir(III) solvato complex $[Ir(ppy)_2(solv)_2]^+$ has been used as a selective luminescent switch-on probe for His-rich proteins.[294] By contrast, positively charged complexes like $(Ir(NH_3)_6)^{3+}$ are likely to bind acidic regions in the protein.

This section shown Ir(III) complexes to be also able to bind Met side chains and N-terminal amines helping to understand and predict the biomolecule-Ir compound interactions, as well as support future drug design.

At last, it is worth noting that the two Raman studies for lysozyme and RNase A with $IrCl_5CO_2^-$ suggest a possible correlation between the CO-releasing ability of the Ir compound and its Cl^-/H_2O content, at least in the time scale of the Raman analysis (2 weeks): the higher the content of Cl^- in the coordination sphere, the faster the CO release within the crystal though further studies are needed to validate this hypothesis.

7

Ruthenium prodrug release from protein

The Ru(III) drug AziRu efficiently binds proteins but its release mechanism remains disputed. Herein, we perform a Raman-assisted crystallographic study of AziRu binding to lysozyme and its chemical reduction to test the Ru release conditions, by using three different reducing agents. Different outcomes have been achieved spanning from the complete crystal dissolution, through a complete Ru release up to the Ru reduction without release. The aggregate of our spectroscopic and crystallographic findings highlights the reduction to be necessary though no self-sufficient in the prodrug activation/release mechanism. At last, these findings support the possible environ-specific activation of the prodrug within cancer environments because of the different chemical conditions as compared to healthy tissues.

7.1 INTRODUCTION

Last decades saw a significant increase of the ruthenium-based designs as anti-cancer agents.[16] Notwithstanding that the details of their mechanisms of actions remain unclear, ruthenium-based drugs are known to owe much of their success in the current anticancer panorama to the ease they access different oxidation states under physiological conditions.[16,81] Ru(III) is the prevailing and most stable form though marginally anticancer active and largely bound to blood-plasma proteins once administered, essentially acting as a prodrug.[4,58,64] Indeed, Its anti-tumour potential has been proven to rely on the reduction to Ru(II),[61,82,83] widely recognised as the utmost anticancer-active ruthenium form.[4,58,64] Ru(II), alike Ru(IV), can be promptly accessed in the presence of ordinary biological redox agents, particularly abundant within cancer environs opening perspective for possible selective drug activation.[4,25,64,82-85] In addition, the structures, speciation in biological environs, exact molecular targets and action mechanisms have not yet been elucidated.[16]

A number of complexes have been proposed and, albeit none of them has achieved to reach actual clinical usage as yet, two acclaimed complexes introduced roughly at the same time, namely NAMI-A, and KP1019 have both reached phase II in clinical trials showing remarkable performance.[11,16,58,59,62]

The subject of this study is the recently proposed **AziRu** complex, whose structure differs from NAMI-A for a pyridine ring in place of imidazole (Figure 41).[295] It has proven to possess a higher cytotoxicity and anti-proliferative capacity than its imidazole-substituted counterpart.[295,296] Tests in conjugation with nanocarriers have proven a sizeable increase in the cell delivery rate as well,[296] whilst the combination of X-ray crystallography and

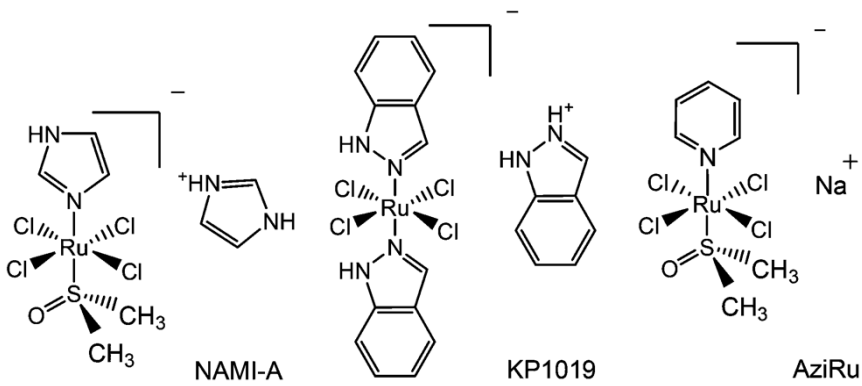

Figure 41 – Chemical structures of the most representative Ru-based compounds NAMI-A and KP1019 as compared to the novel pyridine-substituted AziRu complex (refer to body text and section 1.5.

Raman microspectroscopy granted evidences from a structural point of view on interaction with the two model proteins, RNase A and Lysozyme, as well as shedding light on the ligand exchange process.[18,297]

Electron-paramagnetic resonance has given clues for the plasma proteins-mediated transport of aquated Ru(III) species, also indicating the binding to occur through Cys and His side chains.[298] Previous crystallographic studies supported by Raman findings on the binding of AziRu with lysozyme, ribonuclease, and cytochrome c, report the binding to occur via His, Asp and Arg side chains.[16-18,297]

In aqueous solution, the AziRu undergoes to the aquation process and the early solution appears yellowish (Cl^- yet dominant in the coordination sphere) and turns greenish within hours (sizeable aquation), then black at longer time because of the Ru(IV) polyoxoruthenate species formation, characterised by Ru(IV)-O_n-Ru(IV) bridges. The time scale of this sequence of events has been demonstrated to depend on several factors, including pH and Cl^- concentration. The ligand exchange process quickly begins with the release of the DMSO group, which can be observed exclusively in the solid state indeed. Afterwards, at least

three out of the four Cl^- anions are replaced by H_2O/OH^-, depending on the pH: the higher the pH[296] and the lower the Cl^-,[18,297] the faster the process. The course of events goes on until the Ru(IV) polyoxoruthenate species responsible for the black colour appear. This stage goes as faster as higher the Cl^- concentration possibly suggesting the involvement of a leaving chlorine group.

Herein, a combined crystallographic-Raman structural study of AziRu with a model protein (lysozyme), focusing on the chemical-mediated Ru reduction and its release from the protein. Three reducing agents have been used in a twofold strategy: 1) crystallography has been used to identify the structural changes and release occurring upon Ru(III) reduction to Ru(II) by alternative exposure to hydrazine, ascorbate or sodium borohydride and 2) Raman microscopy on protein single crystals has been performed to identify the spectral changes due to the reduction of Ru(III) bound to the protein. Here-hence this study is meant to clarify whether a) ruthenium ion gets actually released from lysozyme upon chemical reduction and b) Raman can distinguish Ru coordination/oxidation state and detect Ru(II) release.

7.2 Experimental

HEWL crystals have been grown by hanging-drop vapour diffusion mixing 1 μL of 15 mg/mL protein in sodium acetate at pH 4.5 to 1 μL of sodium chloride 1.1 M, sodium acetate 50 mM at pH 4.5. Very well-shaped crystals had rapidly grown within 48 h and have been soaked by merging a 2 μL drop of a 15 mM AziRu aqueous solution to the 2 μL crystal drop. The solution had suddenly turned yellowish and so have had the crystals upon AziRu exposure, thus turning to a greenish colouration in a timescale of hours and eventually had become dark brown/black in 1 week. Crystals had been kept at 20 °C throughout the whole crystallization, soaking and colour shift process. Raman data have been collected at increasing time from soaking until the formation of black crystals by using a commercial Jasco NSR-3100, a 514 nm excitation laser line (3 mW at sample power, 20x lens) directly in the crystallization well.

Black crystals have been exposed to the alternative reduction with sodium borohydride, hydrazine, and ascorbate. Different reducing agent concentrations have been tested (10-100 mM) but no significant differences have to be reported. The best looking black crystals have been chosen for the X-ray data collection, which had been performed using a Saturn944 CCD detector along with CuKα X-ray radiation from a Rigaku Micromax 007 HF generator, and processed using HKL2000.[299] The very same black crystal used for the reference dataset collection has undergone to reduction and hence re-used for X-ray data collection. The phasing has been carried out by molecular replacement using PhaserMR[300] and the 4J1B model from the PDB as template. Crystallographic refinements have been performed using Coot 0.8.6,[280] and REFMAC5 from the CCP4 software suite.[279]

7.3 Results

Upon exposure to the AziRu solution, the lysozyme native crystals have swiftly turned yellowish (minutes), then greenish (hours) and lately black (≥1 week), consistently with previous records.[18,297] As far as this text is drafted, black crystals have been stable for 1 year.

The Raman spectra from the native ad black crystals have been collected as starting references for the reduction/release process (Figure 42). The black crystal trace shows very strong Raman bands in the low frequency region arising from the Ru(III)-OH_2/OH^- (400-500 cm^{-1}) and Ru(IV)-O-Ru(IV) (500-700 cm^{-1}) accordingly to previous assignment.[18,297] The crystallographic structure of the black crystal has been solved (Table 6, Figure 43A) and, as expected, the model closely resembles the previously solved structure (PDB accession 4J1B).[297] The Ru binding site is appreciable nearby the His15 side chain (Ru-NE2 at 2.4 Å) and its occupancy has been evaluated as 0.5. The ruthenium bound to the His15 exhibits octahedral geometry tough the sixth ligand (wat in Figure 43A and C) could not be interpreted as part of the Ru coordination sphere because of the significant geometrical distortion. This can be possibly made plain with the steric hindrance from the very close Asp87 side chain.

Chemical reduction has been performed on black crystals using three different reducing agents. The exposure to borohydride has rapidly wreaked the crystal, like enough because of the might hydrogen sparkling and neither Raman nor crystallographic investigations have been possible. By contrast, hydrazine has driven to a colourless, native-like crystal whose Raman spectrum and crystallographic structure (Figure 43B) are utterly undistinguishable from native lysozyme crystals grown in the same

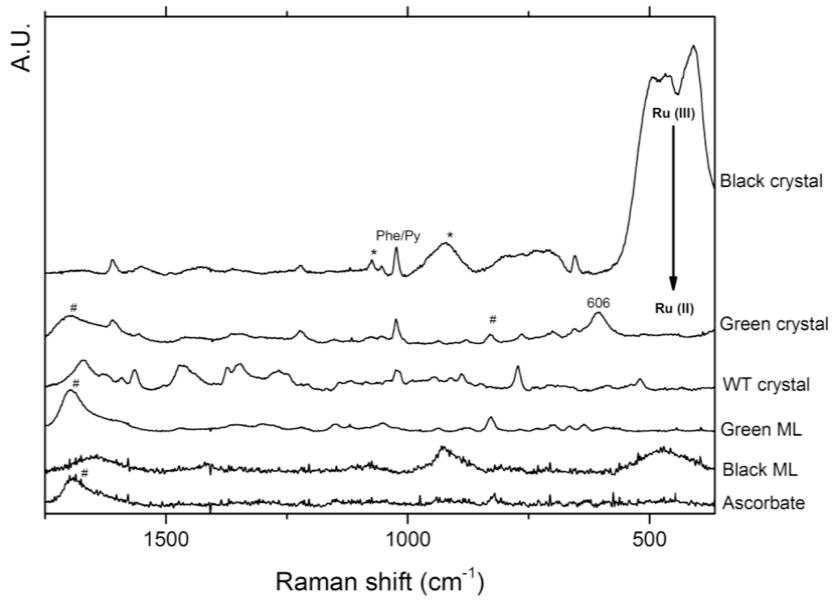

Figure 42 – Non-resonant Raman for the reduction of lysozyme-AziRu(III) (black crystal) the lysozyme-AziRu(II) (green crystals) upon ascorbate exposure. Wild-type lysozyme crystal spectrum is also reported as a reference, as well as mother liquor from green and black crystal either. Spectral features marked as (*) refer to signals from the mother liquor, whereas those labelled with (#) refer to signals arising from ascorbate.

conditions, clearly indicatory of a complete release of Ru from the protein upon reduction, like enough through:

$$Ru(III)_{(aquated)}\text{-}HEWL \rightarrow Ru(II)_{(aquated)}\text{-}HEWL \rightarrow Ru(II)_{(aquated)}$$

In fact, upon hydrazine addition the X-ray structure, solved at 2.55 Å and refined up to R and R_{free} of 0.193 and 0.293 respectively, does not show any residual Ru density (Figure 43B) and resembles the structure of wild-type lysozyme crystals grown in the same conditions (Figure 43D, PDB 5L9J) as also confirmed by the low 0.279 Å RMSD calculated by superposing the hydrazine-reduced model to the PDB 5L9J.[301]

By contrast, upon reduction with ascorbate the black crystal has turned back to green and stably remained so, long enough to allow for Raman and X-ray diffraction data collections.

The Raman spectrum distinctly changes losing completely the very strong Ru(III)-H_2O/OH^- signals in the low frequency region (Green

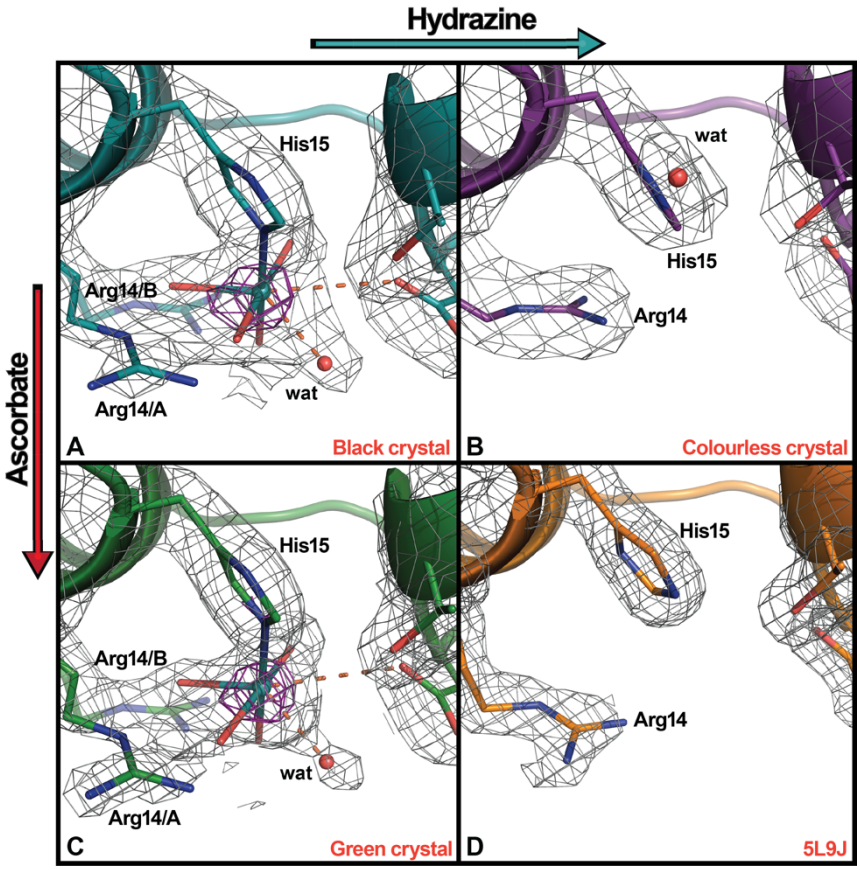

Figure 43 – Crystallographic close up for the His15 Ru binding site. All models are countered with 2Fo-Fc at 1σ (grey mesh) and 3σ (purple mesh). For sake of clarity, non-interacting water have been hidden. **A**) Detail for the Black crystal before the chemical reduction. **B**) Upon reduction with hydrazine no Ru density is detectable. **C**) Upon reduction with ascorbate no significant structural modifications are appreciable and Ru density is almost unperturbed. **D**) The native lysozyme structure from crystals grown in the same condition is reported as reference (PDB 5L9J).

crystal trace in Figure 42), whilst a new spectral feature arises at around 606 cm^{-1}. Literature does not support for any Ru(II)-protein species assignment. Gas-phase DFT calculations are being performed to explore possible Ru(II)-related modes.

The crystallographic structure for the ascorbate-reduced crystal (Green crystal) has been solved at 1.86 Å and refined up to R and R_{free} of 0.178 and 0.255 respectively (Table 6). Differently from the crystal reduced with hydrazine, it has revealed the persistence of the Ru atom bound to the His15 with almost no differences as compared to the black crystal structure (Figure 43C).

Electron-density maps indicate that no disulphide reduction occurs and the Ru site keeps its occupancy and coordination geometry. The RMSD value obtained by superposing the Green over the Black crystal is as low as 0.125 Å, denoting the models to be almost identical.

The aggregate of the disappearing Ru(III)-H_2O/OH^- Raman features, persisting Ru-density and geometry in the reduced crystal structure, indicates that upon ascorbate addition a Ru(II) specie bound to the protein could have been trapped, schematically as:

$$Ru(III)_{aquated}\text{-}HEWL \rightarrow Ru(II)_{aquated}\text{-}HEWL$$

In this case, no Ru(II) release is observed, thus ascorbate is able to reduce Ru(III) to Ru(II) yet bound to protein without triggering the Ru release as seen with hydrazine, at least in our experimental condition.

Table 6 – Refinement statistics for the AziRu soaked crystal (Black), the ascorbate reduced (Green) and the hydrazine reduced (Colourless) crystals.

	Black crystal (AziRu soaked)	Green crystal (ascorbate)	Colourless crystal (hydrazine)
Resolution (Å)	2.31 [2.25]	1.91 [1.86]	2.62 [2.55]
Working set (n.)	5073	9339	3783
Test set (n.)	251	467	179
Rfactor (%)	18.7	17.8	19.3
Rfree (%)	28.1	25.5	29.3
Rall (%)	19.16	18.31	20.1
Non-hydrogen atoms (N.)	1164	1177	1103
Mean B-value ($Å^2$)	42.88	35.33	45.11
Favoured (%)	98.4	98.4	92.1
Allowed (%)	1.6	1.6	7.9
Outliners (%)	0	0	0

7.4 Conclusions

Raman-assisted crystallography has been applied to the structural characterisation of the chemically induced reduction of the ruthenium prodrug AziRu bound to protein crystals. The outcome evidently hangs on the reducing agent. Hydrazine has brought to native-like lysozyme crystal since no trace of residual ruthenium electron-density has been found and the Raman spectrum is utterly identical to the native one, convincingly supportive for the Ru release from the protein. By contrast, ascorbate has yielded the AziRu-soaked black crystal (Ru(II)/Ru(III)) firmly back to green (Ru(II)). This has come besides thorough modifications of the Ru-related Raman features, albeit no perturbation in the crystallographic structure has been appreciable.

These findings open new structural and spectroscopic insights on the reduction-dependent ruthenium prodrug activation and release from proteins, a key point in the bigger selective drugging picture. Additional corroborations are reported in the chapter to come but blind spots remain regardless. To this end, gas-phase DFT calculations are being performed by prof. Hildebrandt's team at the Technische Universität of Berlin. Next chapter addresses for the investigation of key physical-chemical forces driving the ruthenium prodrug activation by means of SERS electro-spectroscopy and voltammetry.

8

On-electrode Ruthenium prodrug SERS

This section accounts for the investigation of some key physical-chemical properties of the Ru-based prodrug AziRu, relevant in terms of pharmacokinetics and dynamics, deepening the structural considerations on Ru release process reported in Chapter 7. The potential- and pH-dependent behaviours of AziRu have been studied through a SERS-based approach giving interesting clues on the possible selective drug release and activation within cancer environment. The investigation has been conducted in the laboratories of professor Peter Hildebrandt at the Institut für Chemie, Technischen Universität – Berlin.

8.1 Introduction

The drug effectiveness goes far beyond its mere cytotoxic or anti-proliferative activities as it does not matter how powerful the drug if the fix gets worse than the illness itself. The utmost pressing and trending topic in current drug design course is *selectivity*, meant as a whole of pharmacological facets making a drug able to pick out malignant targets avoiding regrettable impacts on healthy cells, tissue, physiological pathways etc. Selectivity is attained mostly by means of two routes: a) selective drug delivery and b) selective drug activation. The former includes deploying nanocarriers, nanoparticles, molecular decoration etc., whereas the latter can be achieved through diverse approaches e.g. photo-mediated, pH or redox dependent activation.[4]

Cancer cells and tissues indeed exhibit a bunch of sizeably different chemical features as compared to healthy ones, which can be exploited as target labelling features. The high proliferation rate of transformed cells prompts severe increase of hypoxia metabolism and therefore an extracellular lumen pH acidification as low as 6, as compared to the physiological 7.4.[4] In addition, tumour progression invariably goes through hindering the ROS processing ability giving rise to more radical-rich reducing environment.[302]

The *"activation by reduction"* hypothesis,[64,82,87] first advanced for platinum prodrugs, applies to every system able to access its active drug form upon reduction, or oxidation by extent, within malignant conditions. Ruthenium complexes are fully compliant to this definition as the Ru(II) is anticancer active,[61,82,83] whereas its oxidised counterpart Ru(III) is not, yet much more stable under physiological conditions in return.[4,16,58,64,81]

The novel Ru(III) prodrug AziRu (Figure 41), derived from NAMI-A, whose chemical-prompted reduction from a structural point of view is dealt in Chapter 7, does not make exception.

This section goes into investigating the AziRu pH- and reduction potential-related behaviours by means of Surface Enhanced Raman Spectroscopy (SERS) performed on electrodes at controlled applied potential, to grasp whether AziRu is compatible with a selective pH- and/or reduction potential-related activation within cancerous surroundings. Indeed, earlier studies on its parent compound (NAMI-A) have demonstrated the pH to sensibly affect the ligands exchange kinetics and the Ru(III)/Ru(II) redox potential by way of H_2O/OH^- shift.[303]

For the sake of the electrodes functionalisation this study has been carried on by using the AziRu derivative compound as reported below (Figure 44):

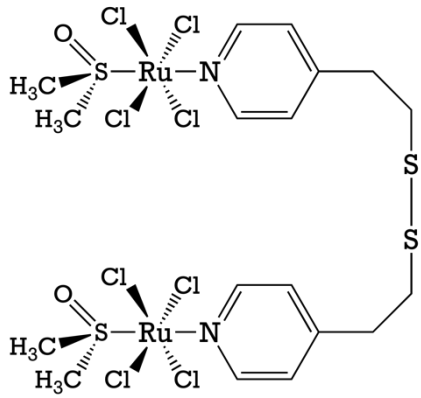

Figure 44 – AziRu derivate compound used for on-electrode SERS experiments. The disulphide grants high reactivity towards the Au surface.

8.2 Experimental

The disulphide derivate of AziRu has been synthesised by prof. Montesarchio and co-workers whereas all of the experimental activities to follow have been carried out within the laboratories of prof. Peter Hildebrandt and the precious support of dr. Jacek Kozuch, during my stay in Berlin.

8.2.1 Electrodes preparation

Silver and gold ring electrodes either have been tested in combination with different laser lines (413, 514 and 647 nm) for the purpose of SERS collections. Satisfactory results have been achieved with gold electrodes combined with the 647 nm line, and the information to follow are to be meant as solely referred to Au electrodes from now on.

The success of the electrode functionalisation process strictly depends on a proper and deep cleaning of its surface, made throughout a mechanical, chemical and electro-chemical procedure.

A first rough mechanical cleaning step relies on using abrasive fine dust and sandpaper with progressively narrowing texture, hence washes with distilled water. The electrode is afterwards immerged into a 1:1 (v/v) hydrogen peroxide/sulphuric acid solution till the complete reaction exhaustion for the harsher chemical treatment, washed again with water and finally dipped into an ultrasonic bath for at least 15 minutes and rinsed with water again.

A last, the gold surface roughening goes through an electrochemical process by using potassium chloride 0.1 M as electrolyte solution and hundreds of redox cycles under protective argon atmosphere. A very similar process has been adopted to prepare pin gold electrodes deployed for cyclic voltammetry measures.

8.2.2 Laying down AziRu monolayer

Gold ring electrodes are now ready for a final thorough wash with distilled water/ethanol, hence carefully dried under nitrogen flux. AziRu self-assembled monolayer (AziRU-SAM) is obtained by dipping the so prepared electrode into a 1:1 water/ethanol 15 mM AziRu derivate solution, the bowl cautiously sealed with Parafilm® and kept in the dark for 1 day. The same procedure has been wielded for pyridine self-assembled monolayers.

8.2.3 SERS setup

The functionalised gold ring electrodes have been mounted on a spinning axis within a 10 mL electrochemical windowed cell. During the measurements, the axis has been kept spinning at 200 Hz to reduce laser-induced photochemical reaction of the AziRu SAM. The gold ring itself serves as working electrode, coupled with an Ag/AgCl and a platinum electrode as reference and counter respectively. The gold mounting axis is connected to a speed-controlled motor and to the potentiostat.

Raman spectra have been collected by using a LabRAM HR800 system equipped with an Olympus BX41 microscope, a 20x wide aperture and long focus distance lens from Nikon, and a 647 nm Coherent Innova Kr^+ laser line as source. A Peltier-cooled Andor CCD as detector operating at -70 °C and a 180° oriented notch filter complete the setup. All reported spectra have been recorded at room temperature, 1 mW on sample power and spectral resolution of 1 cm^{-1}. A schematic representation of the experimental setup is reported in Figure 45.

For sake of conciseness, all of the buffers used in this work are, if not differently explicated, as follow:

- 10 mM $Na_2B_4O_7$/NaOH 100 mM KCl – pH 10
- 10 mM Na_2HPO_4/NaH_2PO_4,100 mM KCl – pH 7
- 10 mM Na/Acetate, 100 mM KCl – pH 4

and pH accordingly adjusted for intermediate values.

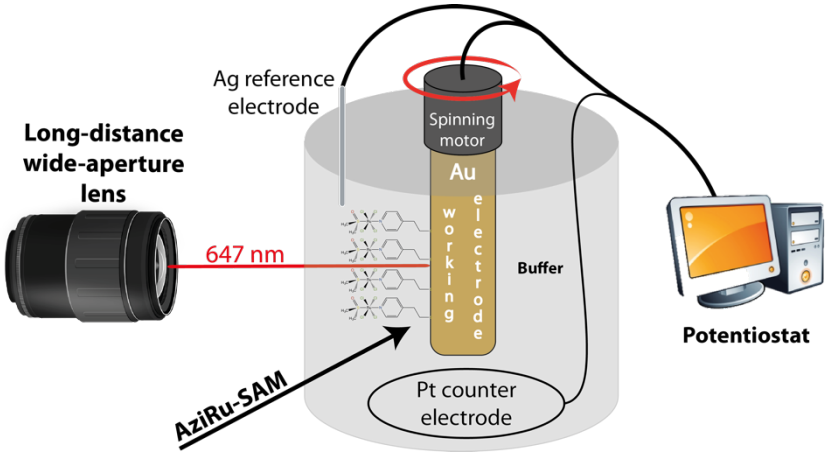

Figure 45 – On-electrode experimental setup scheme. A Teflon windowed chamber contains an AziRu-SAM functionalised gold working electrode in fixed to a spinning motor to avoid laser-induced effects. It is also connected to a potentiostat system for fine-tuning the applied potential. Ag and Pt electrodes are used as reference and counter respectively. The Teflon chamber is filled with buffer solution. The setup requires a 20x long working distance, wide-aperture lens and laser focus is adjusted manually by moving the entire Teflon chamber. Finer adjustments are performed using fine-tuning screws on the chamber mounting frame (not drawn).

8.2.4 Cyclic voltammetry setup

Gold pin working electrodes have been inserted into a glass measuring cell. Again, Ag/AgCl as reference and platinum as counter electrodes. Measured potential have ranged between -0.55 V and +0.60 V with a scanning speed of 50 $mV \cdot s^{-1}$, invariably under protective argon atmosphere.

8.3 Results

Raman references for the vibrations of the Ru complex have been obtained from the comparison between the SERS spectra from the AziRu and pyridine self-assembled monolayers (Figure 46A). The 1000-1700 cm^{-1} region of the AziRu spectrum is entirely due to pyridine (Py from now on) ring modes.

Significant signals from the ruthenium-ligand vibrations are appreciable in the 200-1000 cm^{-1} region, though some Py features superpose.

The identification of Raman markers for the ligand exchange upon water exposure has been achieved by comparing the low frequency regions from the dry AziRu spectrum to the AziRu spectrum collected in the presence of the buffer, a 10 mM sodium phosphate, 100 mM potassium chloride solution at pH 7 (Figure 46B). The comparison marks clear changes in the relative intensity of lower frequency features upon dry to "wet" AziRu transition. The bands from Ru-Cl modes decrease due to the very fast Cl → H_2O/OH^- exchange, according to previous findings[18,297] and consistently with two arising features related to Ru-H_2O/OH in the range 300-500 cm^{-1} and at around 750 cm^{-1} (Figure 46B). Noteworthy that ruthenium-oxygen vibrations are present in the dry spectrum conceivably indicating the ligand exchange to already take place in the 50% v/v ethanol solution used for functionalising the ring electrode. Casting out nines to pinpointedly assign these spectral modifications to Ru-ligands exchange, the dry Py and wet Py spectra have been collected (Figure 47) and the comparison does not show any appreciable difference, thus confirming the exclusive Ru coordination sphere involvement.

These evidences are useful to assume a low content of Ru-Cl in the wet condition (probably only one Cl^- remains coordinated in the time scale of SERS measurements), and consistent with previous observations.[18]

The strong SERS differences between Aziru-SAM and Py-SAM translate into valuable *SERS markers for the Ru-release*. Particularly:

a) the regions at 300-500 and at around 750 cm^{-1} are very different prior and after Ru-release.
b) the relative intensities of the two bands around 1600 and 1200 cm^{-1} are sensitive to the ruthenium release as well.

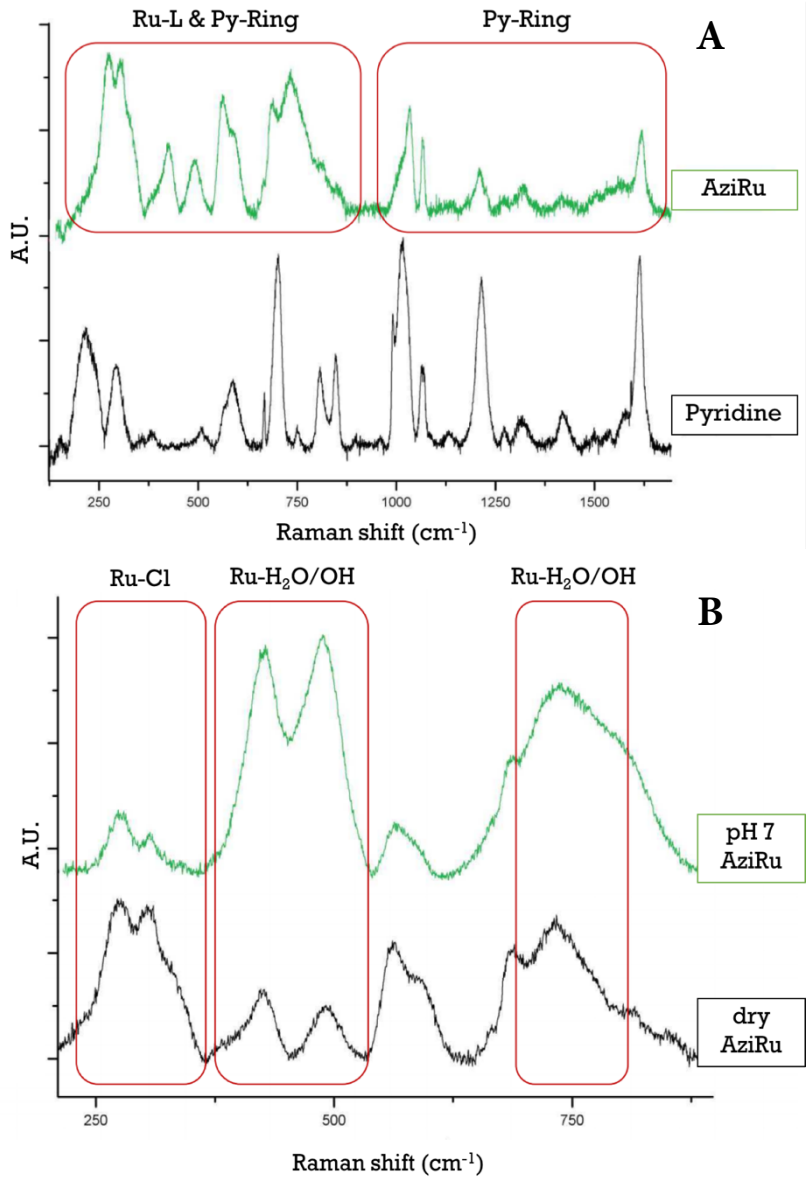

Figure 46 – SERS spectra collected on ring gold electrodes using a 687 cm^{-1} excitation line. **A**) Comparison between dry pyridine and dry AziRu self-assembled monolayers. Spectral differences allow to assign Ru-related vibrational modes as highlighted in red boxes. **B**) Low frequency detail for the comparison between dry AziRu SAM and its "wet" counterpart in a 10 mM Na_2HPO_4, 10 mM NaH_2PO_4, 100 mM KCl solution at pH 7. Relative intensity variations are appreciable, that is, Ru-Cl features fade out and Ru-H2O/OH- bands arise, coherently with a swift ligand exchange.

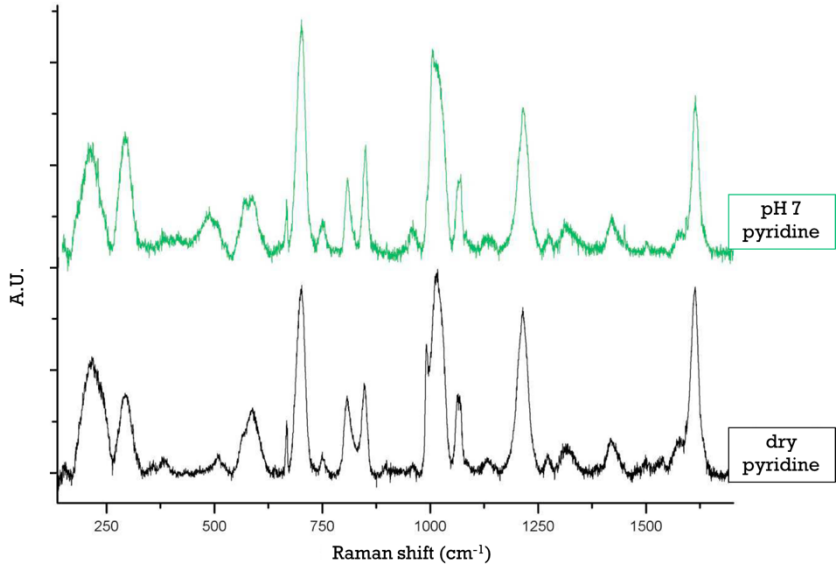

Figure 47 – SERS spectra comparison between dry pyridine SAM and the wet pyridine SAM dipped in a 10 mM Na_2HPO_4, 10 mM NaH_2PO_4, 100 mM KCl solution at pH 7. Spectra collected using a ring gold electrode and 687 nm laser line. Spectral resolution is 1 cm^{-1}.

8.3.1 INVESTIGATING SERS OF AZIRU *VS* PH

Upon aquation, the pH has a pivotal role in defining the electrochemical properties and behaviour of the complex by means of the H_2O/OH^- ligands ratio hence Ru(III)/Ru(II) redox potential and ultimately affecting the promising AziRu selective activation.

A first concern is about whether protonation/deprotonation actually occur and this SERS experimental setup is able to detect them. Thereafter, attempt to determine the pK_A value accordingly.

Given the previously obtained Raman references for the aquation process, SERS spectra of the wet AziRu SAM as a function of pH have been collected at 7 pH values, between 4 and 10 (Figure 48).

The ≥1000 cm^{-1} region (Figure 48A) is utterly unperturbed by pH, whereas the low frequency features significantly vary as pH changes (Figure 48B). Particularly, the relative intensities of the bands in the 400-500 cm^{-1} range, diagnostic for the H_2O/OH^- vibrations, revert as pH arises. The 420 cm^{-1} band prevailing at pH 10, can be assumed

as representative for Ru-OH^- and, accordingly, the 480 cm^{-1} as diagnostic of the Ru-H_2O modes. A minor shift of the band at around 720-740 cm^{-1} is also appreciable.

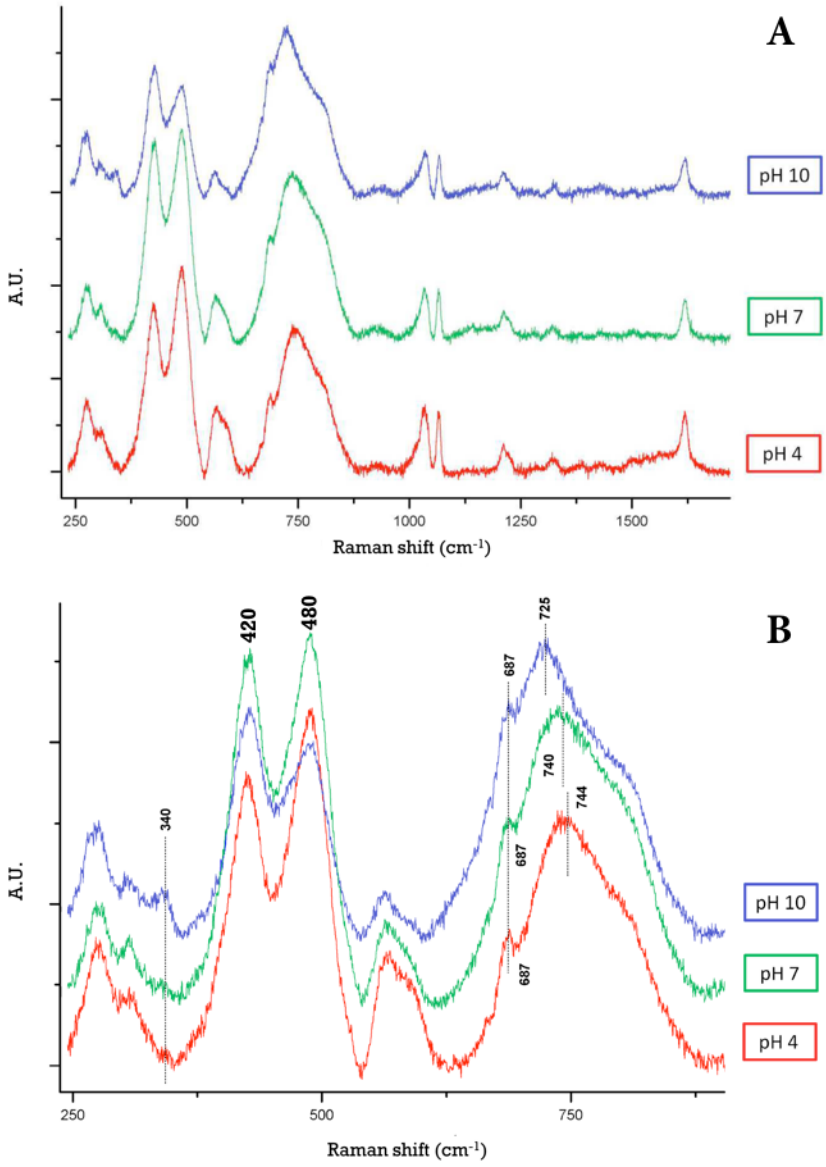

Figure 48 – SERS spectra at different pH for the AziRu SAM. A) The full range spectra point out that no significant modification occurs beyond 1000 cm^{-1}. B) Detail for the low frequency region show a clear inversion in the relative intensities of the 420 and 480 cm^{-1} bands, assumed as representative for Ru-hydroxide and Ru-water respectively.

The SERS spectra have been collected also from the Py SAM at the same pH values as before (Figure 49). The Py SAM spectrum at pH 4 shows a 1640 cm^{-1} shoulder due to the pyridine protonation (ν N-H), absent at pH 7 and 10 either. No additional changes in the low frequency region are detectable thus excluding Py-related effects on the spectral changes seen from the pH-dependent AziRu spectra.

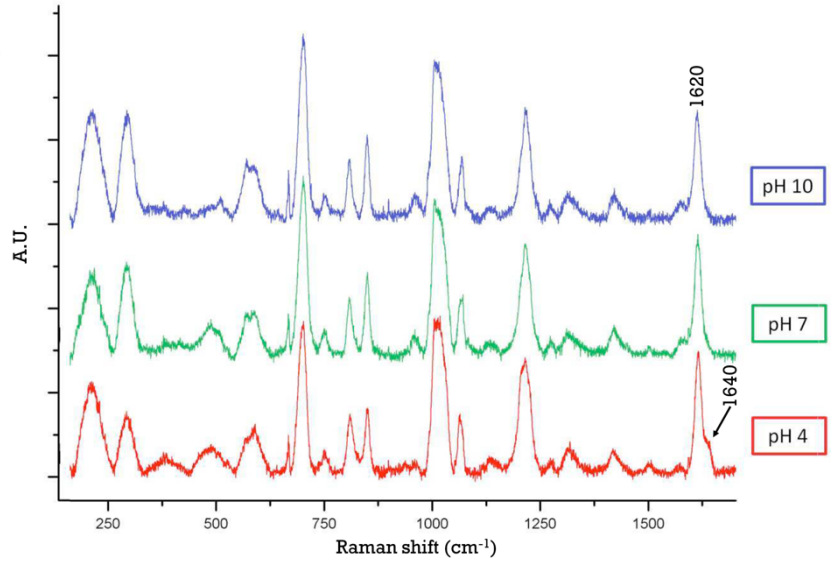

Figure 49 – SERS spectra from the pyridine SAM at pH 4, 7, and 10. A shoulder at 1640 cm^{-1} is appreciable in the pH 4 trace exclusively and it is diagnostic for the Py protonation.

8.3.2 Determining the pK_A

The pH-sensitive SERS features above described are the ground for a tentative extrapolation of the pKa value for the H_2O/OH^- deprotonation in the Ru-coordination sphere. Indeed, a first evaluation of the pKa value can be useful to understand whether it falls within a suitable range for the selective prodrug activation, bearing in mind the substantial difference in pH between healthy and cancerous environments (7.4 down to 6 respectively).[4] This pKa determination has been performed by means of SERS spectra from

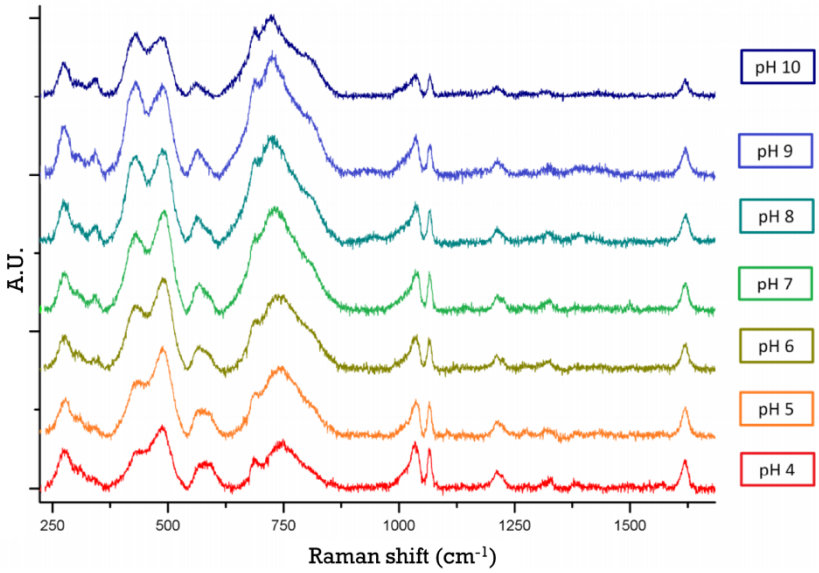

Figure 50 – SERS spectra collected at different pH values in the 4-10 range. All of the spectra have been collected from the same functionalised gold electrode by substituting the buffer solution and waiting 10 minutes for equilibration. Significant spectral changes are appreciable in the low frequency, particularly in the 300-500 cm^{-1} range. By assuming a single deprotonated specie at pH 10, the pKa has been determined (see body text).

the AziRu self-assembled monolayer undergoing to a pH tritation spanning in the pH range 4-10, with 1 pH steps between successive records (Figure 50).

The pKa evaluation herein proposed relies on the assumption that at pH 10 uniquely the protonated form exists since there is almost no difference between spectra collected at pH 9 and 10. Therefore, the pH 10 spectrum has been regarded to be representative for a single Ru-OH^- specie with a molar fraction of 1.

By contrast, the pH 4 spectrum cannot be regarded as representative of a single Ru-H_2O specie since clear differences still occur between pH 4 and 5. A clear plateau is not appreciable, hinting the transition is far from complete and the Ru-H_2O fraction is lower than 1 at pH 4.

A putative pure Ru-H_2O spectrum has been achieved by subtracting the spectrum at pH 10 from the one at pH 4.

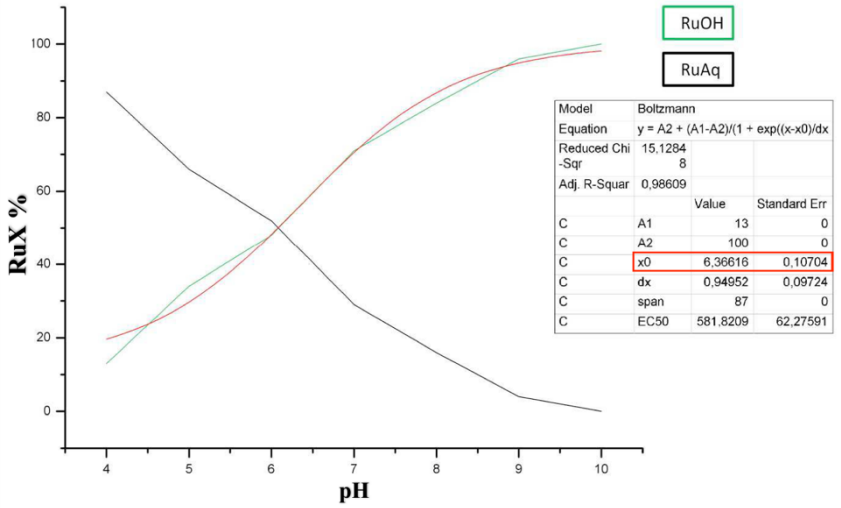

Model	Boltzmann		
Equation	y = A2 + (A1-A2)/(1 + exp((x-x0)/dx		
Reduced Chi-Sqr	15,12848		
Adj. R-Squar	0,98609		
		Value	Standard Err
C	A1	13	0
C	A2	100	0
C	x0	6,36616	0,10704
C	dx	0,94952	0,09724
C	span	87	0
C	EC50	581,8209	62,27591

Figure 51 – Molar fraction as a function of pH for the Ru-OH (RuOH) and the Ru-H_2O species. A sigmoidal trend is appreciable and a Boltzmann fitting performed (fitting table). The pKa value as been determined to be 6.4.

Making it simpler, the pH 4 spectrum is representative for a residual deprotonated fraction of 0.16, hence of a 0.84 fraction of Ru-H_2O. The relative molar fractions for each collected spectrum (from pH 4 to 10) have been extrapolated, plotted (Figure 51) as a function of pH and fitted using the Boltzmann equation.

The pKa value could therefore be evaluated to be 6.4±0.1, a most interesting inference because compatible with the hypothesis that lower pH found in cancerous tissues and cells may crucially contribute to selectively prompt the prodrug activation by favouring the transition to the Ru(II) active specie.[4]

These findings remarks the chance to effectively use AriRu SAM as a SERS pH sensing system, at least in the 5.4-7.4 pH range by using the useful ration between the bands at 420 and around 480 cm^{-1}. Moreover, the SERS could make this possible in-cell as well.

8.3.3 Electro-SERS

Potential-dependent SERS has been used to determine the behaviour of the AziRu at different applied potentials at different

pH conditions. AziRu SAM on a ring gold electrode have been exposed to pH 4, 7 (Figure 52A and B) and 10 (Figure 53) and spectra recorded as a function of controlled applied potential spanning in the -300 mV +500 mV range, by using a potentiostat directly linked to the gold ring, which serves as working electrode. Major changes occur upon applied potential and pH variation either. Significant changes are apparent mostly in the lower frequency region representative for the Ru-ligands modes. The band at around 1620 cm^{-1}, arising from the Py-ring stretching normal modes (C=C)[304,305] is expected to be sensitive towards the Au surface and the ruthenium electron density either and has been first evaluated as diagnostic of the redox process and used for a tentative E_0 evaluation.[305,306]

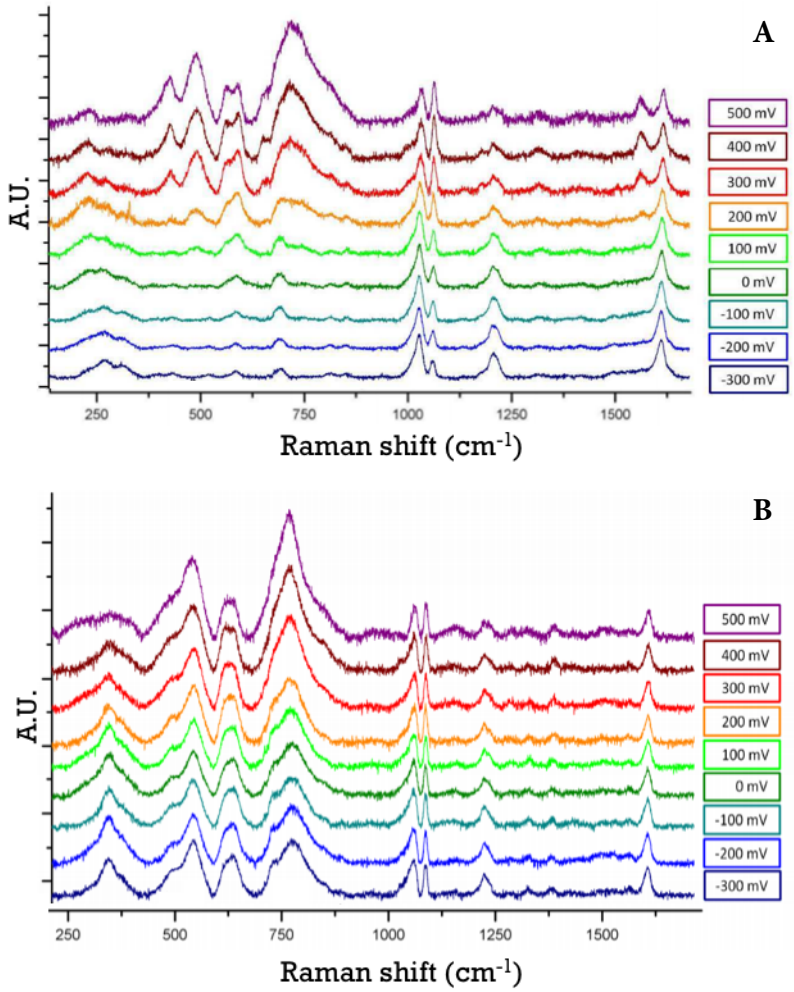

Figure 52 – SERS spectra for the AziRu SAM at A) pH 4 and B) pH 7 at different applied potentials in the -300 mV to +500 mV. A clear trend is apparent at pH 4 for the low frequency region signals arising from the Ru-ligand modes, indicatory for the ruthenium release. Besides, the relative intensity of the Py-related bands at 1060 and 1620 cm-1 changes accordingly. At pH 7 there is not a clear trend remarking the pH dependency.

8.3.3.1 pH 4

The SERS spectra at pH 4 remark noticeably modifications, particularly in the lower frequency region, representative for the Ru-ligands modes. These features decrease in intensity till nearly completely disappearing at approximately -100 mV, whereas the

Py-related bands stand (Figure 52), indicating Ru release. The Py ring breathing band at around 1020 cm^{-1} stays completely unperturbed but the Py-ring trigonal breathing,[304,305] around 1060 cm^{-1} decreases. The Py-ring C=C stretching band at around 1620 cm^{-1} shifts as the potential becomes more negative (Figure 52) and has been used to evaluate putative E_0 by assuming the system to be completely oxidised at +500 mV and completely reduced at -300 mV, using the same approach as seen for the pKa. At pH 4 the E_0 extrapolated from SERS spectra is +28±7 mV.

Worth to say, this SERS-based redox titration is definitively less accurate than the previously reported SERS-based pH-titration, and alternative route for evaluating the E_0 evaluation has been adopted (see below). It has therefore not to be considered as a reliable SERS-based redox sensing system.

The very sharp trend observed for the lower frequency region features from the Ru-ligands can possibly relate to the release of the ruthenium from the pyridine upon reduction. The behaviour in this region is completely different both at pH 7 and pH 10, potentially supporting the opening hypothesis, though further proofs are needed.

8.3.3.2 pH 7 and pH 10

Looking at the SERS spectra sequence a pH 7 the AziRu behaviour is sensibly different. The mighty drops in intensity in the low frequency region are not appreciable but for a slight reduction of the feature at around 750 cm^{-1}. As well, the relative intensities of the Py-ring breathing modes do not appear perturbed by the applied potential all over its full extent. The C=C Py-ring band at around 1620 cm^{-1} shifts less pronouncedly than seen at pH 4 and the resulting fitting model is affected by a larger bias, giving an E_0 value of 208±20 mV.

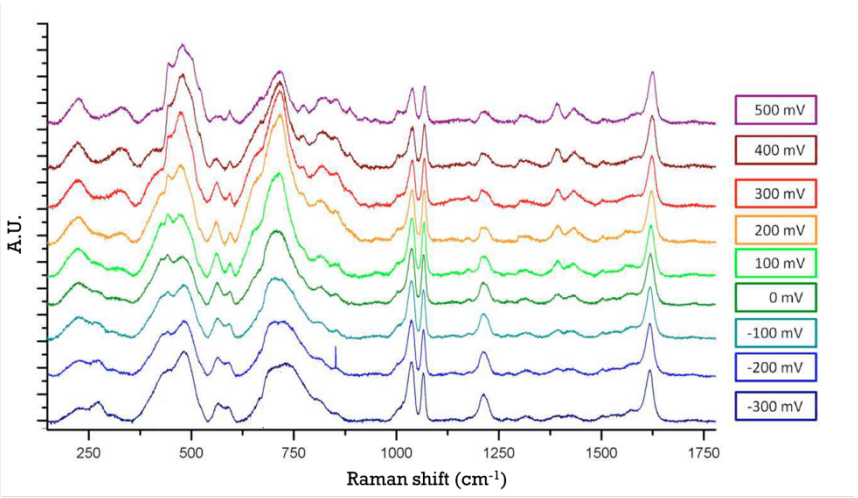

Figure 53 – SERS spectra for the AziRu SAM at pH 10. The lower frequency bands exhibit a similar behaviour as compared to pH though new, yet unidentified species, appear.

Similarly, at pH 10 the bands in the lower frequency have a similar behaviour as at pH 7 though, even though some new species conceivably appear. In this case, the estimated E_0 value is 103±5 mV.

Though clear pH- and potential-dependent SERS spectral features have been identified, the found E_0 values yet glares curbs and a deeper investigation has been performed by means of cyclic voltammetry.

8.3.4 Cyclic voltammetry

Cyclic voltammetry has been performed on the same system adopted in the Raman-based evaluation of standard reduction potentials, but for the usage of pin gold electrode in place of ring ones. Resulting voltammograms are reported in (Figure 54), and a clear dependence towards pH is apparent.

The pH 10 voltammogram shows a different course over the number of cycles as compared to pH 7 and 4 (Figure 54). Some features clearly visible in early runs fade out and new signals arise.

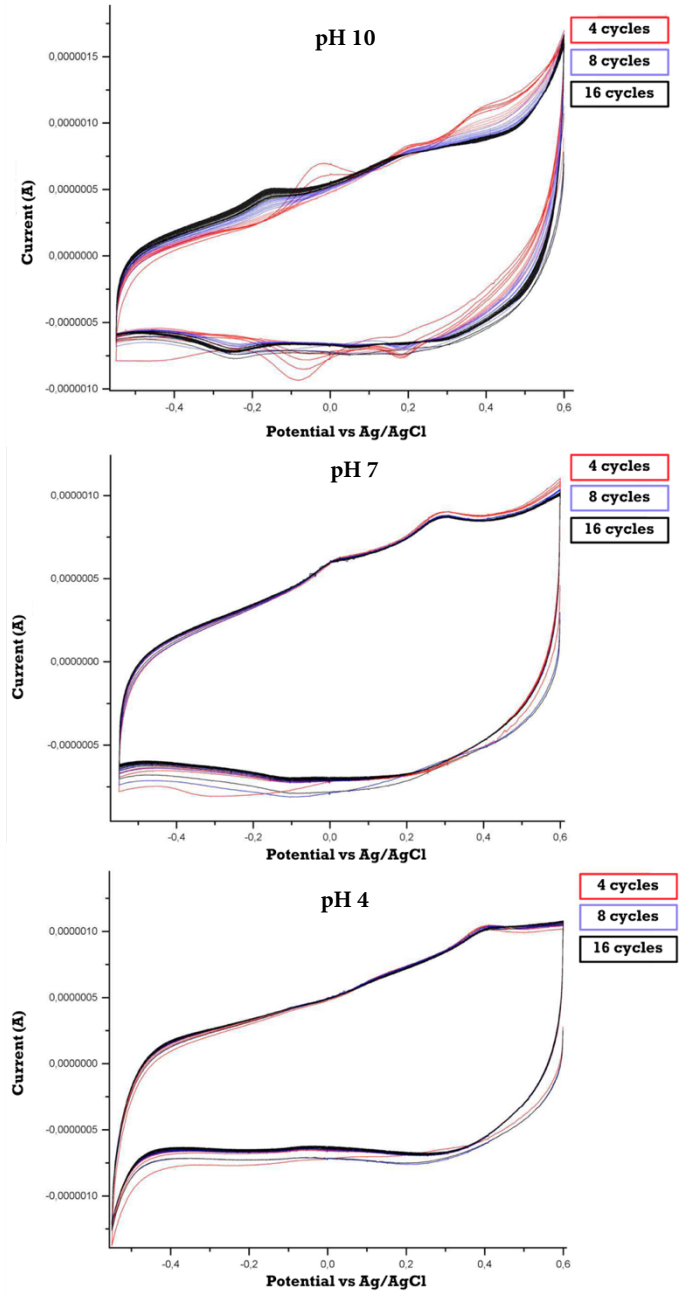

Figure 54 – Cyclic voltammograms at the three different pH values of the AziRu SAM vs Ag/AgCl on a pin gold electrode. At pH 10 the system is probably far from an equilibrium condition.

This can possibly be explained by the electrically-driven formation of unstable species rapidly changing in new, stable species, also

making plain the stabilisation as the number of cycles goes. Alternatively, the system may be far from the equilibrium during early stages though the previous SERS findings hardly fit. Moreover, even much longer equilibration times prior the cyclo-voltammetric measures have given almost identical results.

The voltammograms have a very broad appearance which may be clarified as the addition of multiple different species possibly possessing very close E_0 values, but further investigations are required.

The voltammetric evaluation of the E_0 for each pH has been hence brought off according to:

$$E_0 = \frac{E_{ox} + E_{red}}{2}$$

where E_{ox} and E_{red} are the standard oxidation and reduction potentials respectively. As compared to those obtained from SERS, the cyclic voltammetry gave a much clearer trend. As the pH moves down, the corresponding standard E_0 values moves from -200 mV at pH 10, to -50 mV at pH 7 and -34 mV at pH 4 finally.

The aggregate of the pKa (6.4±0.1) and the E_0 findings, gives an encouraging frame for the easier reduction, thus activation of the AziRu prodrug within cancer entities, bearing in mind the comparatively lower pH and higher reducing environment of tumours as compared to healthy tissues.

8.4 Conclusions

AziRu is among the most promising prodrug from the ruthenium family because of its stunning anti-proliferative, anti-metastatic, and likely selectivity properties. The keystone hypothesis underlying the selective activation of the prodrug harks back to whether the reduction of the ruthenium within cancerous lesions could occur easier than in physiological counterparts, because of lower pH and sensibly higher reducing potential of cancerous conditions. This section addresses this question by giving insights on the influence pH exerts on the standard reduction potential of the complex, through the interesting SERS on electrode approach. Further support to the previous Ru-ligands assignment is provided and an evaluation of the pKa is reported.

Briefly, this chapter brought two significant inferences:

I. Provides the pKa and E_0 values as a function of pH for the AziRu SAM.
II. Proves the sensitiveness of the SERS valuable for developing diagnostic systems for the pH and the ruthenium release either, possibly transposable to in-cell applications. Regrettably, the system cannot be assumed reliable for the Ru-detection as yet.

The most interesting pKa value of 6.4±0.1 falls in a watershed range of pH values separating most cancer environments from their physiological counterparts. Standard reduction potentials have been thereafter evaluated as a function of pH by means of electro-SERS and cyclic voltammetry either. Though the outcomes from electro-SERS have not been as clear as cyclic voltammetry, E_0 values could be evaluated showing a meaningful trend with regard to the pH. The whole of these findings further proves the chance for a selectively easier, potential-driven and pH-dependent activation

of the ruthenium prodrug within cancer. Further theoretical DFT and Levers' analyses[307] are being brought off by dr. Kozuch and prof. Hildebrandt's team, preliminarily supporting these findings. Looking forward, SERS analyses should be extended further acid since the pKa sigmoidal plateau is not entirely shaped at pH 4. By now, this has been denied by limitations in the electrochemical cell used. At last, UV/Vis electrospectroscopy could profitably integrate SERS findings.

9

Bottom line

This project dealt with the improvement of the relatively young yet powerful Raman-assisted crystallography (RAC) approach, a most convenient combination of mutual complementary techniques for looking deep into the bountifully informative macromolecular crystalline systems. RAC was applied to explore a number of most diverse systems exploiting metal-protein interaction as a common thread subject.

Each foregoing section extensively accounts for system-specific inferences whereas a comprehensive discussion over the general forewords of this thesis follows.

Raman assistance turns useful as a supportive tool for a bounty of goals and was effectively exploited as a supportive analytical tool for assessing primary structure (ligands insertion in Chapter 2, photodamage events in Chapter 3) and secondary structure ($\alpha \rightarrow \beta$ transition in Chapter 2) chemical modifications occurring within protein crystals.

Beyond the purely compositional information and in a stricter sense of the words, RAC was fruitfully adopted to overcome crystallographic curbs in terms of supportive or complementary data for the electron-density disambiguation (Chapters 5-7), to proper clarify ligand binding-mode (Chapter 5), metal coordination sphere (Chapters 6 and 7) and redox behaviour (Chapter 7). In addition, *in-cristallo* Surface-Enhanced Raman Spectroscopy (SERS) provided inspiring information for a proper crystallographic structural evaluation of a protein-nanoparticle hybrid system (Chapter 3), while off-crystal, on-electrode SERS emerged into a fine setup for the investigation of key physico-chemical properties of a novel ruthenium prodrug (Chapter 8).

Altogether, this thesis proved the RAC effectiveness and reliability in a swollen range of diverse protein-metal systems and hints to overturn the RAC perspective as crystallography provided valuable support for Raman assignments, in a *Crystallography-assisted Raman spectroscopy* (CAR) outlook, as led out in Chapter 3 where ultrahigh resolution X-ray data was the spearhead for satisfactory Raman markers identification, and in Chapter 5 where Raman and crystallography came to mutual assistance *iteratively*.

10

References

1. Farrer, N.J. and Sadler, P.J., *Medicinal Inorganic Chemistry: State of the Art, New Trends, and a Vision of the Future, in Bioinorganic Medicinal Chemistry*. Vol. 1. 2011, Weinheim - Germani: Wiley-VCH Verlag GmbH & Co.
2. *Martindale: The Complete Drug Reference Brayfield Alison (Ed) Martindale: The Complete Drug Reference pound459 4,688pp Pharmaceutical Press 9780857111395 0857111396 [Formula: see text]*. Emerg Nurse, 2014. **22**(5): p. 12.
3. Gaynor, D. and Griffith, D.M., *The prevalence of metal-based drugs as therapeutic or diagnostic agents: beyond platinum*. Dalton T, 2012. **41**(43): p. 13239-13257.
4. Reisner, E., Arion, V.B., et al., *Electron-transfer activated metal-based anticancer drugs*. Inorg Chim Acta, 2008. **361**(6): p. 1569-1583.
5. Dwyer, F.P., Mayhew, E., et al., *Inhibition of Landschuetz Ascites Tumour Growth by Metal Chelates Derived from 3,4,7,8-Tetramethyl-1,10-Phenanthroline*. Br J Cancer, 1965. **19**: p. 195-199.
6. Dwyer, F.P., Gyarfas, E.C., et al., *Biological activity of complex ions*. Nature, 1952. **170**(4318): p. 190-191.
7. Dwyer, F.P., Reid, I.K., et al., *The biological actions of 1,10-phenanthroline and 2,2'-bipyridine hydrochlorides, quaternary salts and metal chelates and related compounds. 1. Bacteriostatic action on selected gram-positive, gram-negative and acid-fast bacteria*. Aust J Exp Biol Med Sci, 1969. **47**(2): p. 203-218.
8. Rosenberg, B., VanCamp, L., et al., *Platinum compounds: a new class of potent antitumour agents*. Nature, 1969. **222**(5191): p. 385-386.
9. Wheate, N.J., Walker, S., et al., *The status of platinum anticancer drugs in the clinic and in clinical trials*. Dalton Trans, 2010. **39**(35): p. 8113-8127.
10. Kelland, L., *The resurgence of platinum-based cancer chemotherapy*. Nat Rev Cancer, 2007. **7**(8): p. 573-584.
11. McQuitty, R.J., *Metal-based drugs*. Sci Prog, 2014. **97**(Pt 1): p. 1-19.

12. Wang, D. and Lippard, S.J., *Cellular processing of platinum anticancer drugs.* Nat Rev Drug Discov, 2005. **4**(4): p. 307-320.
13. Ishida, S., Lee, J., et al., *Uptake of the anticancer drug cisplatin mediated by the copper transporter Ctr1 in yeast and mammals.* Proc Natl Acad Sci U S A, 2002. **99**(22): p. 14298-14302.
14. Chen, H.H. and Kuo, M.T., *Overcoming platinum drug resistance with copper-lowering agents.* Anticancer Res, 2013. **33**(10): p. 4157-4161.
15. Medici, S., Peana, M., et al., *Noble metals in medicine: Latest advances.* Coordin Chem Rev, 2015. **284**: p. 329-350.
16. Merlino, A., *Interactions between proteins and Ru compounds of medicinal interest: A structural perspective.* Coordin Chem Rev, 2016. **326**: p. 111-134.
17. Messori, L. and Merlino, A., *Ruthenium metalation of proteins: the X-ray structure of the complex formed between NAMI-A and hen egg white lysozyme.* Dalton Trans, 2014. **43**(16): p. 6128-6131.
18. Vergara, A., Russo Krauss, I., et al., *Investigating the ruthenium metalation of proteins: X-ray structure and Raman microspectroscopy of the complex between RNase A and AziRu.* Inorg Chem, 2013. **52**(19): p. 10714-10716.
19. Arnesano, F. and Natile, G., *Mechanistic insight into the cellular uptake and processing of cisplatin 30 years after its approval by FDA.* Coordin Chem Rev, 2009. **253**(15-16): p. 2070-2081.
20. Kelsen, D.P., Scher, H., and Burchenal, J., *Phase I and Early Phase II Trials of 4'Carboxyphthalato (1,2 Diaminocyclohexane) Platinum (II)*, in *Platinum Coordination Complexes in Cancer Chemotherapy: Proceedings of the Fourth International Symposium on Platinum Coordination Complexes in Cancer Chemotherapy convened in Burlington, Vermont by the Vermont Regional Cancer Center and the Norris Cotton Cancer Center, June 22–24, 1983*, M.P. Hacker, E.B. Douple, and I.H. Krakoff, Editors. 1984, Springer US: Boston, MA. p. 310-320.
21. Cvitkovic, E. and Bekradda, M., *Oxaliplatin: a new therapeutic option in colorectal cancer.* Semin Oncol, 1999. **26**(6): p. 647-662.
22. Fuertes, M.A., Alonso, C., and Perez, J.M., *Biochemical modulation of cisplatin mechanisms of action: Enhancement of antitumor activity and circumvention of drug resistance.* Chemical Reviews, 2003. **103**(3): p. 645-662.
23. Hartinger, C.G., Zorbas-Seifried, S., et al., *From bench to bedside - preclinical and early clinical development of the anticancer agent indazolium trans-[tetrachlorobis(1H-indazole)ruthenate(III)] (KP1019 or FFC14A).* J Inorg Biochem, 2006. **100**(5-6): p. 891-904.
24. Hartinger, C.G., Jakupec, M.A., et al., *KP1019, a new redox-active anticancer agent--preclinical development and results of a clinical phase I study in tumor patients.* Chem Biodivers, 2008. **5**(10): p. 2140-2155.
25. Markowska, A., Kasprzak, B., et al., *Noble metals in oncology.* Contemp Oncol (Pozn), 2015. **19**(4): p. 271-275.
26. Clarke, M.J., Zhu, F.C., and Frasca, D.R., *Non-platinum chemotherapeutic metallopharmaceuticals.* Chemical Reviews, 1999. **99**(9): p. 2511-2533.
27. Dahm, G., Bailly, C., et al., *Synthesis, structural characterization and in vitro anti-cancer activity of functionalized N-heterocyclic carbene platinum and palladium complexes.* J Organomet Chem, 2015. **794**: p. 115-124.
28. Jahromi, E.Z., Divsalar, A., et al., *Palladium complexes: new candidates for anti-cancer drugs.* J Iran Chem Soc, 2016. **13**(5): p. 967-989.
29. Finkelstein, A.E., Walz, D.T., et al., *Auranofin. New oral gold compound for treatment of rheumatoid arthritis.* Ann Rheum Dis, 1976. **35**(3): p. 251-257.
30. van Rijt, S.H. and Sadler, P.J., *Current applications and future potential for bioinorganic chemistry in the development of anticancer drugs.* Drug Discov Today, 2009. **14**(23-24): p. 1089-1097.
31. Nardon, C., Boscutti, G., and Fregona, D., *Beyond Platinums: Gold Complexes as Anticancer Agents.* Anticancer Research, 2014. **34**(1b): p. 487-492.
32. Leung, C.-H., Zhong, H.-J., et al., *Bioactive iridium and rhodium complexes as therapeutic agents.* Coordin Chem Rev, 2013. **257**(11–12): p. 1764-1776.
33. Li, C., Yu, M., et al., *A nonemissive iridium(III) complex that specifically lights-up the nuclei of living cells.* J Am Chem Soc, 2011. **133**(29): p. 11231-11239.

34. Jia, J., Fei, H., and Zhou, M., *Luminescent iridium(III) complexes as novel protein staining agents.* Electrophoresis, 2012. **33**(9-10): p. 1397-1401.
35. Jiang, J., Zhang, C., et al., *Long-lived phosphorescent iridium(III) complexes conjugated with cationic polyfluorenes for heparin sensing and cellular imaging.* Macromol Rapid Commun, 2015. **36**(7): p. 640-646.
36. Koren, K., Dmitriev, R.I., et al., *Complexes of Ir(III)-octaethylporphyrin with peptides as probes for sensing cellular O2.* Chembiochem, 2012. **13**(8): p. 1184-1190.
37. Ma, D.L., Zhong, H.J., et al., *Phosphorescent imaging of living cells using a cyclometalated iridium (III) complex.* PLoS One, 2013. **8**(2): p. e55751.
38. Wang, B., Liang, Y., et al., *A luminescent cyclometalated iridium(III) complex accumulates in mitochondria and induces mitochondrial shortening by conjugation to specific protein targets.* Chembiochem, 2012. **13**(18): p. 2729-2737.
39. Zeng, Y., Liu, Y., et al., *Phosphorescence monitoring of hypoxic microenvironment in solid-tumors to evaluate chemotherapeutic effects using the hypoxia-sensitive iridium (III) coordination compound.* PLoS One, 2015. **10**(3): p. e0121293.
40. Wang, X., Jia, J., et al., *Luminescent peptide labeling based on a histidine-binding iridium(III) complex for cell penetration and intracellular targeting studies.* Chemistry, 2011. **17**(29): p. 8028-8032.
41. Desmard, M., Davidge, K.S., et al., *A carbon monoxide-releasing molecule (CORM-3) exerts bactericidal activity against Pseudomonas aeruginosa and improves survival in an animal model of bacteraemia.* FASEB J, 2009. **23**(4): p. 1023-1031.
42. Ward, J.S., Lynam, J.M., et al., *A therapeutically viable photo-activated manganese-based CO-releasing molecule (photo-CO-RM).* Dalton Trans, 2012. **41**(35): p. 10514-10517.
43. Bikiel, D.E., Gonzalez Solveyra, E., et al., *Tetrachlorocarbonyliridates: water-soluble carbon monoxide releasing molecules rate-modulated by the sixth ligand.* Inorg Chem, 2011. **50**(6): p. 2334-2345.
44. Simpson, P.V., Radacki, K., et al., *An iridium N-heterocyclic carbene complex [IrCl(CO)2(NHC)] as a carbon monoxide-releasing molecule (CORM).* J Organomet Chem, 2015. **782**: p. 116-123.
45. Motterlini, R. and Otterbein, L.E., *The therapeutic potential of carbon monoxide.* Nat Rev Drug Discov, 2010. **9**(9): p. 728-743.
46. Motterlini, R., Clark, J.E., et al., *Carbon monoxide-releasing molecules: characterization of biochemical and vascular activities.* Circ Res, 2002. **90**(2): p. E17-24.
47. Desmard, M., Foresti, R., et al., *Differential antibacterial activity against Pseudomonas aeruginosa by carbon monoxide-releasing molecules.* Antioxid Redox Signal, 2012. **16**(2): p. 153-163.
48. Romanski, S., Kraus, B., et al., *Acyloxybutadiene tricarbonyl iron complexes as enzyme-triggered CO-releasing molecules (ET-CORMs): a structure-activity relationship study.* Dalton Trans, 2012. **41**(45): p. 13862-13875.
49. Romanski, S., Kraus, B., et al., *Acyloxybutadiene iron tricarbonyl complexes as enzyme-triggered CO-releasing molecules (ET-CORMs).* Angew Chem Int Ed Engl, 2011. **50**(10): p. 2392-2396.
50. Tinajero-Trejo, M., Rana, N., et al., *Antimicrobial Activity of the Manganese Photoactivated Carbon Monoxide-Releasing Molecule [Mn(CO)3(tpa-kappa(3)N)](+) Against a Pathogenic Escherichia coli that Causes Urinary Infections.* Antioxid Redox Signal, 2016. **24**(14): p. 765-780.
51. Jimenez, J., Chakraborty, I., et al., *Light-triggered CO delivery by a water-soluble and biocompatible manganese photoCORM.* Dalton Trans, 2016. **45**(33): p. 13204-13213.
52. Garcia-Gallego, S. and Bernardes, G.J., *Carbon-monoxide-releasing molecules for the delivery of therapeutic CO in vivo.* Angew Chem Int Ed Engl, 2014. **53**(37): p. 9712-9721.
53. Seixas, J.D., Mukhopadhyay, A., et al., *Characterization of a versatile organometallic pro-drug (CORM) for experimental CO based therapeutics.* Dalton Trans, 2013. **42**(17): p. 5985-5998.
54. Santos-Silva, T., Mukhopadhyay, A., et al., *CORM-3 reactivity toward proteins: the crystal structure of a Ru(II) dicarbonyl-lysozyme complex.* J Am Chem Soc, 2011. **133**(5): p. 1192-1195.
55. Petruk, A.A., Vergara, A., et al., *Interaction between Proteins and Ir Based CO Releasing Molecules: Mechanism of Adduct Formation and CO Release.* Inorganic Chemistry, 2014. **53**(19): p. 10456-10462.

56. Santos, M.F.A., Seixas, J.D., et al., *New insights into the chemistry of fac-[Ru(CO)3]2 + fragments in biologically relevant conditions: The CO releasing activity of [Ru(CO)3Cl2(1,3-thiazole)], and the X-ray crystal structure of its adduct with lysozyme.* J Inorg Biochem, 2012. **117**: p. 285-291.
57. Caterino, M., Petruk, A.A., et al., *Mapping the protein-binding sites for iridium(iii)-based CO-releasing molecules.* Dalton Trans, 2016. **45**(30): p. 12206-12214.
58. Levina, A., Mitra, A., and Lay, P.A., *Recent developments in ruthenium anticancer drugs.* Metallomics, 2009. **1**(6): p. 458-470.
59. Alessio, E., Mestroni, G., et al., *Ruthenium antimetastatic agents.* Curr Top Med Chem, 2004. **4**(15): p. 1525-1535.
60. Bergamo, A. and Sava, G., *Ruthenium anticancer compounds: myths and realities of the emerging metal-based drugs.* Dalton Trans, 2011. **40**(31): p. 7817-7823.
61. Clarke, M.J., *Toward ruthenium containing metallopharmaceuticals.* Abstr Pap Am Chem S, 2005. **230**: p. U2131-U2131.
62. Suss-Fink, G., *Arene ruthenium complexes as anticancer agents.* Dalton T, 2010. **39**(7): p. 1673-1688.
63. Bacac, M., Hotze, A.C., et al., *The hydrolysis of the anti-cancer ruthenium complex NAMI-A affects its DNA binding and antimetastatic activity: an NMR evaluation.* J Inorg Biochem, 2004. **98**(2): p. 402-412.
64. Dragutan, I., Dragutan, V., and Demonceau, A., *Editorial of Special Issue Ruthenium Complex: The Expanding Chemistry of the Ruthenium Complexes.* Molecules, 2015. **20**(9): p. 17244-17274.
65. Bergamo, A. and Sava, G., *Linking the future of anticancer metal-complexes to the therapy of tumour metastases.* Chem Soc Rev, 2015. **44**(24): p. 8818-8835.
66. Bergamo, A. and Sava, G., *Ruthenium complexes can target determinants of tumour malignancy.* Dalton Trans, 2007(13): p. 1267-1272.
67. Bratsos, I., Bergamo, A., et al., *Influence of the anionic ligands on the anticancer activity of Ru(II)-dmso complexes: Kinetics of aquation and in vitro cytotoxicity of new dicarboxylate compounds in comparison with their chloride precursors.* J Inorg Biochem, 2008. **102**(4): p. 606-617.
68. Gava, B., Zorzet, S., et al., *Inhibition of B16 melanoma metastases with the ruthenium complex imidazolium trans-imidazoledimethylsulfoxide-tetrachlororuthenate and down-regulation of tumor cell invasion.* J Pharmacol Exp Ther, 2006. **317**(1): p. 284-291.
69. Sava, G., Frausin, F., et al., *Actin-dependent tumour cell adhesion after short-term exposure to the antimetastasis ruthenium complex NAMI-A.* Eur J Cancer, 2004. **40**(9): p. 1383-1396.
70. Casarsa, C., Mischis, M.T., and Sava, G., *TGFbeta1 regulation and collagen-release-independent connective tissue re-modelling by the ruthenium complex NAMI-A in solid tumours.* J Inorg Biochem, 2004. **98**(10): p. 1648-1654.
71. Sava, G., Zorzet, S., et al., *Dual Action of NAMI-A in inhibition of solid tumor metastasis: selective targeting of metastatic cells and binding to collagen.* Clin Cancer Res, 2003. **9**(5): p. 1898-1905.
72. Spreckelmeyer, S., Orvig, C., and Casini, A., *Cellular transport mechanisms of cytotoxic metallodrugs: an overview beyond cisplatin.* Molecules, 2014. **19**(10): p. 15584-15610.
73. Adhireksan, Z., Davey, G.E., et al., *Ligand substitutions between ruthenium-cymene compounds can control protein versus DNA targeting and anticancer activity.* Nat Commun, 2014. **5**: p. 3462.
74. Kapitza, S., Pongratz, M., et al., *Heterocyclic complexes of ruthenium(III) induce apoptosis in colorectal carcinoma cells.* J Cancer Res Clin Oncol, 2005. **131**(2): p. 101-110.
75. Blunden, B.M., Rawal, A., et al., *Superior Chemotherapeutic Benefits from the Ruthenium-Based Anti-Metastatic Drug NAMI-A through Conjugation to Polymeric Micelles.* Macromolecules, 2014. **47**(5): p. 1646-1655.
76. Bergamo, A., Riedel, T., et al., *Preclinical combination therapy of the investigational drug NAMI-A(+) with doxorubicin for mammary cancer.* Invest New Drugs, 2015. **33**(1): p. 53-63.
77. Flocke, L.S., Trondl, R., et al., *Molecular mode of action of NKP-1339 - a clinically investigated ruthenium-based drug - involves ER- and ROS-related effects in colon carcinoma cell lines.* Invest New Drugs, 2016. **34**(3): p. 261-268.
78. Nazarov, A.A., Gardini, D., et al., *Organometallic anticancer agents that interfere with cellular energy processes: a subtle approach to inducing cancer cell death.* Dalton Trans, 2013. **42**(7): p. 2347-2350.

79. Guidi, F., Modesti, A., et al., *The molecular mechanisms of antimetastatic ruthenium compounds explored through DIGE proteomics.* J Inorg Biochem, 2013. **118**: p. 94-99.
80. Takezawa, Y., Bockmann, P., et al., *Incorporation of organometallic Ru complexes into apo-ferritin cage.* Dalton T, 2011. **40**(10): p. 2190-2195.
81. Schluga, P., Hartinger, C.G., et al., *Redox behavior of tumor-inhibiting ruthenium(III) complexes and effects of physiological reductants on their binding to GMP.* Dalton T, 2006(14): p. 1796-1802.
82. Graf, N. and Lippard, S.J., *Redox activation of metal-based prodrugs as a strategy for drug delivery.* Adv Drug Deliv Rev, 2012. **64**(11): p. 993-1004.
83. Jakupec, M.A., Reisner, E., et al., *Redox-active antineoplastic ruthenium complexes with indazole: correlation of in vitro potency and reduction potential.* J Med Chem, 2005. **48**(8): p. 2831-2837.
84. Ang, W.H. and Dyson, P.J., *Classical and non-classical ruthenium-based anticancer drugs: Towards targeted chemotherapy.* Eur J Inorg Chem, 2006(20): p. 4003-4018.
85. Antonarakis, E.S. and Emadi, A., *Ruthenium-based chemotherapeutics: are they ready for prime time?* Cancer Chemother Pharmacol, 2010. **66**(1): p. 1-9.
86. Chatterjee, D., Mitra, A., and De, G.S., *Ruthenium Polyaminocarboxylate Complexes PROSPECTS FOR THEIR USE AS METALLOPHARMACEUTICALS.* Platin Met Rev, 2006. **50**(1): p. 2-11.
87. Sanchez-Cano, C. and Hannon, M.J., *Novel and emerging approaches for the delivery of metallo-drugs.* Dalton Trans, 2009(48): p. 10702-10711.
88. Muckerman, J.T., Polyansky, D.E., et al., *New water oxidation chemistry of ruthenium complexes with polypyridyl ligands.* Abstr Pap Am Chem S, 2014. **248**.
89. Vos, J.G. and Kelly, J.M., *Ruthenium polypyridyl chemistry; from basic research to applications and back again.* Dalton T, 2006(41): p. 4869-4883.
90. Aird, R.E., Cummings, J., et al., *In vitro and in vivo activity and cross resistance profiles of novel ruthenium (II) organometallic arene complexes in human ovarian cancer.* Brit J Cancer, 2002. **86**(10): p. 1652-1657.
91. Ang, W.H., Casini, A., et al., *Organometallic ruthenium-based antitumor compounds with novel modes of action.* J Organomet Chem, 2011. **696**(5): p. 989-998.
92. Theruvakkattil, S. and Thalappil, P., *Noble Metal Nanopartices*, in *Springer Handbook of Nanomaterials*, R. Vajtai, Editor. 2013, Springer. p. 303-388.
93. Jain, P.K., Huang, X., et al., *Noble metals on the nanoscale: optical and photothermal properties and some applications in imaging, sensing, biology, and medicine.* Acc Chem Res, 2008. **41**(12): p. 1578-1586.
94. Willets, K.A. and Van Duyne, R.P., *Localized surface plasmon resonance spectroscopy and sensing.* Annu Rev Phys Chem, 2007. **58**: p. 267-297.
95. Aliaga, A.E., Aguayo, T., et al., *Surface-enhanced Raman scattering and theoretical studies of the C-terminal peptide of the beta-subunit human chorionic gonadotropin without linked carbohydrates.* Biopolymers, 2011. **95**(2): p. 135-143.
96. Zhang, L., Fang, Y., and Wang, P., *Experimental and DFT theoretical studies of surface enhanced Raman scattering effect on the silver nano arrays modified electrode.* Spectrochim Acta A Mol Biomol Spectrosc, 2012. **93**: p. 363-366.
97. Fleischmann, M., Hendra, P.J., and McQuillan, A., *Raman spectra of pyridine adsorbed at a silver electrode.* Chemical Physics Letters, 1974. **26**(2): p. 163-166.
98. Daniel, M.C. and Astruc, D., *Gold nanoparticles: assembly, supramolecular chemistry, quantum-size-related properties, and applications toward biology, catalysis, and nanotechnology.* Chem Rev, 2004. **104**(1): p. 293-346.
99. Sajanlal, P.R. and Pradeep, T., *Electric field assisted growth of highly surface enhanced Raman active gold nanotriangles.* J Nanosci Nanotechnol, 2009. **9**(9): p. 5283-5287.
100. Sperling, R.A., Rivera Gil, P., et al., *Biological applications of gold nanoparticles.* Chem Soc Rev, 2008. **37**(9): p. 1896-1908.
101. Shah, M., Badwaik, V.D., and Dakshinamurthy, R., *Biological applications of gold nanoparticles.* J Nanosci Nanotechnol, 2014. **14**(1): p. 344-362.
102. Wang, H., Huff, T.B., et al., *In vitro and in vivo two-photon luminescence imaging of single gold nanorods.* Proc Natl Acad Sci U S A, 2005. **102**(44): p. 15752-15756.
103. Wang, S., Xi, W., et al., *Three-photon luminescence of gold nanorods and its applications for high contrast tissue and deep in vivo brain imaging.* Theranostics, 2015. **5**(3): p. 251-266.

104. Durr, N.J., Larson, T., et al., *Two-photon luminescence imaging of cancer cells using molecularly targeted gold nanorods.* Nano Lett, 2007. **7**(4): p. 941-945.
105. Liu, Z., Zhao, F., et al., *The Applications of Gold Nanoparticle-Initialed Chemiluminescence in Biomedical Detection.* Nanoscale Res Lett, 2016. **11**(1): p. 460.
106. Skrabalak, S.E., Chen, J., et al., *Gold nanocages: synthesis, properties, and applications.* Acc Chem Res, 2008. **41**(12): p. 1587-1595.
107. Xia, Y., Li, W., et al., *Gold nanocages: from synthesis to theranostic applications.* Acc Chem Res, 2011. **44**(10): p. 914-924.
108. Wang, A.X. and Kong, X., *Review of Recent Progress of Plasmonic Materials and Nano-Structures for Surface-Enhanced Raman Scattering.* Materials (Basel), 2015. **8**(6): p. 3024-3052.
109. McNay, G., Eustace, D., et al., *Surface-enhanced Raman scattering (SERS) and surface-enhanced resonance Raman scattering (SERRS): a review of applications.* Appl Spectrosc, 2011. **65**(8): p. 825-837.
110. Banholzer, M.J., Millstone, J.E., et al., *Rationally designed nanostructures for surface-enhanced Raman spectroscopy.* Chem Soc Rev, 2008. **37**(5): p. 885-897.
111. Xie, W. and Schlucker, S., *Rationally designed multifunctional plasmonic nanostructures for surface-enhanced Raman spectroscopy: a review.* Rep Prog Phys, 2014. **77**(11): p. 116502.
112. Kawawaki, T., Shinjo, N., and Tatsuma, T., *Backward-scattering-based Localized Surface Plasmon Resonance Sensors with Gold Nanospheres and Nanoshells.* Anal Sci, 2016. **32**(3): p. 271-274.
113. Kazuma, E. and Tatsuma, T., *Localized surface plasmon resonance sensors based on wavelength-tunable spectral dips.* Nanoscale, 2014. **6**(4): p. 2397-2405.
114. Mayer, K.M. and Hafner, J.H., *Localized surface plasmon resonance sensors.* Chem Rev, 2011. **111**(6): p. 3828-3857.
115. Aragay, G., Pons, J., and Merkoci, A., *Recent trends in macro-, micro-, and nanomaterial-based tools and strategies for heavy-metal detection.* Chem Rev, 2011. **111**(5): p. 3433-3458.
116. Tseng, C.H., Yang, T.C., et al., *Catalysis of oxidation of carbon monoxide on supported gold nanoparticle.* J Hazard Mater, 2009. **166**(2-3): p. 686-694.
117. Ojea-Jimenez, I., Lopez, X., et al., *Citrate-Coated Gold Nanoparticles As Smart Scavengers for Mercury(II) Removal from Polluted Waters.* Acs Nano, 2012. **6**(3): p. 2253-2260.
118. Yu, H., Wang, X., et al., *Photocatalytic degradation of malathion in aqueous solution using an Au-Pd-TiO2 nanotube film.* J Hazard Mater, 2010. **184**(1-3): p. 753-758.
119. Eustis, S. and el-Sayed, M.A., *Why gold nanoparticles are more precious than pretty gold: noble metal surface plasmon resonance and its enhancement of the radiative and nonradiative properties of nanocrystals of different shapes.* Chem Soc Rev, 2006. **35**(3): p. 209-217.
120. Narayanan, R. and El-Sayed, M.A., *Catalysis with transition metal nanoparticles in colloidal solution: nanoparticle shape dependence and stability.* J Phys Chem B, 2005. **109**(26): p. 12663-12676.
121. Wei, H., Wang, Z., et al., *Time-dependent, protein-directed growth of gold nanoparticles within a single crystal of lysozyme.* Nat Nanotechnol, 2011. **6**(2): p. 93-97.
122. Wei, H. and Lu, Y., *Catalysis of Gold Nanoparticles within Lysozyme Single Crystals.* Chem-Asian J, 2012. **7**(4): p. 680-683.
123. Liu, M.Y., Wang, L.B., et al., *Superior Catalytic Performance of Gold Nanoparticles Within Small Cross-Linked Lysozyme Crystals.* Langmuir, 2016. **32**(42): p. 10895-10904.
124. Ueno, T., Yokoi, N., et al., *Crystal structure based design of functional metal/protein hybrids.* J Inorg Biochem, 2007. **101**(11-12): p. 1667-1675.
125. Gardiner, D.J. and Graves, P.R., *Practical Raman Spectroscopy*. 1989, Springer Berlin Heidelberg,: Berlin, Heidelberg. p. 1 online resource (VIII, 157 pages 187 illustrations).
126. Edsall, T.J., *Cold Spring Harbor Symposium on Quantitative Biology.* 1938. **6**: p. 440-449.
127. Garfinkel, D. and Edsall, J.T., *Raman Spectra of Amino Acids and Related Compounds. X. The Raman Spectra of Certain Peptides and of Lysozyme1-3.* Journal of the American Chemical Society, 1958. **80**(15): p. 3818-3823.
128. Tobin, M.C., *Raman spectra of crystalline lysozyme, pepsin, and alpha chymotrypsin.* Science, 1968. **161**(3836): p. 68-69.
129. Lord, R.C. and Yu, N.T., *Laser-excited Raman spectroscopy of biomolecules. I. Native lysozyme and its constituent amino acids.* J Mol Biol, 1970. **50**(2): p. 509-524.
130. Lord, R.C. and Yu, N.T., *Laser-excited Raman spectroscopy of biomolecules. II. Native ribonuclease and alpha-chymotrypsin.* J Mol Biol, 1970. **51**(2): p. 203-213.

131. Rimai, L., Kilponen, R.G., and Gill, D., *Resonance-enhanced Raman spectra of visual pigments in intact bovine retinas at low temperatures.* Biochem Biophys Res Commun, 1970. **41**(2): p. 492-497.
132. Long, T.V., 2nd, Loer, T.M., et al., *Determination of iron coordination in nonheme iron proteins using laser-raman spectroscopy. II. Clostridium pasteurianum rubredoxin in aqueous solution.* J Am Chem Soc, 1971. **93**(7): p. 1809-1811.
133. Spiro, T.G. and Strekas, T.C., *Resonance Raman spectra of hemoglobin and cytochrome c: inverse polarization and vibronic scattering.* Proc Natl Acad Sci U S A, 1972. **69**(9): p. 2622-2626.
134. Strekas, T.C. and Spiro, T.G., *Cytochrome c: resonance Raman spectra.* Biochim Biophys Acta, 1972. **278**(1): p. 188-192.
135. Strekas, T.C. and Spiro, T.G., *Hemoglobin: resonance Raman spectra.* Biochim Biophys Acta, 1972. **263**(3): p. 830-833.
136. Efremov, E.V., Ariese, F., and Gooijer, C., *Achievements in resonance Raman spectroscopy review of a technique with a distinct analytical chemistry potential.* Anal Chim Acta, 2008. **606**(2): p. 119-134.
137. Carey, D.M. and Korenowski, G.M., *Measurement of the Raman spectrum of liquid water.* J Chem Phys, 1998. **108**(7): p. 2669-2675.
138. Rygula, A., Majzner, K., et al., *Raman spectroscopy of proteins: a review.* J Raman Spectrosc, 2013. **44**(8): p. 1061-1076.
139. Kong, J. and Yu, S., *Fourier transform infrared spectroscopic analysis of protein secondary structures.* Acta Bioch Bioph Sin, 2007. **39**(8): p. 549-559.
140. Harada, I., Miura, T., and Takeuchi, H., *Origin of the Doublet at 1360 and 1340 Cm-1 in the Raman-Spectra of Tryptophan and Related-Compounds.* Spectrochim Acta A, 1986. **42**(2-3): p. 307-312.
141. Chen, M.C., Lord, R.C., and Mendelsohn, R., *Laser-excited raman spectroscopy of biomolecules. IV. Thermal denaturation of aqueous lysozyme.* Biochim Biophys Acta, 1973. **328**(2): p. 252-260.
142. Hernandez, B., Coic, Y.M., et al., *All characteristic Raman markers of tyrosine and tyrosinate originate from phenol ring fundamental vibrations.* J Raman Spectrosc, 2016. **47**(2): p. 210-220.
143. Vergara, A., Merlino, A., et al., *A novel method for detection of selenomethionine incorporation in protein crystals via Raman microscopy.* Acta Crystallogr D Biol Crystallogr, 2008. **64**(Pt 2): p. 167-171.
144. Smulevich, G., Wang, Y., et al., *Single-Crystal Resonance Raman-Spectroscopy of Site-Directed Mutants of Cytochrome-C Peroxidase.* Biochemistry-Us, 1990. **29**(31): p. 7174-7180.
145. Vergara, A., Vitagliano, L., et al., *An Order-Disorder Transition Plays a Role in Switching Off the Root Effect in Fish Hemoglobins.* J Biol Chem, 2010. **285**(42): p. 32568-32575.
146. Di Fiore, A., Vergara, A., et al., *Hydroxylamine-O-sulfonamide is a versatile lead compound for the development of carbonic anhydrase inhibitors.* Chem Commun (Camb), 2015. **51**(57): p. 11519-11522.
147. Katona, G., Carpentier, P., et al., *Raman-assisted crystallography reveals end-on peroxide intermediates in a nonheme iron enzyme.* Science, 2007. **316**(5823): p. 449-453.
148. Kendrew, J.C., Bodo, G., et al., *A three-dimensional model of the myoglobin molecule obtained by x-ray analysis.* Nature, 1958. **181**(4610): p. 662-666.
149. Protein Data Bank. Available from: RCSB Protein Data Bank - RCSB PDB.
150. Glazer, A.M., *The first paper by W.L. Bragg – what and when?* Crystallography Reviews, 2013. **19**(3): p. 117-124.
151. Taylor, G., *The phase problem.* Acta Crystallogr D Biol Crystallogr, 2003. **59**(Pt 11): p. 1881-1890.
152. Hendrickson, W.A., *Determination of macromolecular structures from anomalous diffraction of synchrotron radiation.* Science, 1991. **254**(5028): p. 51-58.
153. Crick, F.H.C. and Magdoff, B.S., *The theory of the method of isomorphous replacement for protein crystals. I.* Acta Crystallographica, 1956. **9**(11): p. 901-908.
154. Garman, E.F. and Weik, M., *Radiation damage to biological macromolecules: some answers and more questions.* J Synchrotron Radiat, 2013. **20**(Pt 1): p. 1-6.
155. Gerstel, M., Deane, C.M., and Garman, E.F., *Identifying and quantifying radiation damage at the atomic level.* J Synchrotron Radiat, 2015. **22**(2): p. 201-212.

156. Sutton, K.A., Black, P.J., et al., *Insights into the mechanism of X-ray-induced disulfide-bond cleavage in lysozyme crystals based on EPR, optical absorption and X-ray diffraction studies.* Acta Crystallographica Section D: Biological Crystallography, 2013. **69**(Pt 12): p. 2381-2394.
157. Burmeister, W.P., *Structural changes in a cryo-cooled protein crystal owing to radiation damage.* Acta Crystallogr D, 2000. **56**: p. 328-341.
158. Ravelli, R.B.G., McSweeney, S., et al., *Toward minimizing the 'fingerprint' x-rays leave on macromolecular structures.* Biophys J, 2000. **78**(1): p. 484a-484a.
159. Ravelli, R.B.G. and McSweeney, S.M., *The 'fingerprint' that X-rays can leave on structures.* Struct Fold Des, 2000. **8**(3): p. 315-328.
160. Weik, M., Ravelli, R.B.G., et al., *Specific chemical and structural damage to proteins produced by synchrotron radiation.* P Natl Acad Sci USA, 2000. **97**(2): p. 623-628.
161. Weik, M., Berges, J., et al., *Evidence for the formation of disulfide radicals in protein crystals upon X-ray irradiation.* Journal of Synchrotron Radiation, 2002. **9**: p. 342-346.
162. Fioravanti, E., Vellieux, F.M.D., et al., *Specific radiation damage to acidic residues and its relation to their chemical and structural environment.* Journal of Synchrotron Radiation, 2007. **14**: p. 84-91.
163. Ennifar, E., Carpentier, P., et al., *X-ray-induced debromination of nucleic acids at the BrK absorption edge and implications for MAD phasing.* Acta Crystallogr D, 2002. **58**: p. 1262-1268.
164. Ramagopal, U.A., Dauter, Z., et al., *Radiation-induced site-specific damage of mercury derivatives: phasing and implications.* Acta Crystallogr D, 2005. **61**: p. 1289-1298.
165. Garman, E.F. and Weik, M., *Radiation damage to macromolecules: kill or cure?* J Synchrotron Radiat, 2015. **22**(2): p. 195-200.
166. Garman, E.F. and Weik, M., *Macromolecular crystallography radiation damage research: what's new?* J Synchrotron Radiat, 2011. **18**(Pt 3): p. 313-317.
167. McGeehan, J.E., Bourgeois, D., et al., *Raman-assisted crystallography of biomolecules at the synchrotron: instrumentation, methods and applications.* Biochim Biophys Acta, 2011. **1814**(6): p. 750-759.
168. Carey, P.R. and Dong, J., *Following ligand binding and ligand reactions in proteins via Raman crystallography.* Biochemistry-Us, 2004. **43**(28): p. 8885-8893.
169. Merlino, A., Fuchs, M.R., et al., *Selective X-ray-induced NO photodissociation in haemoglobin crystals: evidence from a Raman-assisted crystallographic study.* Acta Crystallogr D Biol Crystallogr, 2013. **69**(Pt 1): p. 137-140.
170. Park, J.D. and Zheng, W., *Human exposure and health effects of inorganic and elemental mercury.* J Prev Med Public Health, 2012. **45**(6): p. 344-352.
171. Karagas, M.R., Choi, A.L., et al., *Evidence on the human health effects of low-level methylmercury exposure.* Environ Health Perspect, 2012. **120**(6): p. 799-806.
172. Aschner, M., Onishchenko, N., and Ceccatelli, S., *Toxicology of alkylmercury compounds.* Met Ions Life Sci, 2010. **7**: p. 403-434.
173. Garcia, J.J., Martinez-Ballarin, E., et al., *Effects of trace elements on membrane fluidity.* J Trace Elem Med Biol, 2005. **19**(1): p. 19-22.
174. Houston, M.C., *Role of mercury toxicity in hypertension, cardiovascular disease, and stroke.* J Clin Hypertens (Greenwich), 2011. **13**(8): p. 621-627.
175. Koedrith, P. and Seo, Y.R., *Advances in carcinogenic metal toxicity and potential molecular markers.* Int J Mol Sci, 2011. **12**(12): p. 9576-9595.
176. Valko, M., Morris, H., and Cronin, M.T., *Metals, toxicity and oxidative stress.* Curr Med Chem, 2005. **12**(10): p. 1161-1208.
177. Bernhoft, R.A., *Mercury toxicity and treatment: a review of the literature.* J Environ Public Health, 2012. **2012**: p. 460508.
178. Guzzi, G. and La Porta, C.A., *Molecular mechanisms triggered by mercury.* Toxicology, 2008. **244**(1): p. 1-12.
179. Vas, J. and Monestier, M., *Immunology of mercury.* Ann N Y Acad Sci, 2008. **1143**: p. 240-267.
180. Carvalho, C.M., Chew, E.H., et al., *Inhibition of the human thioredoxin system. A molecular mechanism of mercury toxicity.* J Biol Chem, 2008. **283**(18): p. 11913-11923.
181. Zamora, F., Kunsman, M., et al., *Metal-Stabilized Rare Tautomers of Nucleobases. 6. Imino Tautomer of Adenine in a Mixed-Nucleobase Complex of Mercury(II).* Inorg Chem, 1997. **36**(8): p. 1583-1587.

182. Zheng, R., Zheng, X.J., et al., *Proteins can convert to beta-sheet in single crystals.* Protein Sci, 2004. **13**(5): p. 1288-1294.
183. Smith, G.D., Pangborn, W.A., and Blessing, R.H., *The structure of T-6 bovine insulin.* Acta Crystallogr D, 2005. **61**: p. 1476-1482.
184. Dong, J., Swift, K., et al., *Probing inhibitors binding to human urokinase crystals by Raman microscopy: implications for compound screening.* Biochemistry-Us, 2001. **40**(33): p. 9751-9757.
185. Zako, T., Sakono, M., et al., *Bovine Insulin Filaments Induced by Reducing Disulfide Bonds Show a Different Morphology, Secondary Structure, and Cell Toxicity from Intact Insulin Amyloid Fibrils.* Biophys J, 2009. **96**(8): p. 3331-3340.
186. Jalilehvand, F., Leung, B.O., et al., *Mercury(II) cysteine complexes in alkaline aqueous solution.* Inorg Chem, 2006. **45**(1): p. 66-73.
187. Hoffmann, G.G., Brockner, W., and Steinfatt, I., *Bis(n-alkanethiolato)mercury(II) compounds, Hg(SCnH2n+1)(2) (n=1 to 10, 12): Preparation methods, vibrational spectra, GC/MS investigations, and exchange reactions with diorganyl disulfides.* Inorganic Chemistry, 2001. **40**(5): p. 977-985.
188. Parker, W.R. and Brodbelt, J.S., *Characterization of the Cysteine Content in Proteins Utilizing Cysteine Selenylation with 266 nm Ultraviolet Photodissociation (UVPD).* J Am Soc Mass Spectrom, 2016. **27**(8): p. 1344-1350.
189. Garman, E.F., *Radiation damage in macromolecular crystallography: what is it and why should we care?* Acta Crystallogr D, 2010. **66**: p. 339-351.
190. Garman, E.F., *Radiation damage in macromolecular crystallography: what is it and why should we care?* Acta Crystallogr D Biol Crystallogr, 2010. **66**(Pt 4): p. 339-351.
191. Murray, J.W., Garman, E.F., and Ravelli, R.B.G.J., *X-ray absorption by macromolecular crystals: the effects of wavelength and crystal composition on absorbed dose.* J. Appl. Cryst., 2004. **37**: p. 513-522.
192. Sutton, K.A., Black, P.J., et al., *Insights into the mechanism of X-ray-induced disulfide-bond cleavage in lysozyme crystals based on EPR, optical absorption and X-ray diffraction studies.* Acta Crystallogr D, 2013. **69**: p. 2381-2394.
193. Burmeister, W.P., *Structural changes in a cryo-cooled protein crystal owing to radiation damage.* Acta Crystallogr D Biol Crystallogr, 2000. **56**(Pt 3): p. 328-341.
194. Yano, J., Kern, J., et al., *X-ray damage to the Mn4Ca complex in single crystals of photosystem II: a case study for metalloprotein crystallography.* Proc Natl Acad Sci U S A, 2005. **102**(34): p. 12047-12052.
195. Merlino, A., Fuchs, M.R., et al., *Selective X-ray-induced NO photodissociation in haemoglobin crystals: evidence from a Raman-assisted crystallographic study.* Acta Crystallogr D, 2013. **69**: p. 137-140.
196. Vergara, A., Merlino, A., et al., *A novel method for detection of selenomethionine incorporation in protein crystals via Raman microscopy.* Acta Crystallogr D, 2008. **64**: p. 167-171.
197. Di Fiore, A., Vergara, A., et al., *Hydroxylamine-O-sulfonamide is a versatile lead compound for the development of carbonic anhydrase inhibitors.* Chem Commun, 2015. **51**(57): p. 11519-11522.
198. Di Fiore, A., De Simone, G., et al., *A new lead compound for the development of Carbonic Anhydrase inhibitors.* Protein Sci, 2015. **24**: p. 50-50.
199. Carpentier, P., Royant, A., et al., *Raman-Assisted Crystallography Suggests a Mechanism of X-Ray-Induced Disulfide Radical Formation and Reparation.* Structure, 2010. **18**(11): p. 1410-1419.
200. Thomas, G.J., Jr., *Raman spectroscopy of protein and nucleic acid assemblies.* Annu Rev Biophys Biomol Struct, 1999. **28**: p. 1-27.
201. McGeehan, J.E., Carpentier, P., et al., *X-ray radiation-induced damage in DNA monitored by online Raman.* J Synchrotron Radiat, 2007. **14**(Pt 1): p. 99-108.
202. Adam, V., Carpentier, P., et al., *Structural Basis of X-ray-Induced Transient Photobleaching in a Photoactivatable Green Fluorescent Protein.* J Am Chem Soc, 2009. **131**(50): p. 18063-+.
203. Raines, R.T., *Ribonuclease A.* Chem Rev, 1998. **98**(3): p. 1045-1066.
204. Neira, J.L. and Rico, M., *Folding studies on ribonuclease A, a model protein.* Fold Des, 1997. **2**(1): p. R1-R11.
205. Gutte, B. and Merrifield, R.B., *The synthesis of ribonuclease A.* J Biol Chem, 1971. **246**(6): p. 1922-1941.

206. Moore, S. and Stein, W.H., *Chemical structures of pancreatic ribonuclease and deoxyribonuclease.* Science, 1973. **180**(4085): p. 458-464.
207. Picone, D., Donnarumma, F., et al., *Platinated oligomers of bovine pancreatic ribonuclease: Structure and stability.* J Inorg Biochem, 2015. **146**: p. 37-43.
208. Vergara, A., Russo Krauss, I., et al., *Investigating the Ruthenium Metalation of Proteins: X-ray Structure and Raman Microspectroscopy of the Complex between RNase A and AziRu.* Inorg Chem, 2013. **52**(19): p. 10714-10716.
209. Messori, L. and Merlino, A., *Cisplatin binding to proteins: molecular structure of the ribonuclease a adduct.* Inorg Chem, 2014. **53**(8): p. 3929-3931.
210. Messori, L., Scaletti, F., et al., *Interactions of gold-based drugs with proteins: crystal structure of the adduct formed between ribonuclease A and a cytotoxic gold(III) compound.* Metallomics, 2014. **6**(2): p. 233-236.
211. Nanao, M.H., Sheldrick, G.M., and Ravelli, R.B.G., *Improving radiation-damage substructures for RIP.* Acta Crystallogr D, 2005. **61**: p. 1227-1237.
212. Bourgeois, D., Katona, G., et al., *Raman-assisted X-ray crystallography for the analysis of biomolecules.* Methods Mol Biol, 2009. **544**: p. 253-267.
213. Sica, F., Adinolfi, S., et al., *Crystallization of multiple forms of bovine seminal ribonuclease in the liganded and unliganded state.* J Cryst Growth, 1999. **196**(2-4): p. 305-312.
214. Berisio, R., Lamzin, V.S., et al., *Protein titration in the crystal state.* J Mol Biol, 1999. **292**(4): p. 845-854.
215. Vitagliano, L., Merlino, A., et al., *Productive and nonproductive binding to ribonuclease A: X-ray structure of two complexes with uridylyl(2 ',5 ')guanosine.* Protein Sci, 2000. **9**(6): p. 1217-1225.
216. Paithankar, K.S., Owen, R.L., and Garman, E.F., *Absorbed dose calculations for macromolecular crystals: improvements to RADDOSE.* J Synchrotron Radiat, 2009. **16**(Pt 2): p. 152-162.
217. Otwinowsky, Z. and Minor, W., *Processing of X-ray diffraction data collected in oscillation mode.* Methods Enzymol., 1997: p. 307-326.
218. Sheldrick, G.M. and Schneider, T.R., *SHELXL: high-resolution refinement.* Methods Enzymol, 1997. **277**: p. 319-343.
219. Gerstel, M., Deane, C.M., and Garman, E.F., *Identifying and quantifying radiation damage at the atomic level.* J Synchrotron Radiat, 2015. **22**: p. 201-212.
220. Garman, E.F. and Weik, M., *Radiation damage to macromolecules: kill or cure?* J Synchrotron Radiat, 2015. **22**: p. 195-200.
221. Owen, R.L., Pearson, A.R., et al., *A new on-axis multimode spectrometer for the macromolecular crystallography beamlines of the Swiss Light Source.* J Synchrotron Radiat, 2009. **16**: p. 173-182.
222. Kudryavtsev, A.B., Mirov, S.B., et al., *Polarized Raman spectroscopic studies of tetragonal lysozyme single crystals.* Acta Crystallogr D, 1998. **54**: p. 1216-1229.
223. Hernandez, B., Pfluger, F., et al., *Characteristic Raman lines of phenylalanine analyzed by a multiconformational approach.* J Raman Spectrosc, 2013. **44**(6): p. 827-833.
224. Zhu, G.Y., Zhu, X., et al., *Raman spectra of amino acids and their aqueous solutions.* Spectrochim Acta A, 2011. **78**(3): p. 1187-1195.
225. Garman, E.F. and Owen, R.L., *Cryocooling and radiation damage in macromolecular crystallography.* Acta Crystallogr D, 2006. **62**: p. 32-47.
226. Culka, A., Jehlicka, J., and Edwards, H.G.M., *Acquisition of Raman spectra of amino acids using portable instruments: Outdoor measurements and comparison.* Spectrochim Acta A, 2010. 77(5): p. 978-983.
227. Pacansky, J., Koch, W., and Miller, M.D., *Analysis of the Structures, Infrared-Spectra, and Raman-Spectra for the Methyl, Ethyl, Isopropyl, and Tert-Butyl Radicals.* J Am Chem Soc, 1991. **113**(1): p. 317-328.
228. Uchida, M., Klem, M.T., et al., *Biological containers: Protein cages as multifunctional nanoplatforms.* Adv Mater, 2007. **19**(8): p. 1025-1042.
229. Dickerson, M.B., Sandhage, K.H., and Naik, R.R., *Protein- and Peptide-Directed Syntheses of Inorganic Materials.* Chemical Reviews, 2008. **108**(11): p. 4935-4978.
230. Guli, M., Lambert, E.M., et al., *Template-Directed Synthesis of Nanoplasmonic Arrays by Intracrystalline Metalization of Cross-Linked Lysozyme Crystals.* Angew Chem Int Edit, 2010. **49**(3): p. 520-523.

231. Baksi, A. and Pradeep, T., *Noble metal alloy clusters in the gas phase derived from protein templates: unusual recognition of palladium by gold.* Nanoscale, 2013. **5**(24): p. 12245-12254.
232. Alterio, V., Di Fiore, A., et al., *Multiple binding modes of inhibitors to carbonic anhydrases: how to design specific drugs targeting 15 different isoforms?* Chem Rev, 2012. **112**(8): p. 4421-4468.
233. Supuran, C.T., *Carbonic anhydrases: novel therapeutic applications for inhibitors and activators.* Nat Rev Drug Discov, 2008. **7**(2): p. 168-181.
234. De Simone, G., Di Fiore, A., et al., *The zinc coordination pattern in the eta-carbonic anhydrase from Plasmodium falciparum is different from all other carbonic anhydrase genetic families.* Bioorg Med Chem Lett, 2015. **25**(7): p. 1385-1389.
235. Supuran, C.T., Di Fiore, A., and De Simone, G., *Carbonic anhydrase inhibitors as emerging drugs for the treatment of obesity.* Expert Opin Emerg Dr, 2008. **13**(2): p. 383-392.
236. Supuran, C.T., Di Fiore, A., et al., *Recent Advances in Structural Studies of the Carbonic Anhydrase Family: The Crystal Structure of Human CA IX and CA XIII.* Curr Pharm Design, 2010. **16**(29): p. 3246-3254.
237. Del Giudice, R., Monti, D.M., et al., *Human carbonic anhydrase VII protects cells from oxidative damage.* Biol Chem, 2013. **394**(10): p. 1343-1348.
238. Supuran, C.T. and De Simone, G., *Carbonic Anhydrases as Biocatalysts*. 1st ed. Vol. 1. 2015: Elsevier.
239. Winum, J.Y. and Supuran, C.T., *Recent advances in the discovery of zinc-binding motifs for the development of carbonic anhydrase inhibitors.* J Enzym Inhib Med Ch, 2015. **30**(2): p. 321-324.
240. D'Ambrosio, K., Carradori, S., et al., *Out of the active site binding pocket for carbonic anhydrase inhibitors.* Chem Commun, 2015. **51**(2): p. 302-305.
241. Belock, C.W., Cetin, A., et al., *Transition metal coordination chemistry of N,N-Bis(2-{pyrid-2-ylethyl})hydroxylamine.* Inorganic Chemistry, 2008. **47**(16): p. 7114-7120.
242. Di Fiore, A., Maresca, A., et al., *Hydroxamate represents a versatile zinc binding group for the development of new carbonic anhydrase inhibitors.* Chem Commun, 2012. **48**(70): p. 8838-8840.
243. Sippel, K.H., Robbins, A.H., et al., *High-resolution structure of human carbonic anhydrase II complexed with acetazolamide reveals insights into inhibitor drug design.* Acta Crystallogr F, 2009. **65**: p. 992-995.
244. De La Cruz, C. and Sheppard, N., *A structure-based analysis of the vibrational spectra of nitrosyl ligands in transition-metal coordination complexes and clusters.* Spectrochim Acta A, 2011. **78**(1): p. 7-28.
245. Chen, H., Cho, K.B., et al., *Dioxygen Activation by a Non-Heme Iron(II) Complex: Theoretical Study toward Understanding Ferric-Superoxo Complexes.* J Chem Theory Comput, 2012. **8**(3): p. 915-926.
246. Cho, J., Sarangi, R., and Nam, W., *Mononuclear metal-O2 complexes bearing macrocyclic N-tetramethylated cyclam ligands.* Acc Chem Res, 2012. **45**(8): p. 1321-1330.
247. Liu, J.G., Ohta, T., et al., *Spectroscopic Characterization of a Hydroperoxo-Heme Intermediate: Conversion of a Side-On Peroxo to an End-On Hydroperoxo Complex.* Angew Chem Int Edit, 2009. **48**(49): p. 9262-9267.
248. ChemAxon. Marvin. Available from: http://www.chemaxon.com/marvin/sketch/index.php.
249. Temperini, C., Winum, J.Y., et al., *Carbonic anhydrase inhibitors: The X-ray crystal structure of the adduct of N-hydroxysulfamide with isozyme II explains why this new zinc binding function is effective in the design of potent inhibitors.* Bioorganic & Medicinal Chemistry Letters, 2007. **17**(10): p. 2795-2801.
250. Scott, A.D., Phillips, C., et al., *Thermodynamic Optimisation in Drug Discovery: A Case Study using Carbonic Anhydrase Inhibitors.* Chemmedchem, 2009. **4**(12): p. 1985-1989.
251. Maresca, A., Temperini, C., et al., *Non-Zinc Mediated Inhibition of Carbonic Anhydrases: Coumarins Are a New Class of Suicide Inhibitors.* Journal of the American Chemical Society, 2009. **131**(8): p. 3057-3062.
252. Carta, F., Temperini, C., et al., *Polyamines Inhibit Carbonic Anhydrases by Anchoring to the Zinc-Coordinated Water Molecule.* Journal of Medicinal Chemistry, 2010. **53**(15): p. 5511-5522.
253. Carta, F., Aggarwal, M., et al., *Dithiocarbamates: a new class of carbonic anhydrase inhibitors. Crystallographic and kinetic investigations.* Chem Commun, 2012. **48**(13): p. 1868-1870.

254. Carta, F., Akdemir, A., et al., *Xanthates and Trithiocarbonates Strongly Inhibit Carbonic Anhydrases and Show Antiglaucoma Effects in Vivo.* Journal of Medicinal Chemistry, 2013. **56**(11): p. 4691-4700.
255. Tars, K., Vullo, D., et al., *Sulfocoumarins (1,2-benzoxathiine-2,2-dioxides): a class of potent and isoform-selective inhibitors of tumor-associated carbonic anhydrases.* J Med Chem, 2013. **56**(1): p. 293-300.
256. Martin, D.P. and Cohen, S.M., *Nucleophile recognition as an alternative inhibition mode for benzoic acid based carbonic anhydrase inhibitors.* Chem Commun, 2012. **48**(43): p. 5259-5261.
257. Maresca, A., Temperini, C., et al., *Correction to Deciphering the Mechanism of Carbonic Anhydrase Inhibition with Coumarins and Thiocoumarins.* J Med Chem, 2015. **58**(14): p. 5689.
258. Maresca, A., Temperini, C., et al., *Deciphering the mechanism of carbonic anhydrase inhibition with coumarins and thiocoumarins.* J Med Chem, 2010. **53**(1): p. 335-344.
259. Casini, A., Guerri, A., et al., *Biophysical characterisation of adducts formed between anticancer metallodrugs and selected proteins: New insights from X-ray diffraction and mass spectrometry studies.* J Inorg Biochem, 2008. **102**(5-6): p. 995-1006.
260. Casini, A. and Reedijk, J., *Interactions of anticancer Pt compounds with proteins: an overlooked topic in medicinal inorganic chemistry?* Chem Sci, 2012. **3**(11): p. 3135-3144.
261. Cubo, L., Groessl, M., et al., *Proteins as Possible Targets for Cytotoxic trans-Platinum(II) Complexes with Aliphatic Amine Ligands: Further Exceptions to the DNA Paradigm.* Chemmedchem, 2010. **5**(8): p. 1335-1343.
262. Lv, X.J., Zhao, M., et al., *Loading cisplatin onto 6-mercaptopurine covalently modified MSNS: a nanomedicine strategy to improve the outcome of cisplatin therapy.* Drug Des Dev Ther, 2016. **10**: p. 3933-3946.
263. Hartinger, C.G. and Dyson, P.J., *Bioorganometallic chemistry-from teaching paradigms to medicinal applications.* Chemical Society Reviews, 2009. **38**(2): p. 391-401.
264. Romao, C.C., Blattler, W.A., et al., *Developing drug molecules for therapy with carbon monoxide.* Chemical Society Reviews, 2012. **41**(9): p. 3571-3583.
265. Mann, B.E., Johnson, T.R., et al., *Metal carbonyls - A new class of pharmaceuticals?* J Inorg Biochem, 2003. **96**(1): p. 40-40.
266. Pizarro, M.D., Rodriguez, J.V., et al., *Protective effects of a carbon monoxide-releasing molecule (CORM-3) during hepatic cold preservation.* Cryobiology, 2009. **58**(3): p. 248-255.
267. Motterlini, R., Clark, J.E., et al., *Carbon monoxide-releasing molecules - Characterization of biochemical and vascular activities.* Circulation Research, 2002. **90**(2): p. E17-E24.
268. Long, L., Jiang, X.J., et al., *Water-soluble diiron hexacarbonyl complex as a CO-RM: controllable CO-releasing, releasing mechanism and biocompatibility.* Dalton T, 2013. **42**(44): p. 15663-15669.
269. Bani-Hani, M.G., Greenstein, D., et al., *A carbon monoxide-releasing molecule (CORM-3) attenuates lipopolysaccharide- and interferon-gamma-induced inflammation in microglia.* Pharmacol Rep, 2006. **58 Suppl**: p. 132-144.
270. Motterlini, R., Haas, B., and Foresti, R., *Emerging concepts on the anti-inflammatory actions of carbon monoxide-releasing molecules (CO-RMs).* Med Gas Res, 2012. **2**(1): p. 28.
271. Wilson, J.L., Wareham, L.K., et al., *CO-Releasing Molecules Have Nonheme Targets in Bacteria: Transcriptomic, Mathematical Modeling and Biochemical Analyses of CORM-3 [Ru(CO)(3)Cl(glycinate)] Actions on a Heme-Deficient Mutant of Escherichia coli.* Antioxid Redox Sign, 2015. **23**(2): p. 148-162.
272. Schwer, C.I., Mutschler, M., et al., *Carbon Monoxide Releasing Molecule-2 Inhibits Pancreatic Stellate Cell Proliferation by Activating p38 Mitogen-Activated Protein Kinase/Heme Oxygenase-1 Signaling.* Mol Pharmacol, 2010. **77**(4): p. 660-669.
273. Herrick, R.S., Ziegler, C.J., and Leeper, T.C., *Structure and function in organometallic.protein complexes.* J Organomet Chem, 2014. **751**: p. 90-110.
274. Santos-Silva, T., Mukhopadhyay, A., et al., *Towards Improved Therapeutic CORMs: Understanding the Reactivity of CORM-3 with Proteins.* Current Medicinal Chemistry, 2011. **18**(22): p. 3361-3366.
275. Russo Krauss, I., Sica, F., et al., *Increasing the X-ray Diffraction Power of Protein Crystals by Dehydration: The Case of Bovine Serum Albumin and a Survey of Literature Data.* International Journal of Molecular Sciences, 2012. **13**(3): p. 3782-3800.
276. Russo Krauss, I., Messori, L., et al., *Interactions of gold-based drugs with proteins: the structure and stability of the adduct formed in the reaction between lysozyme and the cytotoxic gold(III) compound Auoxo3.* Dalton T, 2014. **43**(46): p. 17483-17488.

277. Messori, L., Cinellu, M.A., and Merlino, A., *Protein Recognition of Gold-Based Drugs: 3D Structure of the Complex Formed When Lysozyme Reacts with Aubipy(c).* Acs Med Chem Lett, 2014. **5**(10): p. 1110-1113.
278. Vitagliano, L., Merlino, A., et al., *Reversible substrate-induced domain motions in ribonuclease A.* Proteins, 2002. **46**(1): p. 97-104.
279. Murshudov, G.N., Skubak, P., et al., *REFMAC5 for the refinement of macromolecular crystal structures.* Acta Crystallogr D Biol Crystallogr, 2011. **67**(Pt 4): p. 355-367.
280. Emsley, P., Lohkamp, B., et al., *Features and development of Coot.* Acta Crystallogr D Biol Crystallogr, 2010. **66**(Pt 4): p. 486-501.
281. Pettersen, E.F., Goddard, T.D., et al., *UCSF Chimera--a visualization system for exploratory research and analysis.* J Comput Chem, 2004. **25**(13): p. 1605-1612.
282. Picone, D., Donnarumma, F., et al., *Platinated oligomers of bovine pancreatic ribonuclease: Structure and stability.* J Inorg Biochem, 2015. **146**: p. 37-43.
283. Ang, W.H., Parker, L.J., et al., *Rational design of an organometallic glutathione transferase inhibitor.* Angew Chem Int Ed Engl, 2009. **48**(21): p. 3854-3857.
284. Messori, L., Marzo, T., and Merlino, A., *Interactions of carboplatin and oxaliplatin with proteins: Insights from X-ray structures and mass spectrometry studies of their ribonuclease A adducts.* J Inorg Biochem, 2015. **153**: p. 136-142.
285. Ferraro, G., Messori, L., and Merlino, A., *The X-ray structure of the primary adducts formed in the reaction between cisplatin and cytochrome c.* Chem Commun (Camb), 2015. **51**(13): p. 2559-2561.
286. Huliciak, M., Reinhard, L., et al., *Crystals of Na(+)/K(+)-ATPase with bound cisplatin.* Biochem Pharmacol, 2014. **92**(3): p. 494-498.
287. Ferraro, G., Massai, L., et al., *Cisplatin binding to human serum albumin: a structural study.* Chem Commun (Camb), 2015. **51**(46): p. 9436-9439.
288. Tabe, H., Shimoi, T., et al., *Photoactivatable CO release from engineered protein crystals to modulate NF-kappaB activation.* Chem Commun (Camb), 2016. **52**(24): p. 4545-4548.
289. Albuquerque, I.S., Jeremias, H.F., et al., *An artificial CO-releasing metalloprotein built by histidine-selective metallation.* Chem Commun (Camb), 2015. **51**(19): p. 3993-3996.
290. Crabtree, R., *Iridium compounds in catalysis.* Accounts of Chemical Research, 1979. **12**(9): p. 331-337.
291. Yu, Z.-T., *Photochemical Solar Energy Conversion and Storage Using Cyclometalated Iridium Complexes*, in *Organometallics and Related Molecules for Energy Conversion*, W.-Y. Wong, Editor. 2015, Springer Berlin Heidelberg: Berlin, Heidelberg. p. 513-537.
292. Housecroft, C.E., *Iridium: Inorganic & Coordination Chemistry*, in *Encyclopedia of Inorganic Chemistry*. 2006, John Wiley & Sons, Ltd.
293. Zhang, S., Hosaka, M., et al., *Phosphorescent Light–Emitting Iridium Complexes Serve as a Hypoxia-Sensing Probe for Tumor Imaging in Living Animals.* Cancer Research, 2010. **70**(11): p. 4490-4498.
294. Davis, K.M., Bitting, A.L., et al., *Iridium(III) Luminescent Probe for Detection of the Malarial Protein Biomarker Histidine Rich Protein-II.* J Vis Exp, 2015(101): p. e52856.
295. Simeone, L., Mangiapia, G., et al., *Cholesterol-based nucleolipid-ruthenium complex stabilized by lipid aggregates for antineoplastic therapy.* Bioconjug Chem, 2012. **23**(4): p. 758-770.
296. Mangiapia, G., D'Errico, G., et al., *Ruthenium-based complex nanocarriers for cancer therapy.* Biomaterials, 2012. **33**(14): p. 3770-3782.
297. Vergara, A., D'Errico, G., et al., *Interaction of Anticancer Ruthenium Compounds with Proteins: High-Resolution X-ray Structures and Raman Microscopy Studies of the Adduct between Hen Egg White Lysozyme and AziRu.* Inorganic Chemistry, 2013. **52**(8): p. 4157-4159.
298. Cetinbas, N., Webb, M.I., et al., *Serum-protein interactions with anticancer Ru(III) complexes KP1019 and KP418 characterized by EPR.* J Biol Inorg Chem, 2010. **15**(2): p. 131-145.
299. Otwinowski, Z. and Minor, W., *Processing of X-ray diffraction data collected in oscillation mode.* Methods Enzymol, 1997. **276**: p. 307-326.
300. McCoy, A.J., Grosse-Kunstleve, R.W., et al., *Phaser crystallographic software.* J Appl Crystallogr, 2007. **40**(Pt 4): p. 658-674.
301. Crosas, E., Castellvi, A., et al., *Uridine as a new scavenger for synchrotron-based structural biology techniques.* Journal of Synchrotron Radiation, 2017. **24**: p. 53-62.
302. Wardman, P., *Electron transfer and oxidative stress as key factors in the design of drugs selectively active in hypoxia.* Curr Med Chem, 2001. **8**(7): p. 739-761.

303. Webb, M.I. and Walsby, C.J., *Control of ligand-exchange processes and the oxidation state of the antimetastatic Ru(III) complex NAMI-A by interactions with human serum albumin.* Dalton Trans, 2011. **40**(6): p. 1322-1331.
304. Klots, T.D., *Raman vapor spectrum and vibrational assignment for pyridine1.* Spectrochimica Acta Part A: Molecular and Biomolecular Spectroscopy, 1998. **54**(10): p. 1481-1498.
305. Muniz-Miranda, M., Cardini, G., and Schettino, V., *Surface-enhanced Raman spectra of pyridine and pyrazolide on silver colloids: chemical and electromagnetic effects.* Theoretical Chemistry Accounts, 2004. **111**(2): p. 264-269.
306. Wu, D.-Y., Li, J.-F., et al., *Electrochemical surface-enhanced Raman spectroscopy of nanostructures.* Chemical Society Reviews, 2008. **37**(5): p. 1025-1041.
307. Lever, A.B.P., *Electrochemical Parametrization of Rhenium Redox Couples.* Inorganic Chemistry, 1991. **30**(9): p. 1980-1985.